THÈSE

En vue de l'obtention du

DOCTORAT DE L'UNIVERSITÉ DE TOULOUSE

Délivré par :

Institut National Polytechnique de Toulouse (Toulouse INP)

Discipline ou spécialité :

Energétique et Transferts

Présentée et soutenue par :

Mme ESLI TREJO PEIMBERT

le jeudi 22 novembre 2018

Titre :

Dynamics and Transfers in two phase flows with phase change in normal and microgravity conditions

---

Ecole doctorale :

Mécanique, Energétique, Génie civil, Procédés (MEGeP)

Unité de recherche :

Institut de Mécanique des Fluides de Toulouse (I.M.F.T.)

Directeur(s) de Thèse :

MME CATHERINE COLIN

Rapporteurs :

M. DAVID BRUTIN, AIX-MARSEILLE UNIVERSITE

Mme NADIA CANEY, UNIVERSITE GRENOBLE ALPES

Membre(s) du jury :

Mme VERONIQUE ROIG, INP TOULOUSE, Président

M. JULIEN SEBILLEAU, INP TOULOUSE, Membre

Mme CATHERINE COLIN, INP TOULOUSE, Membre

M. ROBERTO ZENIT, UNIVERSITE NATIONALE AUTONOME DE MEXICO, Membre

Dynamics and Transfers of two-phase flows with phase change for normal and microgravity conditions

TREJO PEIMBERT Esli

Abstract

Two-phase flows with or without phase change are present in industrial and space applications. Gas-liquid and liquid-vapor pipe flows in microgravity have been studied for more than forty years. The studies were motivated by potential applications for space industries like thermal control of satellites, propellant supply for launchers, and waste water treatment for space exploration mission. Experiments with HFE700 were conducted in a vertical heated tube in normal and microgravity conditions to gather data on flow patterns, pressure drops, heat transfers and void fraction in thermohydraulic systems. Two different methods used to deduce heat transfer coefficients, were applied and compared. In addition, special focus was made for a specific regime of flow boiling. Annular flow structures were studied and digital image analysis was executed to detect disturbance waves, wave velocities and wave frequencies. Results and comparisons are related to the pressure drops and interfacial shear stress that changed with gravity that help model flow boiling.

Keywords: flow boiling, microgravity, heat transfer, void fraction

Les écoulements diphasiques avec ou sans changement de phase sont présents dans les applications spatiales et industrielles. Les écoulements gaz-liquide et liquide-vapeur en microgravité sont étudiés depuis plus de quarante ans. Les études ont été motivés par des applications potentielles pour l'industrie spatiale comme le contrôle thermique des satellites, l'approvisionnement en gaz propulseur pour les lanceurs et le traitement des eaux usées pour la mission d'exploration spatiale. Des expériences avec HFE700 ont été menées dans un tube vertical chauffé dans des conditions normales et de microgravité afin de recueillir des données sur les régimes d'écoulement, les pertes de pression, les transferts thermiques et le taux de vide dans les systèmes thermohydrauliques. Deux méthodes différentes utilisées pour déduire les coefficients de transfert de chaleur ont été appliquées et comparées. En outre, une attention particulière a été accordée à un régime spécifique d'écoulement en ébullition convective. Les structures d'écoulement annulaire ont été étudiées et une analyse d'image a été effectuée pour détecter les vagues, les vitesses des ondes et les fréquences des ondes. Les résultats et les comparaisons sont liés aux pertes de pression et à la contrainte de cisaillement interfaciale qui change avec la gravité et qui aident à modéliser le d'ébullition convective.

Mots clés: ébullition convective, microgravité, transferts thermiques, taux de vide

Contents

List of Figures

List of Tables

Nomenclature

Symbol	Name	Unit
A	cross-section area	m^2
Bo	Boiling number	[-]
C	constant	
Cp	specific heat at constant pressure	$J/K/kg$
D	diameter	m
e	rate of entrainment	[-]
f	friction factor	[-]
Fr	Froude number	[-]
g	acceleration	m/s^2
G	mass flux	$kg/m^2/s$
$h_{l,v}$	latent heat of vaporization	J/kg
h	heat transfer coefficient	$W/m^2/K$
j	superficial velocity	m/s
Ja	Jakob number	[-]
k	sapphire thermal conductivity	$W/m/K$
K_{pr} or K_{Kum}	constants	[-]
L	test section length	m
$\dot{m}$	mass flow rate	kg/s
Nu	Nusselt number	[-]
p	pressure	bar
Pch	Phase change number	[-]
Pe	Peclet number	[-]
Pr	Prandtl number	[-]
q	heat flux	W/m^2
R	radius	m
r	radial coordinate	m
Re	Reynolds number	[-]
S	perimeter	m
t	time	s
T	temperature	$^\circ C$
u	mean velocity	m/s
V	volume	m^3
We	Weber number	[-]

x	mass quality	[-]
z	axis coordinate	m

Greek symbols

α	void fraction	[-]
Γ	mass transfer	$kg/s/m^{-3}$
Δ	difference	
δ	liquid film thickness	m
ε	permittivity	[-]
ϕ	Martinelli's multiplier	[-]
λ	thermal conductivity	$W/m/K$
μ	dynamic viscosity	Pa/s
ν	kinematic viscosity	m^2/s
ρ	density	kg/m^{-3}
σ	surface tension	N/m
τ	shear stress	Pa

Subscripts

c	core or critic
$conv$	convective
$crit$	critic
exp	experimental
fr	frictional
g	gas
i	inner
i	interfacial
in	inlet conditions
l	liquid phase
lf	liquid film
liq	liquid phase
m	mixture
nb	nucleate boiling
o	outer
out	outlet conditions
sat	saturated conditions
sub	subcooled conditions
t	total
$theo$	theoretical
v	vapor phase
vap	vapor phase
w	wall

Acknowledgments

J'aimerais tout d'abord remercier ma directrice de thèse, Catherine Colin pour ces quatre années de travail. Je remercie également les membres du jury qui ont accepté d'évaluer mes travaux de thèse: Véronique Roig, Roberto Zenit et Julien Sebilleau. Merci aux rapporteurs, David Brutin et Nadia Caney pour leurs commentaires et leurs questions.

Je tiens particulièrement à remercier Greg, sans qui, la manip n'aurait jamais marché. Merci Gregorio de m'avoir appris le vocabulaire pour travailler tous les jours avec toi, pour les trajets en camion vers Bordeaux, pour le travail productif mais surtout pour les bons moments et les cours de culture française. J'aimerais également remercier Nabil Achour pour tout le travail qu'il a fait et d'avoir accepté le challenge de traiter les données de la caméra IR. J'aimerais aussi remercier Julien pour toute l'aide et le temps consacré à ma thèse. Merci à l'équipe de l'Atelier, Sébastien Cazin et Hervé Ayroles, pour la construction et l'installation expérimentale. Merci à Marie-Hélène pour l'aide qu'elle m'a fourni dans toutes les démarches administratives, et merci à toutes les personnes qui m'ont accueilli à l'IMFT et dans le groupe INTERFACE. Merci à toute l'équipe de Novespace à Bordeaux qui s'est occupée de BRASIL pendant les campagnes de vols paraboliques. Merci au CNES et à l'ESA pour les campagnes de vols et la caméra IR.

I would also like to thank the direct collaboration with Prof. Jungho Kim from the University of Maryland, who taught us the infrared thermography technique and helped us analyze the data behind the results. His very efficient explanations at conferences were crucial to the understanding of this method. I also want to thank from his research group Dr. Alexander Scammell and Caleb Hammer it was a pleasure working with them during the parabolic flight campaigns at NASA and at Novespace. Finally, I want to thank Mr. John McQuillen for taking care of the logistics at NASA, being the grant monitor of Alex and Caleb, he took care of Dong and me during our stay.

Así mismo, un agradecimiento merecido es dirigido al Consejo Nacional de Ciencia y Tecnología de México que me otorgó los medios financieros para obtener el doctorado en una institución extranjera.

Después de haber agradecido a las personas directamente involucradas, me gustaría, primero que nada, agradecer a mis padres, María de Lourdes Peimbert Tejeda y Onosandro Trejo Cerda, que aunque físicamente estuvieron lejos de todo esto, siempre me brindaron su apoyo de esa manera tan especial a la "Trejo-Peimbert" que nadie en el mundo entiende pero que es lo más importante para mi. Muchas gracias por sus consejos, sus puntos de vista, sus opiniones y sus llamadas de atención necesarias en mi crecimiento. A mi hermana Libna,

por haber estado conmigo el primer día en Francia y por cada llamada telefónica que hemos tenido, a Jack, thank you for the long talks and the interest on what I do. You guys are also far away but you always listened, sent me postcards and were there from beginning to end, so thanks a lot and I love you both. Me gustaría igual agradecer a Roberto Zenit por no haberme pedido mi opinión y haber escogido el IMFT por mí para hacer mi doctorado. No hubiera podido escogerlo mejor yo, that's for sure. A pesar de ya no ser mi asesor, gracias por haberme guiado en esta vida de la investigación, gracias por haberme dado consejos y estar al pendiente de mis francasos y avances al igual que haber formado parte del principio y el final de esta interesante aventura.

Antes de agradecer a las personas que compartieron conmigo los años de maestría-doctorado quiero darle las gracias a René, Adri, Fede, Lidia, Enrique, Ernesto y Dante porque desde París, Thuwal, Enschede, México o Toulouse me ayudaron y aconsejado en como lidiar con esto de la vida en el extranjero (Ja).

Depuis mon arrivée à l'IMFT, j'ai eu la chance de trouver des gens sympas, des permanents, des postdocs et des doctorants qui ont fait de ces années les plus intéressantes. Merci Benji, Lucía, René, Michel, Nico, Elise, Audrey, Auriane, Mathieu, Michaël, Véro R. (qui a partagé son bureau avec moi), Dominique L. et Patricia E.

Pendant la thèse: (tú primero) Seb (la personne qui a partagé le bureau le plus paisible d'INTERFACE avec "Shanti" et moi), Romain (mi esposo), Paul (chachacha), Caroline, Mijail et Marylou qui ont commencé la thèse avec moi. Flo (Pepis, que ahora habla el español más fluido del mundo #NuncaEnTuVida), Valentin (et Florie!), Clément, Alexis, Rafi, Elena, Emeryk, Adrien, mes remerciements vont aussi à vous. Merci tout le monde de m'avoir appris un peu de français. Also people like Anna García (Anna María de la Concepción Inmaculada), Edoardo Macchi, Vipul and Damien who shared the office and great moments with Seb and me.

Enfin, j'aimerais bien remercier ma belle-famille d'être là et pour les bons moments passés ensemble.

De igual manera hay gente que, sino participó directamente, siguió mis pasos. Gente que desde lejos, desde esa otra vida que llevaba en mi país no me dejó sola. Gente que me mandó mensajes y cartas. Gente que vino a visitarme en mi nueva vida y que vino a verme cuando me casé. Amigos que desde hace 10, 15 y hasta 20 años comparten momentos conmigo y que me enseñan siempre que una amistad se puede llevar incluso a 10 000 km de distancia. GRACIAS.

Special thanks to: Iñigo, Gonzalo, Angélica, Chawi, Sofía, Isabel, Peli, Mandy, Thalía, Amayali y Martha Maniwis.

Introduction

Two-phase gas-liquid or liquid-vapor flows are present in a very wide variety of industrial processes on ground and also in space applications. In normal gravity, gas-liquid flows have been studied by the petroleum, nuclear and chemical industries. The petroleum industry has studied two-phase flows of gas and crude oil through long pipelines before performing the separation of the components or products at the refinery. The nuclear industry has been concerned with system safety, with the primary intent of preventing dry out of the nuclear reactor in the case of loss of coolant accident for example. The chemical industries have managed gas-liquid contractors to increase interfacial heat and mass transfers in absorption, stripping and distillation processes that involve two-phase flow though complex geometries.

Two-phase flows with phase change are also present in space applications, in management of propellant in launchers with the transfer of fluid from the storage tank to the engines. The thermal control of electronic component satellites is ensured by liquid-vapor cooling systems such as heat pipes or loop heat pipes. Heat release is becoming a critical issue with the increase of the power of electronic components. In this context, the use of a two-phase mechanical pumped loop offers a significant reduction of weight and size, due to powerful heat transfer by latent heat. However, up to now, technical solutions involving the use of single-phase mechanical pumped loops are often preferred because of the lack of reliable predictive models for sizing the two-phase flow loops. Nevertheless, in the future, the use of two-phase mechanical pumped loop will become unavoidable for thermal management and also for power generation (from nuclear reactor) for the long-time missions. In order to properly design such systems under microgravity conditions it is necessary to be able to predict the pressure drop for sizing the pump, the heat transfer coefficient in convective condensation and boiling, and critical heat flux (CHF). Flow boiling is a complex phenomenon coupling hydrodynamics, heat and mass transfers, interfacial instability. Gravity strongly affects the fluid dynamics leading to non-predictable models. This has motivated studies in two-phase flows without and with phase change in microgravity for more than 40 years. First experiments were performed in drop towers, parabolic flights and last year by a team of Japanese scientists aboard the KIBO module of the International Space Station.

In Europe, researches on flow boiling in microgravity are coordinated in a MAP program of the European Space Agency. The study of flow boiling in microgravity started at the Institute of Fluid Mechanics in 2009 supported also by the national French space agency CNES. A two-phase flow loop for parabolic flights experiments BRASIL was built during the PhD Thesis of Marine Narcy [64]. It allows to study flow boiling of HFE7000 in a tube of 6 mm diameter. This program continues in the present thesis. In the frame of

a collaboration with the University of Maryland a new test section for the measurement of the heat transfer coefficient by infrared thermography was implemented in BRASIL. This allows to evaluate and compare 2 measurement techniques which could be used in the future European flow boiling experiments on Heat Transfer Host aboard the International Space Station.

The first chapter is devoted to an overview of the main equations governing the two-phase flows with phase change and the classical models for the closure laws on void fraction, wall friction and heat transfer coefficient. Since the literature on this domain is very wide, the description of the state of art in this chapter will not be exhaustive. It will be focus on two-phase flows in axisymetric configurations, in vertical upward flow and mainly in microgravity conditions. The study reported in normal gravity conditions will be used as reference for comparison with microgravity conditions. Recent studies on flow boiling in microgravity will be presented at the end of the chapter. The flow boiling loop BRASIL and the measurements techniques are described in Chapter 2. The design of the capacitance probes for the measurement of the void fraction has been improved. The two sections for the measurement of heat transfer coefficient are described. A post-processing for infrared thermography measurements has been developed. Then the accuracy of the measurement techniques is carefully evaluated. The experimental results on the flow patterns, void fraction, liquid film thickness in annular flow and heat transfer coefficient are presented in Chapter 3. The influence of liquid mass flux, heat flux, quality and gravity on heat transfer coefficient is discussed. Finally, the structure of the liquid film in annular flow is studied from image processing. Disturbance waves velocities and frequencies are determined from space-time diagrams.

Chapter 1

Flow boiling: Description and modelling

The description and modeling of two-phase gas-liquid flow is very complex and numerous studies have been performed in the last decades on two-phase adiabatic gas-liquid flows and on flow boiling. Since the literature on this domain is very wide, the description of the state of the art in this chapter will not be exhaustive. It will be focused on two-phase flows in axisymetric configurations, in vertical upward flow and mainly in microgravity conditions. The study reported in normal gravity conditions will be used as reference for comparison with microgravity. In this chapter we will first describe the mean equations of mass and energy conservation and momentum balance averaged in the tube cross section for the gas and the liquid phases. These equations will be used to predict the mean gas and liquid velocities, the evolution of the pressure along the tube and the evolution of the wall temperature in the case of a wall heated at a constant heat flux. To solve these equations, some closure laws are required to estimate the void fraction, the wall shear stress and the heat transfer coefficient. These closure laws are strongly dependent on the flow pattern which will be described in adiabatic flow and in flow boiling. Some of these models will be presented in this chapter with a focus on two-phase flows in microgravity.

1.1 Fundamental description: basic equations and closure laws

To be able to describe the dynamics and heat transfer of flow boiling, a simplified one-dimensional set of equations of the two-phase flow can be used. These equations involve several parameters defined in this section. Two-phase flow is circulating in a tube of diameter D, cross section A, with a mass flux $\dot{m}$ which is a sum of the liquid mass flow rate, $\dot{m}_l$ and the vapor or gas mass flow rate $\dot{m}_v$ The vapor quality $x_v = x$ is equal to $\dot{m}_v/\dot{m}$. The mass flux G is defined as $G = \dot{m}/A$.

1.1.1 Conservation of mass

The volume gas fraction α is defined as follows. If the cross-sectional area of the channel is A and the cross-sectional areas occupied by the gas and liquid phases are A_v and A_l respectively then the void fraction is [25]:

$$\alpha = \alpha_v = \frac{A_v}{A} \tag{1.1}$$

$$\alpha_l = (1 - \alpha) = \frac{A_l}{A} \tag{1.2}$$

The mass conservation equation for phase k (with $k = l$ for liquid, and $k = v$ for vapor) is written as:

$$\frac{\partial \alpha_k \rho_k}{\partial t} + \frac{\partial \alpha_k \rho_k u_k}{\partial z} + \Gamma_k = 0 \tag{1.3}$$

where Γ_k is the interfacial mass transfer rate of the phase k, ρ_k represents the density of the phase k and u_k its axial velocity averaged over A_k in the flow direction z.

$$u_k = \frac{\dot{m}_k}{A \rho_k \alpha_k} = \frac{x_k \dot{m}}{A \rho_k \alpha_k} = \frac{x_k G}{\rho_k \alpha_k} \tag{1.4}$$

1.1.2 Momentum balance

The momentum balance of each phase k can be written as:

$$\frac{\partial \alpha_k \rho_k u_k}{\partial t} + \frac{\partial \alpha_k \rho_k u_k^2}{\partial z} + \alpha_k \frac{\partial p}{\partial z} - \tau_{w,k} \frac{S_{w,k}}{A} - \tau_{i,k} \frac{S_{i,k}}{A} + \alpha_k \rho_k g - \Gamma_k u_i = 0 \tag{1.5}$$

where p is the mean pressure in the cross-section A, $\tau_{w,k}$ is the wall shear stress over the perimeter $S_{w,k}$ wetted by the phase k, $\tau_{i,k}$ the interfacial shear stress over the interfacial perimeter $S_{i,k}$ and u_i the velocity of the interface in the flow direction. The gravitational acceleration is denoted by g and has a value of 9.81 m/s^2 for normal gravity and 0 m/s^2 for microgravity conditions.

In bubbly and slug flow, a momentum balance equation for the mixture is commonly used, since the mean gas and mean liquid velocities can be linked together by using a drift-flux model.

1.1.3 Enthalpy balance

The total enthalpy of each phase $h_{t,k}$, is determined as the sum of the enthalpy, the kinetic energy, and the potential energy of phase k. Its temporal variation is due to an enthal-

phy change through advection, wall and interfacial heat fluxes, energy associated to mass transfer, pressure or volumetric forces, and friction at the interface.

$$\frac{\partial \alpha_k \rho_k h_{t,k}}{\partial t} + \frac{\partial \alpha_k \rho_k h_{t,k}^2}{\partial z} = \frac{q_{w,k} S_{w,k}}{A} + \frac{q_{i,k} S_{i,k}}{A} + \alpha_k \frac{\partial p_k}{\partial t} + \xi \frac{\tau_{i,k} S_i u_i}{A} + \alpha_k \rho_k g u_k + \Gamma_k h_{t,k,sat} \quad (1.6)$$

where $q_{w,k}$ is the heat wall transfer and $q_{i,k}$ the interfacial heat transfer, and $h_{t,k,sat}$ is the total enthalpy of phase k at the interface assumed at the saturation temperature. In the following, the total enthalpy $h_{t,k}$ will be assumed equal to the enthalpy of phase k, the pressure variation with time will be neglected as well as the power of the gravity force and the interfacial friction.

In saturated boiling the enthalpy of the liquid and vapor phases are equal to the enthalpy at saturation conditions $h_{v,sat}$ and $h_{l,sat}$. Then the enthalpy balance equation reduces to a simple equation given the evolution of the vapor quality x along the pipe heated with heat flux $q = q_w$:

$$\frac{4q}{D} = G(h_{v,sat} - h_{l,sat})\frac{dx}{dz} = G h_{lv} \frac{dx}{dz} \quad (1.7)$$

where h_{lv} is enthalpy of the phase change. This equation is linked to the mass balance equation for the vapor or liquid phase since $\Gamma_v = G\frac{dx}{dz}$.

The closure law required for solving these equations are dependent of the flow configuration described hereafter.

1.2 Flow patterns description

When a liquid is vaporized in a heated channel the liquid and the generated vapor take up a variety of configurations known as a flow pattern. The particular flow pattern depends on the conditions of pressure, liquid and vapor flow rates, channel geometry, thermodynamics and transport properties of the phases. Flow boiling is characterized by a strong evolution of the flow patterns all along the tube, as shown in Fig. 1.1.

Let us first consider the flow patterns observed in adiabatic flow. A first description of the flow pattern in vertical upward flows was provided by Taitel et al. [79] for an air-water flow in a pipe of 5 cm diameter.

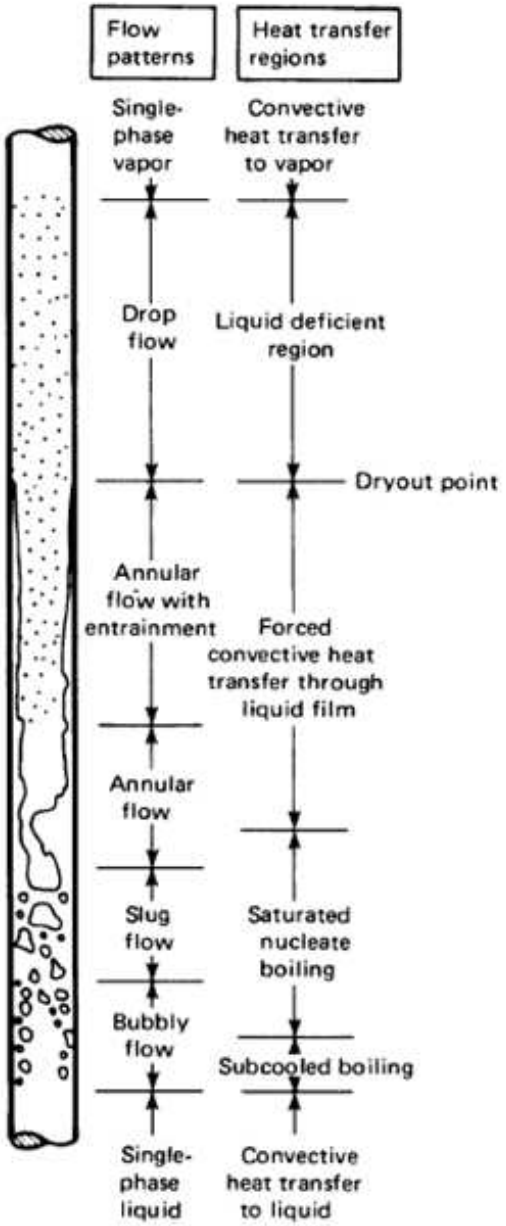

Figure 1.1: Flow pattern structures along a channel.

Flow patterns encountered in vertical upward flow are shown schematically in Fig. 1.2.

- *Bubbly flow.* In bubbly flow, gas or vapor phase is distributed as discrete bubbles in

a continuous liquid phase. For high liquid flow rate the bubbles may be smaller and spherical and for low liquid flow rate the bubbles may be large with a spherical cap and a flat tail.

- *Slug flow.* In slug flow the gas or vapor bubbles are longer than the diameter of the pipe. The nose of the bubble has a characteristic spherical cap and the gas in the bubble is separated from the pipe wall by a slowly descending liquid film in vertical upward flow. The liquid flow is contained in liquid slugs which separate successive gas bubbles, these slugs may or may not contain smaller entrained gas bubbles carried in the wake of the large bubbles. The length of the main gas bubble can vary considerably [25].

- *Churn flow.* Churn flow is formed by the breakdown of the large vapor bubbles in slug flow. The gas or vapor flows in a more or less chaotic manner through the liquid which is mainly displaced to the channel wall, the flow has an oscillatory or time varying character: hence, the descriptive name churn flow. This region is also sometimes referred to as semi-annular or slug-annular flow [25].

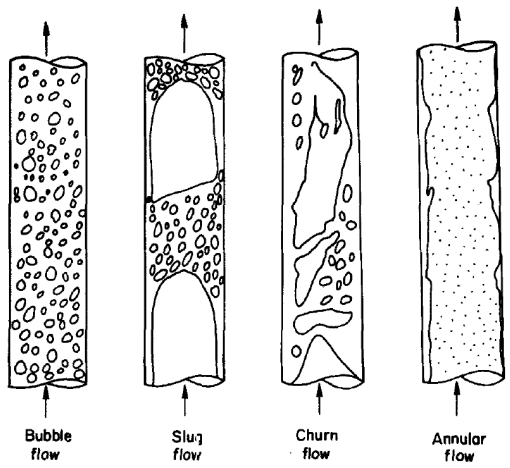

Figure 1.2: Flow patterns of a vertical flow according to Taitel et al. [79].

- *Annular flow.* In annular flows, a liquid film forms at the pipe wall with a continuous central gas or vapor core. Large amplitude coherent waves are usually present on the surface of the film and the continuous break up of these waves may lead to droplet entrainment in the central gas core (wispy-annular pattern) [25].

These flow patterns are generic. They are also observed for smaller diameter tubes and with other fluids, as refrigerants, Chen et al. [17].

The same flow regimes are observed in microgravity conditions. There are nonetheless some difference observed during the absence of gravity. Several studies were performed in the 1990's and early 2000's on gas-liquid adiabatic flows, in tubes of 6–40 mm inner diameter (Dukler et al., [31]; Colin et al., [23],[24]; Huckerby and Rezkallah [42]; Zhao and Rezkallah, [86]; Bousman et al. [10]; Zhao et al. [87]).

In flow boiling, because of the heated wall, the vapor mass flow rate increases along the pipe, and different flow patterns are observed as shown in Fig. 1.1. The presence of a heat flux through the channel wall alters the flow pattern with bubble nucleation at the wall that is observed in bubbly and slug flow. In annular flow, at high vapor velocities, the liquid film at the wall can completely evaporate leading to a dry-out of the wall and a mist flow as observed in Fig. 1.3. Despite these main differences at low wall heat flux, similar flow patterns are observed in adiabatic two-phase flows and in flow boiling.

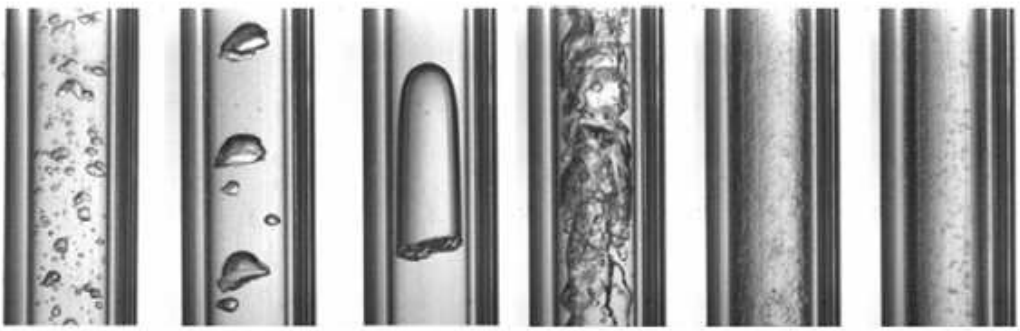

Figure 1.3: Flow patterns observed in 4.26 mm diameter tube with R134a at 6 bar (Chen et al. [17].

1.3 Regime transition criteria

Studies on flow regime transition criteria for upward two-phase flow in a vertical tube have been performed for the last 30 years. Internal structures of two-phase flows are classified by the flow patterns. Traditionally flow regimes are identified from a map obtained from experimental observations [87], [17], .

Taitel et al. regimes transition and Chen et al. work

Classical flow pattern map are plotted using coordinates based on the superficial liquid velocity (j_l or U_{LS}) and superficial gas velocity (j_v or U_{GS}). Taitel et al. [79] proposed a flow pattern map and a transition flow criteria for air-water flows.

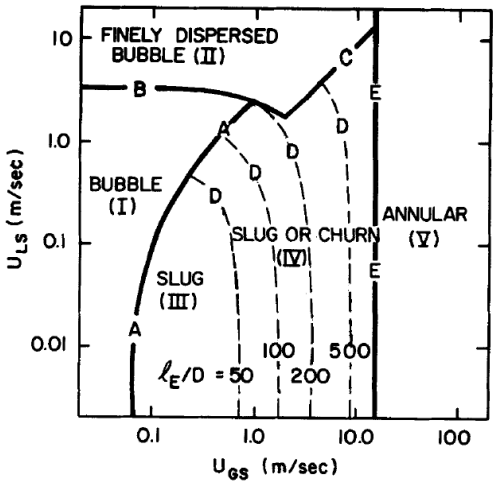

Figure 1.4: Flow pattern map according to Taitel et al. [79] for an air-water vertical flow at a 5 *cm* diameter tube.

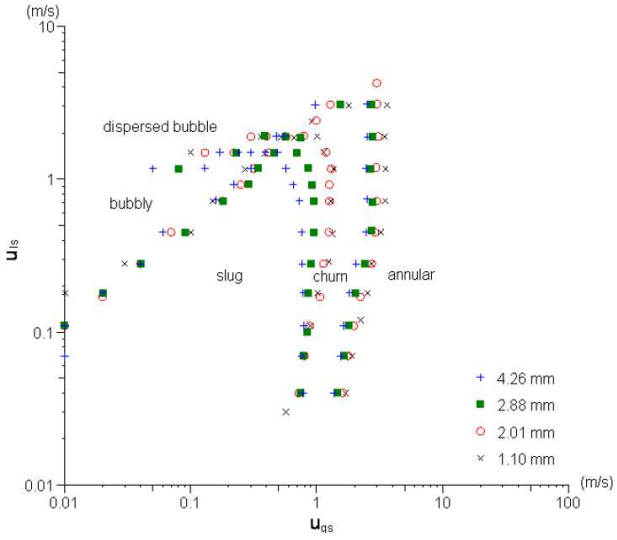

Figure 1.5: Chen's study to determine regimes transitions for different tube diameters [17].

In Fig. 1.5, there is a typical flow pattern maps for a boiling flow of R134a in tubes of 1.10 *mm* to 4.26 *mm* diameter obtained by Chen et al. [17]. The flow patterns are observed in an adiabatic test section. The transition from bubbly to slug flows and from churn to annular flow is not very sensitive to the tube diameter. The impact of the tube diameter is more visible on the transition from slug to churn flows.

Similar flow pattern maps were also observed in microgravity conditions for adiabatic flows

and flow boiling. Several authors tried to predict the transition between the flow patterns, Dukler et al. [31], Ohta [66].

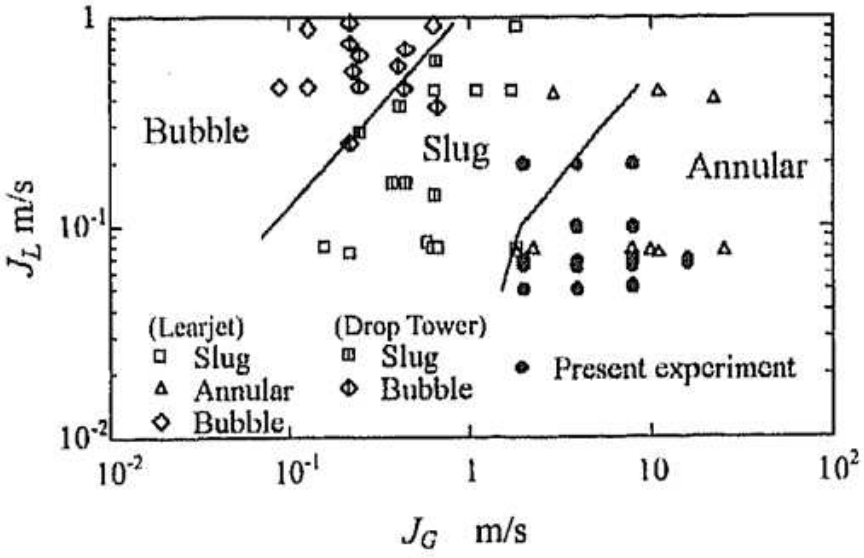

Figure 1.6: Dukler's regimes transitions in microgravity compared to Ohta's work marked as Present experiment [66].

Transition bubbly to slug flow

For upward vertical flow a transition between bubbly and slug flow, for an air/water flow appears for a void fraction $\alpha = 0.3$.

Taitel et al. [79] found that the transition occurs for a critical value of the void fraction $\alpha = 0.25$ They used a relative velocity correlation to convert into a conventional form based on the superficial velocities of liquid and gas:

$$j_l = 3j_v - 1.15 \left[\frac{g\left(\rho_l - \rho_v\right)\sigma}{\rho_l}^{1/4} \right] \tag{1.8}$$

This value was also explained and obtained from a very simple geometrical consideration. Mishima and Ishii [60] considered a tetrahedral form for bubble packing and coalescence pattern. If the possible gap between two bubbles, l, becomes less than a bubble diameter $2r_b$, the critical void fraction writes:

$$\alpha = \left(\frac{2}{3}\right)^3 = 0.296 \simeq 0.3 \tag{1.9}$$

In microgravity conditions, transition criteria is defined for air-water flows using either a critical value of the void fraction, like Dukler et al. [31] and Colin et al. [23], or a critical value of the Weber Number, We_c, like Zhao and Rezkallah [86]. Transition from bubbly to slug flow is progressive and with the increase of coalescence, the size of the bubble increases along the tube. Coalescence is the basic mechanism responsible for the transition and it has been characterized by the Ohnesorge number, Colin et al. [24], $Oh = \nu_L \sqrt{\rho_L}/\sigma D$ based on liquid properties and the tube diameter D.

Two different regimes were identified, inhibiting coalescence ($Oh > 8.2 \times 10^{-4}$) and promoting coalescence ($Oh < 7.6 \times 10^{-4}$) regime. For cases of gas-liquid flows, a critical void fraction value of 0.45 was the transition value due to coalescence where the regime was inhibiting coalescence. For a promoting coalescence regime the transition occurred around $\alpha \approx 0.2$. In flow boiling however, the void fraction at transition is close to 0.7, according to Narcy et al. [61] and Celata and Zummo [12], which is much higher than the value obtained in adiabatic air-water flow by Colin et al. [24] or Mishima and Ishii [60].

The origin of this particular value comes from sphere-packing theory according to Celata and Zummo [12] Fig. 1.7. When the void fraction of a bubbly flow exceeds the limit value, coalescence takes place for small bubbles and Taylor bubbles appear in the flow.

The relation between the superficial velocities at the transition is usually calculated using the drift-flux model of Zuber and Findlay [89] Eq. 1.22 to 1.24.

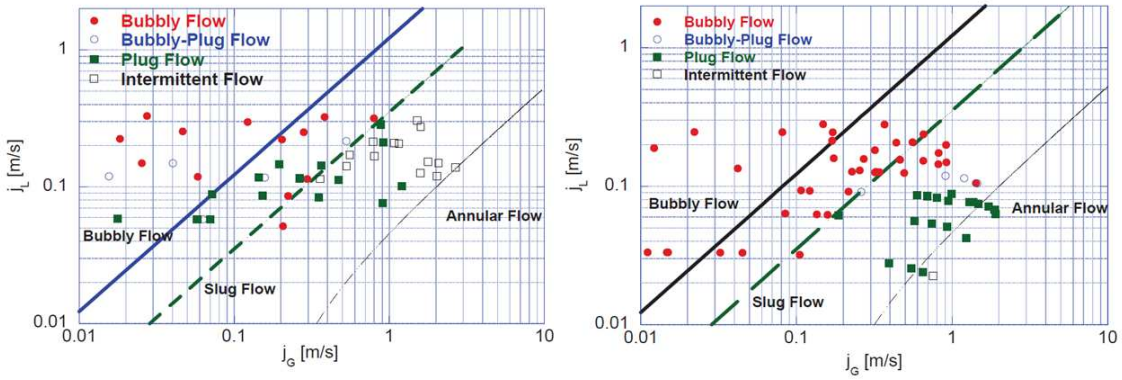

Figure 1.7: Results obtained by Celata and Zummo on regime transitions [12].

Other authors like Zhao and Rezkallah [86], also plotted the flow pattern maps versus dimensionless numbers such as the Weber number.

Critical Weber number by Rezkallah

Zhao and Rezkallah reported experimental data on gas-liquid flow under microgravity conditions and suggested a model of prediction of flow pattern transitions based on an analysis

of the forces acting on the mixture. According to the authors, the Weber number, defined by the ratio between inertial forces over surface tension, plays an important role in microgravity when the buoyancy force is negligible. They therefore proposed a transition criteria based on a critical Weber number We_c calculated with the superficial gas velocity j_v and density ρ_v.

$$We_c = \frac{\rho_v j_v^2 D}{\sigma} \tag{1.10}$$

For bubbly and slug flow, the transition are observed for $We_c < 1$, where the surface tension force is higher than the inertial force. For a We_c between 1 and 20 inertia and surface tension forces lead to a large transition with frothy slug-annular flow that correspond to the beginning of the transition from slug flow to annular flow. The annular region is characterized by values of the $We_c > 20$ and important inertial forces.

In Fig. 1.8 Rezkallah [71] put together different experimental data to compare with the criteria proposed by Zhao and Rezkallah [86].

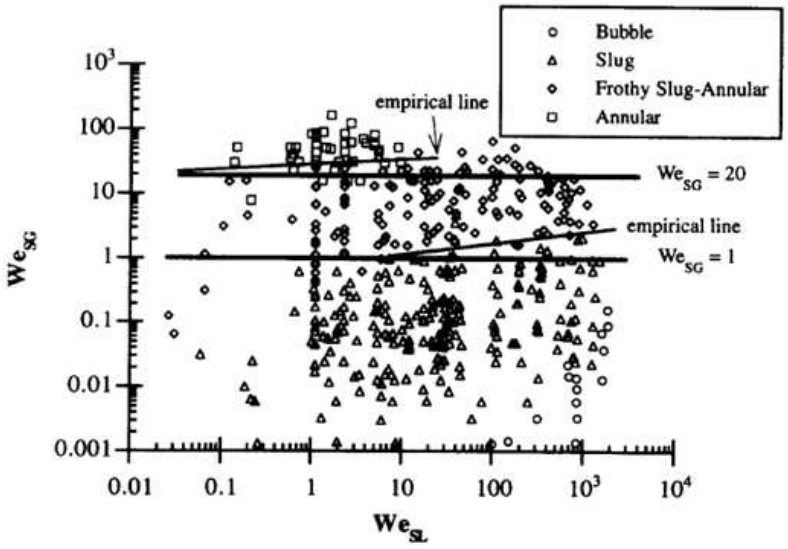

Figure 1.8: Rezkallah and Zhao's critical We number criteria for microgravity flow pattern maps with water-air [71]

After comparing different data sets, transition from bubbly to slug flow was shown to occur at a constant value of the We_c, which is based on the actual gas velocity, of about 2 and from frothy slug-annular was found to be at 20.

Jayawardena et al. regimes transition

For microgravity cases, Jayawardena et al. [46] suggested an approach with dimensionless numbers and showed that for smooth pipes, there were different dimensionless groups that influence the transition. Also noted that the pipe diameter and the flow conditions were such that there is no dominance of the capillary effects and correlated the flow pattern maps in terms of the Weber number and the Reynolds number. Fig. 1.9 shows a flow pattern map for microgravity conditions of a two-phase flow suggesting that the transition can be predicted in this way. The experiments came from different research groups that work with air-water mixtures and liquid-vapor flows: Janicot [45], Bousman [11], Colin [22], Zhao and Rezkallah [86], Reinarts [70], Hill and Best [41], and Chen et al. [16].

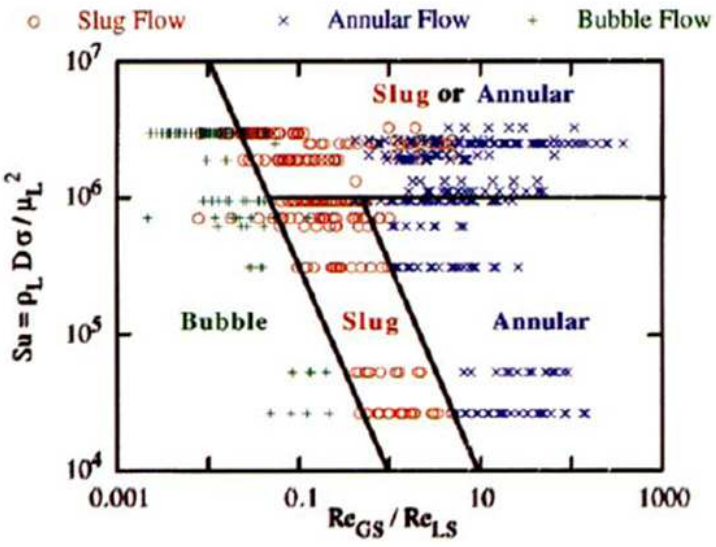

Figure 1.9: Jayawardena's Model

Where Su in literature is the Suratman number, the reciprocal of the square root of is the Ohnesorge number used by Colin et al. [24]. For a bubbly-slug transition:

$$\frac{Re_{GS}}{Re_{LS}} = K_1 \; Su^{2/3} \tag{1.11}$$

where the value of K_1 is equal to 464.16.

Transition slug/churn to annular flow

According to Dukler et al. [31] for microgravity flows the transition from slug to annular flow can be calculated by equaling the void fraction values in slug flow (1.22) and the void

fraction calculated in annular flow :

$$\frac{\alpha^{5/2}}{(1-\alpha)^2} = \frac{f_i}{f_w}\frac{\rho_v}{\rho_l}\left(\frac{j_v}{j_L}\right)^2 \tag{1.12}$$

This equation is obtained from the momentum balance equations for liquid and vapor in annular flow, which are combined to eliminate the pressure gradient:

$$\tau_i = \tau_w\sqrt{\alpha} \tag{1.13}$$

$$\frac{1}{2}\ f_i\ \rho_v\ \frac{j_v^2}{\alpha^2} = \frac{1}{2}\ f_w\ \rho_L\ \frac{j_L^2}{(1-\alpha)^2}\sqrt{\alpha} \tag{1.14}$$

Where f_w and f_i are the wall and interfacial friction factors equal to:

$$f_w = \frac{16}{Re_L}^{\ n} \tag{1.15}$$

for laminar flow, and for turbulent flow:

$$f_w = 0.079 Re_L^{-1/4} \tag{1.16}$$

used for a smooth tube surface, and:

$$\frac{f_i}{f_v} = 1 + 150\left(1-\alpha^{1/2}\right) \tag{1.17}$$

is the empirical correlation by Wallis [80], where f_v is the single-phase friction factor for the vapor flow. Dukler et al. [31] found a transition value of $\alpha = 0.8$ for a slug to annular flow, from Eq. 1.12. Zhao and Rezkallah [86] consider that the transition to annular flow occurs for a Weber number for the vapor greater than 20. Jayawardena et al. [46] proposed 2 correlations to predict the transition from slug to annular flow depending on the Suratman number value:

$$\frac{Re_{GS}}{Re_{LS}} = K_2 Su^{-2/3} \quad if \quad Su < 10^6 \tag{1.18}$$

$$\frac{Re_{GS}}{Re_{LS}} = K_3 Su^2 \quad for \quad Su > 10^6 \tag{1.19}$$

With $K_2 = 4641.6$ and $K_3 = 2\text{x}10^9$.

1.4 Void Fraction and film thickness

1.4.1 Void fraction

Void fraction can be measured using different methods like conductance probes [10] [23], capacitance probes [61] [32] or flow visualizations. These techniques measure the averaged value of the void fraction α in the tube's cross-section.

Homogeneous Model

The homogeneous model assumes that the two phases have the same average velocity. It can be considered that there is only one phase with the properties of a liquid-vapor mixture.

$$U_l = U_v = U_M \tag{1.20}$$

The homogeneous model can be used mainly in dispersed bubbly or droplet flows when the relative velocity is small compared to the carrying phase velocity as well as when they are in microgravity conditions.

A momentum balance equation can be written as:

$$\frac{\partial \rho_M U_M}{\partial t} + \frac{\partial}{\partial z}\left[\rho_M U_M^2\right] = \frac{\partial G}{\partial t} + \frac{\partial}{\partial z}\left[\frac{\partial G}{\rho_M}\right] = \frac{dP}{dz} + \frac{\tau_p S_p}{A} - \rho_M g \sin\theta \tag{1.21}$$

where $\rho_M = \rho_v \alpha + \rho_L(1-\alpha)$ is the density of the mixture.

Drift-flux Model

This model is suitable for moderate liquid velocities in bubbly or slug flow regimes where the drift velocity between gas and liquid phases is well observed. The drift flux model stated that the actual vapor velocity u_v responds in slug flow, to the axial center line flow velocity in the tube which is larger than the mixture velocity j. Due to buoyancy effects, bubbles experience a drift velocity U_∞. For a vertical flow the vapor velocity becomes:

$$U_v = \frac{j_v}{\alpha} = C_0 j + U_\infty \tag{1.22}$$

C_0 depends on the local void fraction and vapor velocity distribution. U_∞ is adapted to the flow pattern:

$$U_\infty = 1.53\left(g\left(\rho_l - \rho_v\right)\frac{\sigma}{\rho_l^2}\right)^1/4 \qquad \text{for bubbly flows} \tag{1.23}$$

$$0.35\sqrt{gD} \qquad \text{for slug flows} \tag{1.24}$$

the drift flux expression to obtain α as a function of x with a distribution coefficient and a drift velocity u_∞ for normal gravity is:

$$\alpha = \frac{1/C_0}{1 + \left(\frac{\rho_v}{\rho_l} + \frac{u_\infty \rho_v}{G}\right)\frac{1}{x}\frac{\rho_v}{\rho_l}} \tag{1.25}$$

Bhagwat and Ghajar's Model

Bhagwat and Ghajar [9] revised different drift flux based models and proposed a new one validated for a large range of fluid properties, inclination, diameter of the pipe and independent of the flow pattern.

$$U_{gm} = (0.35 \sin\theta + 0.45 \cos\theta)\sqrt{\frac{gD\,(\rho_l - \rho_v)}{\rho_l}\,(1-\alpha)^{0.5}}\,C_2 C_3 C_4 \tag{1.26}$$

where the pipe orientation term θ is measured from the horizontal and the variables C_2, C_3 and C_4 are defined by

$$C_2 = \frac{0.434}{log_{10}\,(\mu/0.001)}^{0.15} \qquad (\mu/0.001) > 10 \tag{1.27}$$

$$C_2 = 1 \qquad (\mu/0.001) \leq 10 \tag{1.28}$$

$$C_3 = (La/0.025) \;\; La < 10 \tag{1.29}$$

$$C_3 = 1 \qquad La \geq 10 \tag{1.30}$$

The Laplace variable La used is essentially the inverse of the non-dimensional hydraulic pipe diameter defined by Kataoka and Ishii [48] and is defined as $La = \sqrt{\sigma/\,(g\Delta\rho)}/D$

$$C_4 = 1 \tag{1.31}$$

$$C_4 = -1 \text{ for } (0^\circ > \theta - 50^\circ \text{and } Fr_{sg} \leq 0.1 \tag{1.32}$$

Awad and Muzychka's Model

Awad and Muzychka, based on turbulent liquid and vapor flows assumptions, give an expression for two-phase frictional gradient and void fraction in circular pipes. It is developed to obtained the range of data where the majority of points are expected. Then the limits, or upper and lower bound are averaged to obtain an acceptable prediction.

$$\alpha_{lower} \leq \alpha \leq \alpha_{upper} \tag{1.33}$$

The bounds model is also presented in terms of the Lockhart-Martinelli parameter, X, explained later in the Wall shear stress section. So for a lower bound α writes:

$$\alpha = \frac{1}{1 + X^{16/19}} \tag{1.34}$$

and the upper bound:

$$\alpha = \frac{1}{1 + 0.28X^{0.71}} \tag{1.35}$$

After averaging the two bounds, a simple model is defined as follows:

$$\alpha_{average} = \frac{0.5}{1 + 0.28X^{0.71}} + \frac{0.5}{1 + X^{16/19}} \tag{1.36}$$

or:

$$\begin{aligned} \alpha_{average} = & \frac{0.5}{1 + 0.28\left[(1 - x/x)^{7/8}\left(\rho_v/\rho_l\right)^{1/2}\left(\mu_l/\mu_v\right)^{1/8}\right]^{0.71}} \\ & + \frac{0.5}{1 + \left[(1 - x/x)^{7/8}\left(\rho_v/\rho_l\right)^{1/2}\left(\mu_l/\mu_v\right)^{1/8}\right]^{16/19}} \end{aligned} \tag{1.37}$$

Cioncolini and Thome's Model

Cioncolini and Thome [21] proposed a correlation to predict the void fraction, in annular flows, based on a wide data bank where α is given by:

$$\alpha = \frac{hx^n}{1 + (h - 1)\, x^n} \tag{1.38}$$

where

$$h = \; a + (1 - a)\left(\frac{\rho_v}{\rho_l}\right)^{a_1} \qquad a = -2.129 \;\; a_1 = -0.2186 \tag{1.39}$$

$$n = \; b + (1 - b)\left(\frac{\rho_v}{\rho_l}\right)^{b_1} \qquad b = 0.3487 \;\; b_1 = 0.515 \tag{1.40}$$

Recently, Gomyo and Asano [4] performed void fraction measurements in two-phase adiabatic flows with capacitance probes and compared their measurements to some of these correlations. Cioncolini and Thome's, and Awad and Muzychka's proposed correlations provide the best predictions for the void fraction. But some discrepancy is observed for lower mass fluxes as we can see in Fig. 1.10

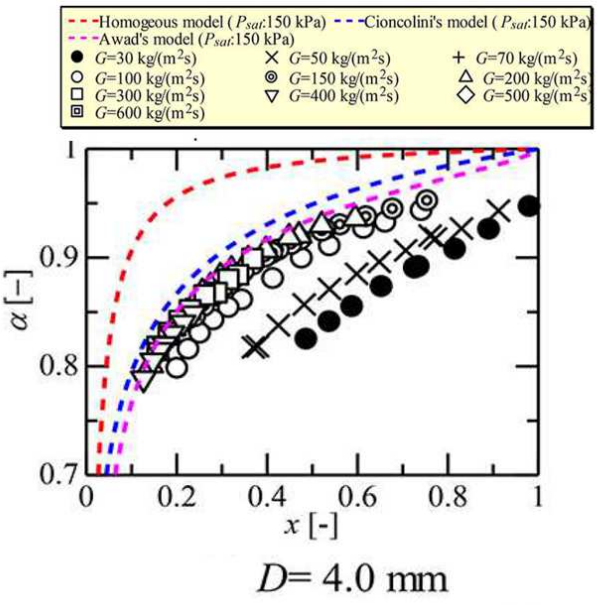

Figure 1.10: Comparison with experimental data from Gomyo and Asano[4].

1.4.2 Liquid film thickness in annular flows

In annular flow, a liquid film of thickness δ is flowing along the wall and a vapor core in the pipe center. The thickness of the liquid film is controlled by a balance between the wall shear stress, the interfacial shear stress and the weight of the liquid film.

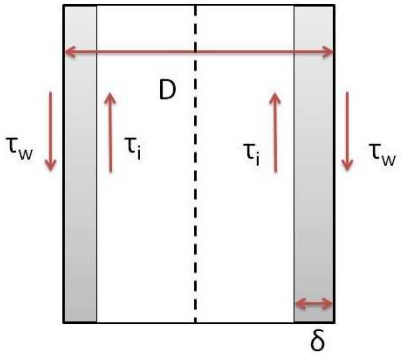

Figure 1.11: Simplified model of annular flow.

Since the vapor velocity is much higher than the liquid velocity it is necessary to apply a

two-fluids model with two equations for the momentum balance for each phase and not a momentum balance for the mixture assuming a relation between the mean velocity of gas and liquid. As shown in Fig. 1.11 in annular flow in a vertical tube of diameter D, where the existence of droplets in the vapor is neglected, the film thickness δ, can be related to the void fraction $\alpha_v = \alpha$ according to the following equation.

$$\delta = \frac{D}{2}\left(1 - \sqrt{\alpha}\right) \tag{1.41}$$

When the entrainment rate of droplets is not negligible, it has to be removed from the total liquid hold up. To calculate the liquid film thickness the equation becomes:

$$\delta = \frac{D}{2}\left(1 - \sqrt{\alpha\left(1 + \frac{\rho_v}{\rho_l}\frac{1-x}{x}e\right)}\right) \tag{1.42}$$

An expression of the entrainment rate is given by [20]:

$$e = \left(1 + 279.6We_c^{-0.8305}\right)^{-2.209} \qquad \text{for } 10 < We_c < 10^5 \tag{1.43}$$

where We_c is the Weber number of the vapor core

$$We_c = \frac{\rho_c j_v^2 D}{\sigma} \tag{1.44}$$

based on the superficial vapor velocity and the density ρ_c of the gas core carrying liquid droplets:

$$\rho_c = \frac{e\,(1-x) + x}{\frac{e(1-x)+x}{\rho_l} + \frac{x}{\rho_v}} \tag{1.45}$$

In annular flows it is also possible to calculate the void fraction from the momentum balance equation for the liquid and the vapor:

$$\left.\begin{aligned} \frac{\partial \alpha \rho_v u_v^2}{\partial z} &= -\alpha\frac{\partial p}{\partial z} + \frac{4}{D}\sqrt{\alpha}\tau_i - \rho_v \alpha g + \Gamma u_i, \\ \frac{\partial \rho_l (1-\alpha) u_l^2}{\partial z} &= -(1-\alpha)\frac{\partial p}{\partial z} + \frac{4}{D}\tau_w + \frac{4}{D}\sqrt{\alpha}\tau_i - \rho_l(1-\alpha)g - \Gamma u_i, \end{aligned}\right\} \tag{1.46}$$

To solve this equation and be able to calculate the pressure drop and liquid film thickness (or void fraction), closure laws for the wall shear stress τ_w and the interfacial shear stress τ_i are required.

The void fraction calculated from Eq. 1.46 is very sensitive to the modeling of τ_w and τ_i and it is often more precise to use a specific correlation to predict the void fraction.

1.5 Wall shear stress

Two classical type of model are used to estimate the wall shear stress. Homogeneous flows models or separated flow models as Lockhart and Martinelli types.

1.5.1 Homogeneous flow models

In this model, both liquid and vapor phases are assumed to move at the same velocity. The fluid obeys the conventional equations of a single-phase flow and is characterized by suitably averaged properties of the liquid and vapor phases.

The frictional pressure drop for a steady flow in a channel with a constant cross sectional area is [13]:

$$\left(\frac{dP}{dz}\right)_{fr} = \frac{2 f_{tp} G^2}{d_h \rho_{tp}} \tag{1.47}$$

where, $d_h = D$ is the hydraulic diameter, ρ_{tp} is the two-phase mixture density is given by several different correlations as for example:

$$\rho_{tp} = \left(\frac{x}{\rho_v} + \frac{1-x}{\rho_l}\right)^{-1} \quad \text{or} \quad \rho_{tp} = \left(\alpha \rho_v + (1-\alpha)\,\rho_l\right) \tag{1.48}$$

and f_{tp} the two-phase friction factor given by:

$$f_{tp} = \frac{16}{Re_{tp}} \quad for \quad Re_{tp} < 2000 \tag{1.49}$$

$$f_{tp} = \frac{0.079}{Re_{tp}^{0.25}} \quad for \quad Re_{tp} > 2000 \tag{1.50}$$

where Re_{tp} is:

$$Re_{tp} = \frac{G d_h}{\mu_{tp}} \tag{1.51}$$

Several models exist for the expression of the mixture density and viscosity versus the liquid and vapor properties and the void fraction or the quality. This expressions are usually obtained from empirical correlations and data sets written accordingly. Expressions are proposed by McAdams et al. [59], Dukler et al. [30], Lin et al. [55], Awad and Muzychka [5], García et al. [34].

1.5.2 Separate flow models

Lockhart-Martinelli's correlation

Lockhart-Martinelli's correlation [57] is widely used for predicting the wall friction in boiling flows. In this separate flow model the two-phase frictional pressure gradient $\left(\frac{dp}{dz}\right)_{fr}$ is assumed to be related to single-phase flow frictional pressure gradient $\left(\frac{dp}{dz}\right)_l$ or $\left(\frac{dp}{dz}\right)_v$ obtained if the liquid or the vapor were flowing alone in the pipe. Interactions between the phases are thus ignored.

The Lockhart-Martinelli correlation is based on a two-phase multiplier for the liquid phase ϕ_l^2 or vapor phase ϕ_v^2. The two-phase frictional pressure gradient can be written:

$$\left(\frac{dp}{dz}\right)_{fr} = \frac{4}{D}\tau_w = \phi_l^2 \left(\frac{dp}{dz}\right)_l = \phi_v^2 \left(\frac{dp}{dz}\right)_v \tag{1.52}$$

Where the pressure gradients are:

$$\left(\frac{dp}{dz}\right)_l = -\frac{4}{D} f_{w,l} \frac{\rho_l j_l^2}{2} \tag{1.53}$$

$$\left(\frac{dp}{dz}\right)_v = -\frac{4}{D} f_{w,v} \frac{\rho_v j_v^2}{2} \tag{1.54}$$

The single phase friction factors $f_{w,k}$ with $k = l$ for the liquid and $k = v$ for the vapor phase.

$$f_{w,k} = K \left(\frac{j_k D}{\nu_k}\right)^{-n} \tag{1.55}$$

K is equal to 16 in laminar flow and 0.079 in turbulent flow and n is equal to 1 in laminar flow and to 0.25 in turbulent flow.

The corresponding two-phase multipliers are:

$$\phi_l^2 = \left(1 + \frac{C}{X} + \frac{1}{X^2}\right) \tag{1.56}$$

$$\phi_v^2 = (1 + CX + X^2) \tag{1.57}$$

Where X is the Martinelli parameter for both phases defined as

$$X = \left[\frac{\left(\frac{dp}{dz}\right)_l}{\left(\frac{dp}{dz}\right)_v}\right]^{1/2} = \frac{j_l}{j_v}\sqrt{\frac{\rho_l}{\rho_v}\frac{f_{w,l}}{f_{w,v}}} \tag{1.58}$$

And the value of C depends on the regimes of the liquid and vapor flows and it is listed on the next table:

Liquid	Vapor	C
turbulent	turbulent	20
laminar	turbulent	12
turbulent	laminar	10
laminar	laminar	5

Chisholm multiplier

Chisholm [18] proposed a correlation suited for cases where $\mu_l\mu_v > 1000$ and $G > 100\ kg/m^2/s$. The parameter he used was:

$$Y = \left[\frac{\left(\frac{dp}{dz}\right)_{lo}}{\left(\frac{dp}{dz}\right)_{vo}}\right]^{1/2} \tag{1.59}$$

$$\Phi_{lo}^2 = 1 + \left(Y^2 - 1\right)\left[Bx^{(2-n)/2}\left(1-x\right)^{(2-n)/2} + x^{2-n}\right] \tag{1.60}$$

where n is the exponent of the Reynolds number in the expression of the friction factor, meaning, that $n = 1$ for laminar flow and $n = 1/4$ for turbulent flow, and B is a parameter given by:

$$B = \begin{cases} \dfrac{55}{\sqrt{G}} & \text{if } 0 < Y < 9.5 \\ \dfrac{520}{Y\sqrt{G}} & \text{if } 9.5 < Y < 28 \\ \dfrac{15000}{Y^2\sqrt{G}} & \text{if } Y > 28 \end{cases} \tag{1.61}$$

Awad and Muzychka for microgravity

For microgravity experiments, an improvement of the two-phase multiplier model has been proposed by Awad and Muzychka [6] and is also in very good agreement with experimental data obtained by different authors in microgravity conditions, Fig. 1.12:

$$\phi_L^2 = \left[1 + \left(\frac{1}{X^2}\right)^{2/7}\right]^{7/2} \tag{1.62}$$

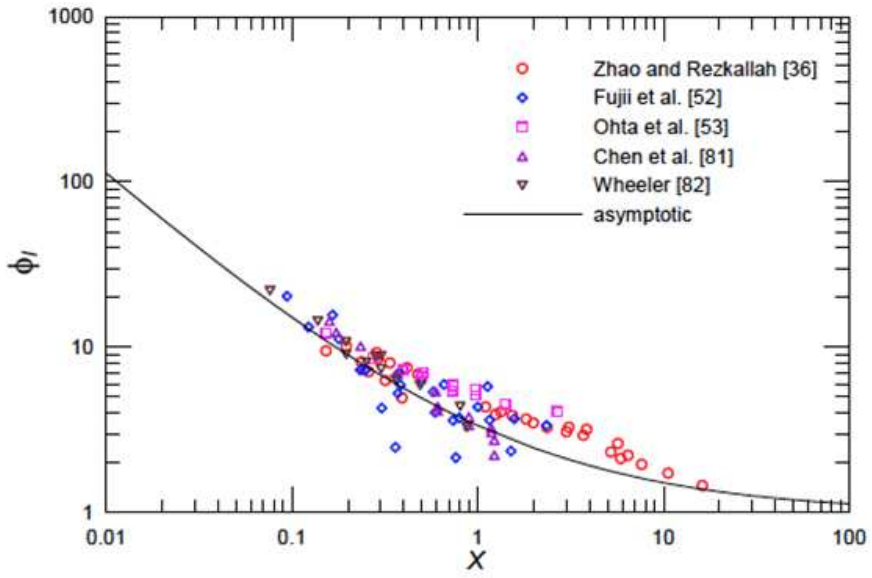

Figure 1.12: Pressure losses in microgravity conditions.

1.5.3 Interfacial shear stress in annular flows

To determine the interfacial shear stress, several closure laws exist in the literature for the prediction of the interfacial friction factor f_i:

$$f_i = \frac{\tau_i}{0.5\rho_v(U_v - U_l)^2} \simeq \frac{\tau_i}{0.5\rho_v U_v^2} \tag{1.63}$$

For annular wavy liquid films in large ducts (around 50 mm), Wallis [80] proposed an expression of the interfacial friction factor linked to the roughness of the liquid film that is assumed to equal the film thickness:

$$\frac{f_i}{f_v} = 1 + 300\frac{\delta}{D} \tag{1.64}$$

where f_v is the wall friction factor of a vapor flow on the smooth wall:

$$f_v = 0.079 Re_v^{-1/4} \quad with \quad Re_v = \frac{U_v D}{\nu_v} \tag{1.65}$$

Very few measurements of the interfacial shear stress have been performed in millimetric diameter tubes and even less measurements exist in microgravity conditions. A data set

is reported in 12.7 mm diameter tube in microgravity by Bousman and Dukler [10], who provided a correlation for the prediction of f_i/f_v:

$$\frac{f_i}{f_v} = 211.4 - 245.9\alpha \tag{1.66}$$

1.6 Modeling heat transfer coefficient

Applications like cooling systems and nuclear reactors have been an important subject and a real motivation for the development of models to understand liquid-vapor flows and to predict the heat transfer coefficient. There are different correlations to predict heat transfer. Here are some classical ones like Chen [15] taking into account the contribution of nucleate boiling and convective boiling and some others that are developed to predict heat transfer in the case of an evaporating liquid film in annular flow as Cioncolini and Thome [19].

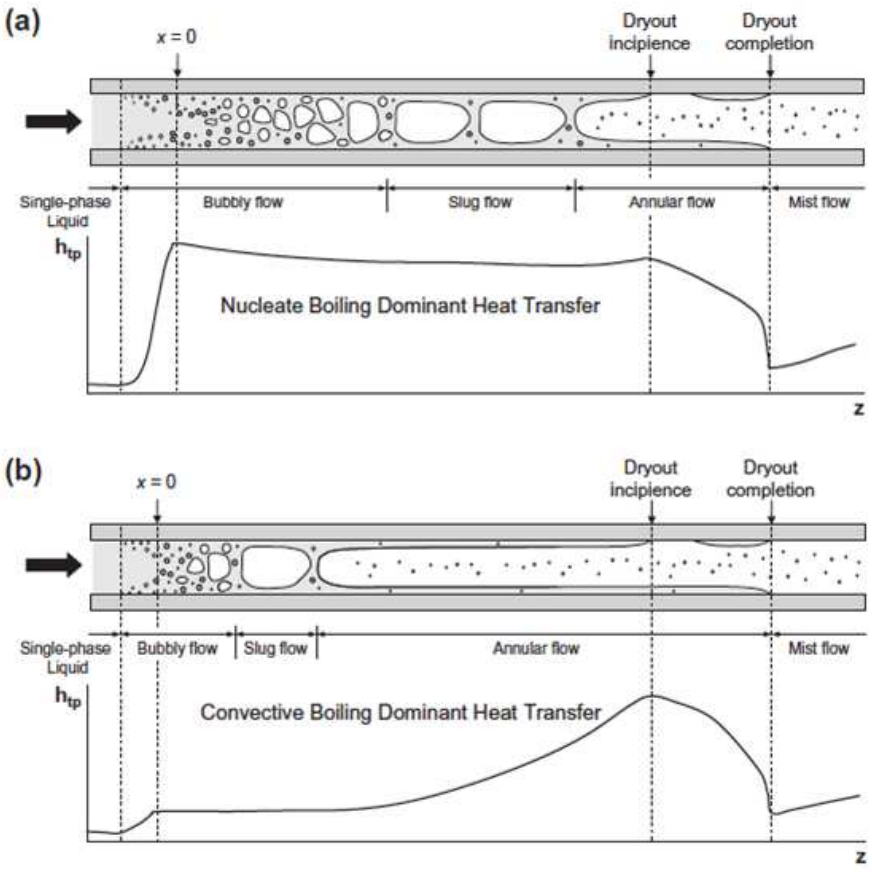

Figure 1.13: Contribution of nucleate boiling and convective boiling [50].

Two regimes, as shown in Fig. 1.13, have been identified based on the boiling mechanisms. When a regime is nucleate boiling dominant, a significant fraction of the channel is dominated by bubbly or slug flow and the heat transfer coefficient decreases monotonically due to gradual suppression of nucleate boiling. When the regime is the convective boiling dominant, it means that the heat transfer coefficient increases along the channel due to the thinning of the annular liquid film.

1.6.1 Chen's correlation

The correlation proposed by Chen [15] includes the interaction of nucleate and convective boiling.

The heat transfer coefficient h is written:

$$h = S \cdot h_{nb} + F \cdot h_l \tag{1.67}$$

where h_{nb} is the contribution of nucleate boiling and h_l is the contribution of the convection, F in an enhancement factor that increases the importance of convective boiling due to the presence of vapor depending on the Martinelli parameter. When $1/X > 0.1$

$$F(X) = 2.35 \cdot \left(0.213 + \frac{1}{X}\right)^{0.736} \tag{1.68}$$

else, $F(x) = 1$ and $S(X)$ is a suppression factor given by:

$$S(X) = \frac{1}{1 + 2.35 \cdot 10^{-6} \left(\frac{GD(1-x)F(X)^{1.25}}{\mu_l}\right)^{1.17}} \tag{1.69}$$

where h_{nb} is obtained from the Forster and Zuber [33] correlation for nucleate pool boiling:

$$h_{nb} = 0.00122 \cdot \left[\frac{\lambda_l^{0.79} C p_l^{0.45} \rho_l^{0.49}}{\sigma^{0.5} \mu_l^{0.29} h_{l,v}^{0.24} \rho_g^{0.24}}\right] (T_w - T_{sat})^{0.24} (p - p_{sat})^{0.75} \tag{1.70}$$

and h_l is expressed using the classical Dittus-Boelter correlation for turbulent flow for $Re_l > 2000$:

$$h_l = \frac{\lambda}{D} \cdot 0.023 \cdot Re^{0.8} Pr_l^{0.4} \tag{1.71}$$

The Chen correlation is more adapted to water flow, where the Prandtl number is large.

1.6.2 Kandlikar's correlation

A correlation was proposed and developed by Kandlikar [47], as a general correlation for saturated two-phase flow boiling heat transfer inside horizontal and vertical tubes for a

wide range of fluids and tube diameters. Heat transfer coefficient is considered to be the larger value between the nucleate boiling term and the convective term. Unlike the Chen correlation, it uses the boiling number, Bo defined by:

$$Bo = \frac{q_w}{Gh_{l,v}} \tag{1.72}$$

to determine the nucleate boiling contribution.

$$h = h_l \left[C_1 C_0^{C_2} + C_3 Bo^{C_4} F_K\right] \tag{1.73}$$

where h_l is calculated with usual turbulent single-phase flow correlations with the velocity j_l. F_K is a constant that can be adapted to suit the working fluid (for refrigerants, $F_K \simeq 1.2 - 1.4$. C_0 is a convection number used to determine the main contribution term. C_1 to C_4, given in Table. 1.1

	$C_0 > 0.65$	$C_0 < 0.65$
C_1	0.6683	1.1360
C_2	-0.2	-0.9
C_3	1058.0	667.2
C_4	0.7	0.7

Table 1.1: Values for constants in Kandlikar's correlation

1.6.3 Liu and Winterton

Liu and Winterton [56] observed that other empirical correlations that had used a boiling number, for correction purposes, had the idea of allowing the enhancement of the forced convective heat transfer mechanism arising from the generation of vapor in the boundary layer next to the wall. However the boiling number prevents application to subcooled boiling. They proposed a correlation depending on the Prandtl number that has an explicit nucleate boiling term and no boiling number dependence.

The method of combining the two contributions suggested by Kutateladze [53] was used by Liu and Winterton [56] where:

$$h_{tp}^2 = (Fh_l)^2 + (Sh_{pool})^2 \tag{1.74}$$

In this equation h_l is Dittus-Boelter Eq. 1.71 and F is the enhancement factor given by:

$$F = \left[1 + xPr_l \left(\frac{\rho_l}{\rho_v} - 1\right)\right]^{0.35} \tag{1.75}$$

the Fh_l is the contribution of the forced convection mechanism, whereas, S is the suppression factor:

$$S = \left(1 + 0.055F^{0.1}Re_L^{0.16}\right)^{-1} \tag{1.76}$$

and h_{pool} is calculated from Cooper's [26] pool boiling correlation:

$$h_{pool} = 55p_r^{0.12}q^{2/3}\left(-log_{10}Pr\right)^{-0.55}M^{-0.5} \tag{1.77}$$

where M is the molecular weight, p_r the reduced pressure, and h_{pool} gives the contribution of the nucleate boiling mechanism.

1.6.4 Kim and Mudawar's correlation

As written by Kim and Mudawar [50], after reviewing the literature, it is imperative to evaluate the large body of models for flow boiling in small channels and create a universal model. It is important to have, as they propose on the second part of their study a universal tool that can be used to model and predict heat transfer applicable to a broad range of operating conditions. The development of a predictive tool is presented for saturated flow boiling in mini and microchannels. With the widely discussed two mechanisms identified that can dominate the largest fraction of the channel, bubbly and slug flow are mainly present in the channel whereas a significant part of the channel length is dominated by annular flow when convective boiling heat transfer is dominant.

Authors	D	Fluid	G $[kg/m^2s]$	Heat transfer
Wang et al. [81]	$6.5mm$	R22	100-400	$h_{tp} = f(q", G, x)$, $NB + CB$
Yun et al. [85]	$6mm$	R134a, CO_2	170-340	$h_{tp} = f(q", G, x)$, NB
Zhao and Bansai [88]	$4.57mm$	CO_2	140-231	$h_{tp} = f(q", G, x)$
Greco [38]	$6.0mm$	R22	100-400	$h_{tp} = f(q", G, x)$, $NB + CB$
Mastrullo et al. [58]	$6.0mm$	CO_2	200-349	$h_{tp} = f(q", x)$, NB
Oh and Son [65]	$5.35mm$	R134a, R22	200-500	$h_{tp} = f(q", G, x)$, CB

Table 1.2: Saturated flow boiling database

Table 1.2, shows some of the work reviewed by Kim and Mudawar with parameters close to

those of our experiment BRASIL. Since the influence of the tube diameter is very important and in this table we present the closest studies that are comparable to our work. To be able to propose a universal approach, a database, with 18 working fluids, hydraulic diameters of $0.19 - 6.5mm$, mass velocities of $19 - 1608kg/m^2/s$, liquid- only Reynolds numbers of 57-49,829, qualities of 0-1 and reduced pressures of $0.005 - 0.69$, was examined.

On Kim and Mudawar's [50] review, thirteen correlations are presented with each specific fluid and specific operating range conditions. Finally, Kim and Mudawar, present a universal correlation that takes into account the contribution of the nucleate boiling and the convective boiling mechanism.

New correlation	$h_{tp} = (h_{nb}^2 + h_{nb}^2)^{0.5}$ $h_{nb} = \left[2345 \left(Bo\frac{P_H}{P_F}\right)^{0.7} P_R^{0.38} (1-x)^{-0.51}\right] \left(0.023 Re_f^{0.8} Pr_f^{0.4} \frac{k_f}{D_h}\right)$ $h_{cb} = \left[5.2 \left(Bo\frac{P_H}{P_F}\right)^{0.08} We_{fo}^{-0.54} + 3.5 \left(\frac{1}{X_{tt}}\right)^{0.94} \left(\frac{\rho_v}{\rho_f}^{0.25}\right)\right] \left(0.023 Re_f^{0.8} Pr_f^{0.4} \frac{k_f}{D_h}\right)$ where $Bo = \frac{q"_H}{Gh_{fg}}$, $P_R = \frac{P}{P_{crit}}$, $Re = \frac{G(1-x)D_h}{\mu_f}$, $We_{fo} = \frac{G^2 D_h}{\rho_f \sigma}$, $X_{tt} = \left(\frac{\mu_f}{\mu_v}\right)^{0.1} \left(\frac{1-x}{x}\right)^{0.9} \left(\frac{\rho_v}{\rho_f}\right)^{0.5}$, $q"_H$: effective heat flux average over heated perimeter of channel, P_H : heated perimeter of channel, P_F : wetted perimeter of channel.

1.6.5 Heat transfer in annular flows: Cioncolini and Thome's Model

The model proposed by Cioncolini and Thome [19] provides an estimation of the heat transfer that occurs by the evaporation through the turbulent liquid film in an annular flow according to the liquid film thickness and the wall shear stress. It is represented by Eq. 1.78 and this correlation is based on eddy viscosity and heat diffusivity models that provides both velocity and temperature profiles through the liquid film and can be used to predict In this model the film thickness is calculated from Eq. 1.42 to 1.45 the heat transfer due to evaporation.

The key assumption pointed out by the authors is that the flow in a shear-driven annular liquid film is mostly affected by the interaction of the film with the shearing gas-entrained droplet core flow. That is to say the liquid film is assumed to behave as a fluid-bounded flow, such as a jet or a wake, with a negligible influence of the bounding channel wall.

Heat transfer coefficient according to the liquid film thickness and the wall shear stress is obtained by:

$$h = \frac{\lambda_l}{\delta} 0.0776 (\delta^+)^{0.9} Pr^{0.52} \tag{1.78}$$

Where h is the convective boiling heat transfer coefficient and,

$$\delta^+ = \frac{\delta}{y^*} = \frac{\delta u^*}{\nu_l} \tag{1.79}$$

$$\text{for } 10 < \delta^+ < 800 \text{ and } 0.86 < Pr < 6.1$$

Where δ^+ is the dimensionless average liquid film thickness, u^* is the friction velocity

$$u^* = \sqrt{\frac{\tau_w}{\rho_l}} \tag{1.80}$$

and y^* is a viscous scale.

As explain by Cioncolini and Thome [19] δ^+ can be interpreted as a Reynolds number for the liquid film with the friction velocity, u^* as the characteristic velocity and the average liquid film thickness δ as characteristic dimension. It is important to say that the model assumes there is no nucleate boiling occurring in the annular liquid film.

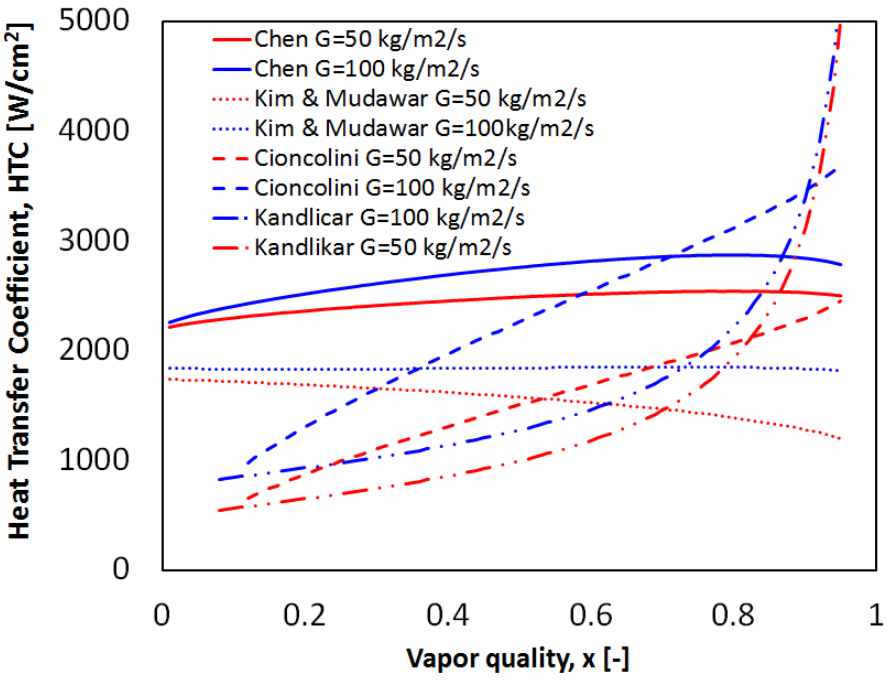

Figure 1.14: Correlations that predict HTC

In Fig. 1.14, the different correlations give HTC versus the vapor quality x are plotted for 2 mass fluxes for the refrigerant HFE7000. This illustrates the significant differences that may exist between the different correlations.

1.7 Heat Transfer Coefficient in microgravity

Flow boiling experiments are very limited for microgravity conditions. the most recent experiments have been performed by Ohta [66], Ohta and Baba [67], Baltis et al. [8], Celata and Zummo [12], Narcy et al. [61], and Lebon et al. [54] were used to compared the results obtained during this study.

Experiments performed by Ohta

Ohta [66] performed microgravity experiments on board the MU-300 japanese aircraft for upward flow boilind experiments with R113. The test section had a 8mm inner diameter glass tube coated with a thin gold film. Flow pattern visualization are simultaneously possible, void fraction measurements are taken and heat transfer data are analyzed for different heat fluxes. More recently, Ohta and Baba [67] presented results for heat transfer coefficients for a flow of FC-72 in a 4 mm inner diameter tube.

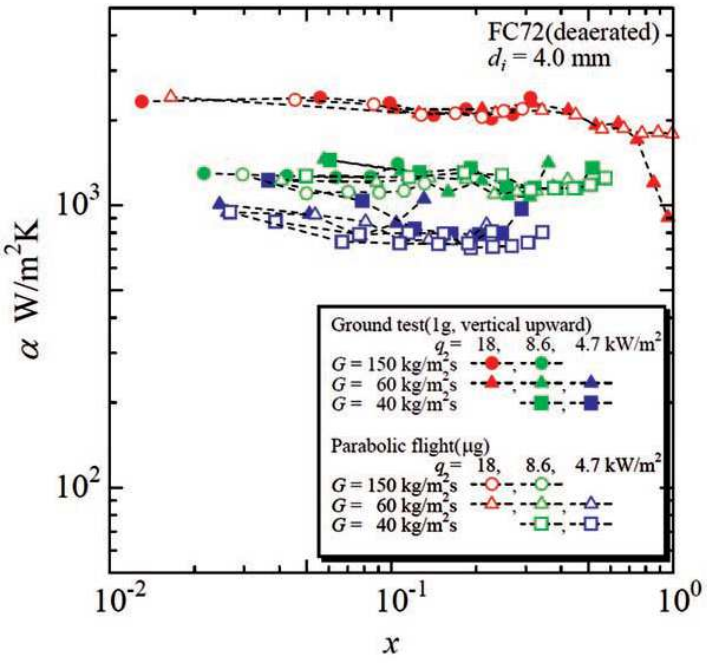

Figure 1.15: Data from experiments of Ohta and Baba [67].

Ohta and Baba [67] reported measurements for mass fluxes from $G = 40$, $G = 60$ and $G = 150$ $kg/m^2/s$ and heat up to 1.8 W/cm^2. For this range of mass fluxes, nucleate boiling always occurs in annular flows (NBA) and as seen in Fig. 1.15 the heat transfer coefficient is independent of the vapor quality up to the critical heat flux and no eventual effect of the gravity is seen.

Experiments performed by Baltis et al.

Baltis et al. [8] compared and reported experimental results on heat transfer coefficient for subcooled FC-72 flow boiling under microgravity conditions for tubes of 2, 4 and 6 mm of inner diameter.

They explained that the difference in bubble dimension between the two gravity levels, at low mass fluxes and low heat fluxes, which can be associated with an increase in the turbulence level and eventually increase the heat transfer rate. In Fig. 1.16, they plotted for the 6 mm diameter tube the ratio of the HTC measured in 0g and in 1g. It can be seen that in the subcooled nucleated boiling regime for thermodynamics qualities lower than zero, HTC is significantly smaller in microgravity.

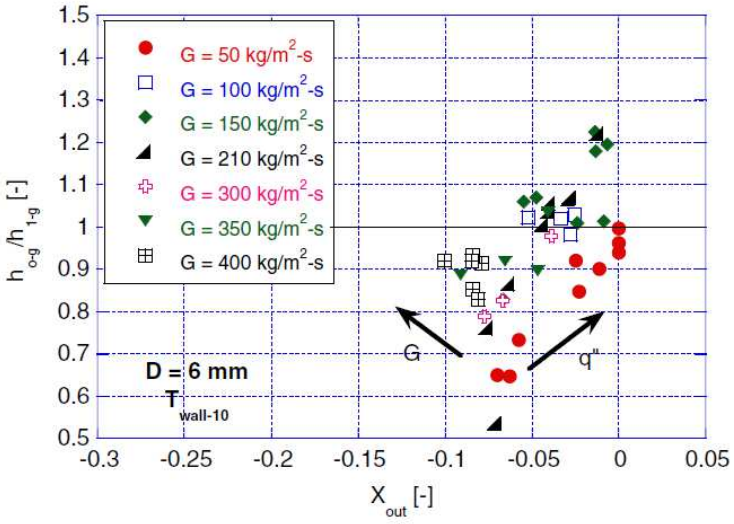

Figure 1.16: Influence of gravity on HTC versus vapor quality by Baltis et al. [8]

The authors also plotted Fig. 1.17 a (G, x) map where the influence of gravity on HTC is highlighted. It is confirmed that gravity has an effect on HTC for highly subcooled flow and for saturated flow at qualities lower than 0.2 and mass fluxes lower than $100 kg/m^2/s$.

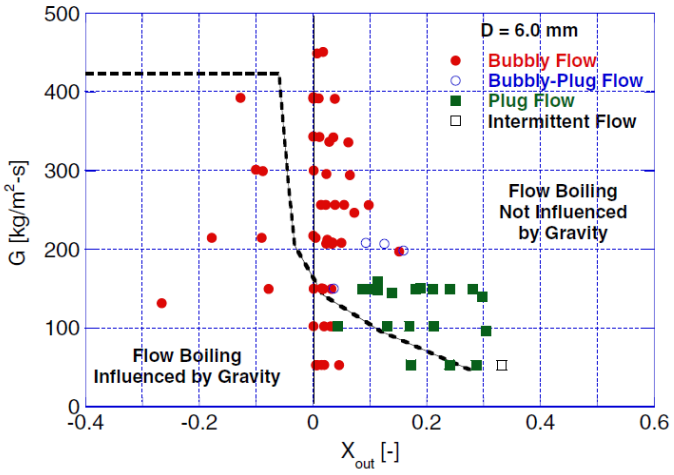

Figure 1.17: Flow boiling gravity influence map for a 6 mm tube

Experiments performed by Narcy et al.

Narcy et al. [61], performed experiments on flow boiling in a vertical tube on ground and microgravity conditions in a 6 mm diameter tube with HFE7000. Fig. 1.18 shows the results obtained for a 2 heat fluxes at $G = 200kg/m^2/s$.

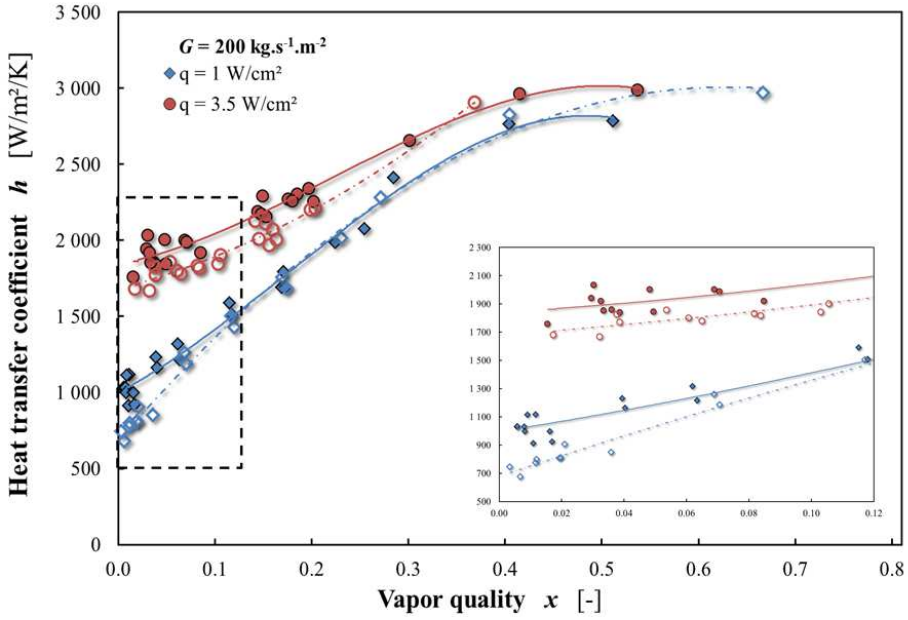

Figure 1.18: Comparison of HTC values for microgravity and normal gravity

In soobcooled conditions, heat transfer coefficient was affected and significantly lower in microgravity than in normal gravity. At high quality, in saturated regimes the difference was less obvious. The curves tend to a similar values in normal and microgravity for high quality and for high heat flux.

Experiments performed by Lebon et al.

Recently Lebon et al. [54] studied subcooled flow boiling with HFE7000 in a vertical 6 mm ID sapphire tube in upward and downward flow at various gravity levels including hypergravity and microgravity. They used Temperature sensitive paint (TSP) applied to the inside of the tube to measure time and space resolved temperature and heat transfer distributions. Thanks to the transparency of the TSP layer, flow visualization were used to characterize the heat transfer for different flow patterns. In Fig. 1.19, the heat transfer coefficient is plotted versus gravity for different heat flux and mass fluxes and for a subcooling of the liquid of $10°C$ at the tube entrance. The lower values of the HTC in microgravity are clearly visible at low mass flux and low heat flux.

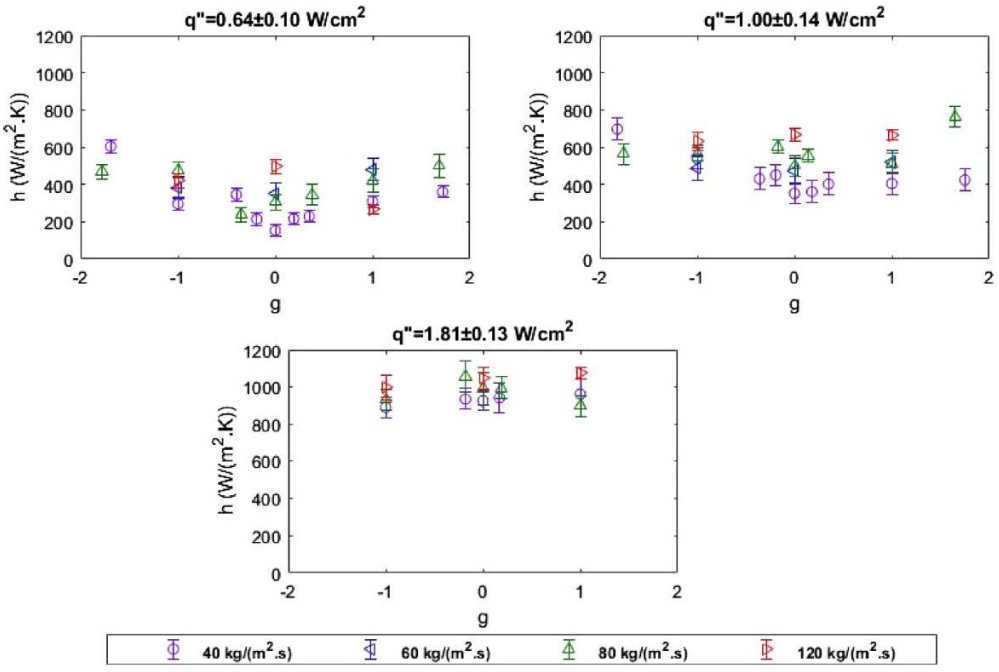

Figure 1.19: HTC versus gravity level and heat flux for soobcooled flow boiling

The authors summarized their results in Fig. 1.20, plotting in a (G,q) map the regions influenced by gravity. The effect of gravity is obvious for low heat fluxes and mass fluxes smaller that $100kg/m^2/s$. This map cannot be directly compared to those of Baltis et al. [8], but it is expected that experiments performed at low heat fluxes correspond to lower

qualities values. It should have been interested to plot also these graphs versus quality.

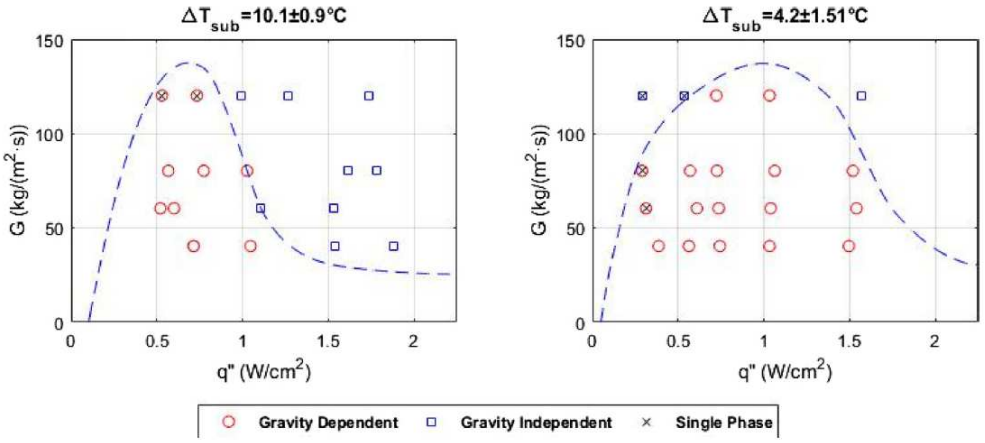

Figure 1.20: Gravity dependence regime maps

1.8 Conclusion

In this chapter, we presented some models and correlations for the prediction of the flow pattern transition, the void fraction, wall fraction and heat transfer coefficient. The literature on two-phase flows and flow boiling is very wide, therefore this study is far from being exhaustive. Since the main models presented in this chapter will be used for comparison with the experimental results presented on Chapter 3, we focused on a limited range of parameters (tube diameter, fluid properties, flow rates).

The study of flow boiling in microgravity were mainly focused on the determination of the heat transfer coefficient. They all point out the effect of gravity in subcooled nucleate boiling at mass fluxes lower than $100 kg/m^2/s$.

Chapter 2

Experimental Setup and Measurement Techniques

This chapter presents a description of the experimental apparatus used for flow boiling study. Then, measurement techniques for pressure and temperature are described. The local quality in the test section is calculated from a thermal balance after evaluation of the heat losses. The void fraction is measured by capacitance probes. Two different techniques, based on Pt100 probes or infrared thermography are developed for heat transfer coefficient measurements. Uncertainties are evaluated all along the chapter.

2.1 Experimental Setup

To study flow boiling dynamics and heat transfer in normal and microgravity conditions, an experimental setup, called BRASIL (Boiling Regimes in Annular and Slug flow In Low gravity), was built at IMFT. This setup provides several measurements of temperature, pressure (differential or absolute), void fraction and heating power. Thanks to these measurements it is possible to determine the local quality in the test section, the superficial liquid and gas velocities, j_l and j_v, the mean velocities of the liquid and gas, U_l and U_v, the wall and interfacial shear stresses, τ_w and τ_i and the heat transfer coefficient HTC.

During the present study two test sections were implemented for the measurements of the heat transfer coefficient (HTC). These test sections have already been used by Narcy et al. [61] or Kim et al. [49]. The last one was implemented in BRASIL during the present work.

The experiment is formed of two main parts, see Fig. 2.1, a closed one including the hydraulic loop with the sensors. The other part is an open side, with all the acquisition and conditioning system, used to control the hydraulic system.

The data are acquired with a National Instrument Data Acquisition System (NI DAQ), which allows the simultaneous acquisition of over 70 signals. The interface of the NI DAQ is a LabVIEW program designed to display the sensors' measurements live and to save the data using a text-based file format for further processing. Surveillance of all temperatures

or pressures is done from this interface. Alarms are triggered if any of the values are over the limit to avoid any malfunction of the system. This allows the experiment to comply safety issues demanded to perform measurements in microgravity conditions. The two-phase flow loop and the measurement techniques will be described in the following sections.

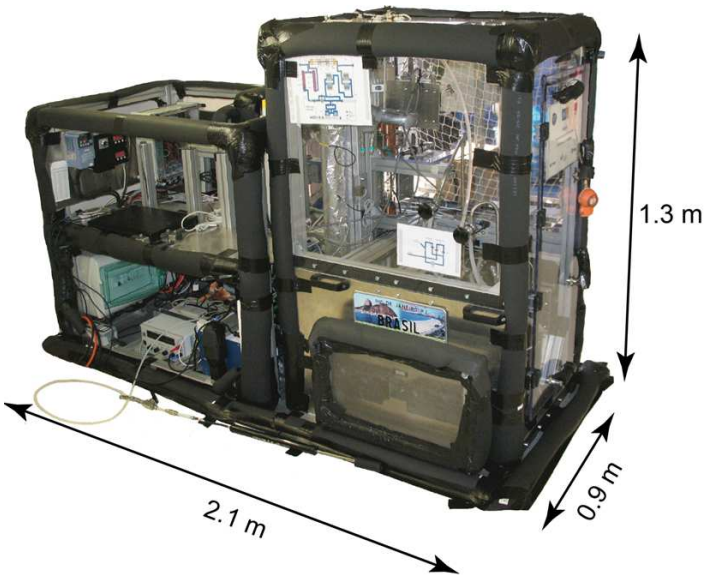

Figure 2.1: Experimental Apparatus, the hydraulic loop is on the right part while the left part contains the acquisition and conditioning system.

2.1.1 Hydraulic circuit

The hydraulic circuit has a classical configuration, where a liquid refrigerant is pumped, then heated and partially vaporized in the preheaters, then further vaporized in the test section and finally condensed and cooled with Peltier modules before reentering the pump (see Fig. 2.2).

A gear pump (L21755 Micropump with a DC-305 A motor) driven by magnetic force is used to circulate the fluid in the loop. It is capable of pumping liquids with temperatures ranging from $-46°C$ to $121°C$. The liquid flow rate is adjusted by changing the rotating speed of the pump, which is controlled by a 12 VDC power supply. The maximum flow rate of the pump is 3.2 L/min at a maximal system working pressure of 21 bar.

The flow meter, placed after the pump, uses a practical application of the Coriolis effect to measure the flow rate, $\dot{m}$, with an accuracy of 0.5% of the measured value.

The preheaters of the liquid loop consist of two stainless steel 85 cm long tubes with a helical resistive wire placed inside it with a heating power ranging from 0 to 900 W. A power supply QVR 320 with a variable regulator is used. The voltage is set with an accuracy of ± 45 mV and the current with an accuracy of ± 30 mA. The two resistive wires

are electrically connected in a serial configuration with one power supply: a variable phase angle power regulator which is directly connected to the power supply of the experiment and manually regulated. Inside each heater, thermocouples measure the temperature of the resistive wire at different positions ($TexH1, T3H1$), and the liquid temperature inside the heaters ($TLH1, TLH2$). These thermocouples are used for safety issue in order to detect any overheating. The liquid is heated in the preheaters and can also be vaporized.

Two test sections are used in the experimental apparatus, corresponding each one to Fig. 2.2, for a sapphire tube, and Fig. 2.3 for a silicon tube. The inner tube diameter is 6 $mm \pm 0.05$ mm. The two different diagrams present also the different sensors that correspond to each configuration. The liquid enters the section sections where it is further vaporized by the heat power input at the tube. Each test section will be entirely described later on this chapter.

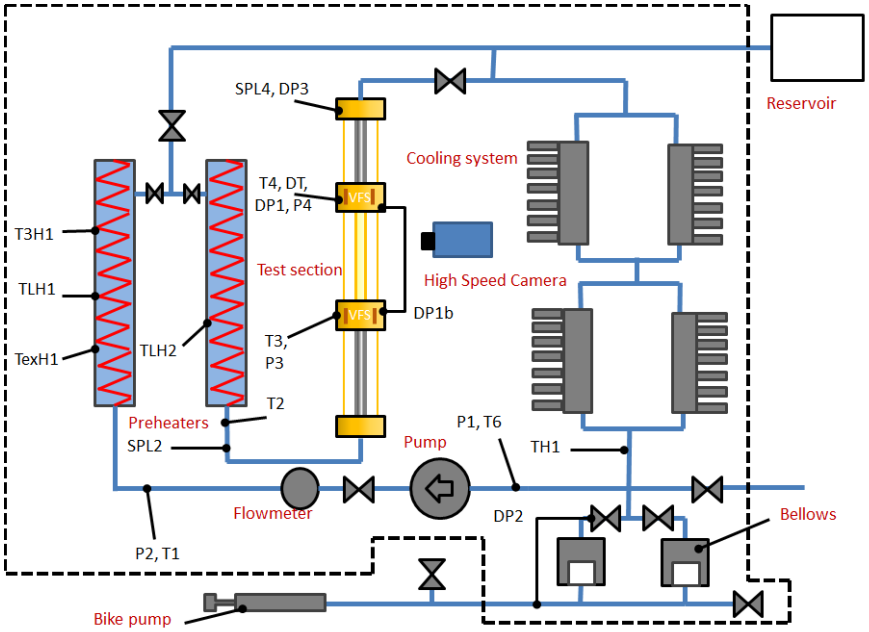

Figure 2.2: Hydraulic loop and sensors placed in the experiment for the Sapphire tube configuration.

After the test section, condensation and cooling of the fluid below its saturation temperature is needed to ensure that vapor will never enter the pump to avoid pump malfunction. The experiment is equipped with a cooling system of Peltier elements for this purpose, which are a high performance heat exchangers because of their internal geometry. The flow circulates in a cold plate and thanks to the Peltier elements heat is evacuated by heat sinks, which are cooled by fans. The power input at the fans is constant, however, the power applied to the Peltier modules is automatically regulated by two temperature controllers. Therefore the temperature at the inlet of the pump, T_6, is kept at a constant value of $T_{sat} - 10$ °C, T_{sat} being the saturation temperature. At the end of the circuit it is important to compensate

the volume variations of the liquid resulting from vaporization and dilatation. This pressure is compensated by two bellows, where one room is connected to the liquid circuit and the other to air. This allows to compensate the volume variations and change the pressure if necessary with the use of a manual bike pump.

In normal conditions the working mass fluxes, G, range from 50 to 400 $kg/m^2/s$, pressure values from 1 to 1.3 bar and vapor qualities, x, at the inlet of the test section go up to 0.8.

To calculate G and the accuracy on the mass flux:

$$G = \frac{4\dot{m}}{\pi D^2} \tag{2.1}$$

$$\frac{\Delta G}{G} = \sqrt{\left(\frac{\Delta \dot{m}}{\dot{m}}\right)^2 + \left(\frac{2\Delta D}{D}\right)^2} = \sqrt{(0.005)^2 + \left(\frac{0.1}{6}\right)^2} \simeq 1.7\% \tag{2.2}$$

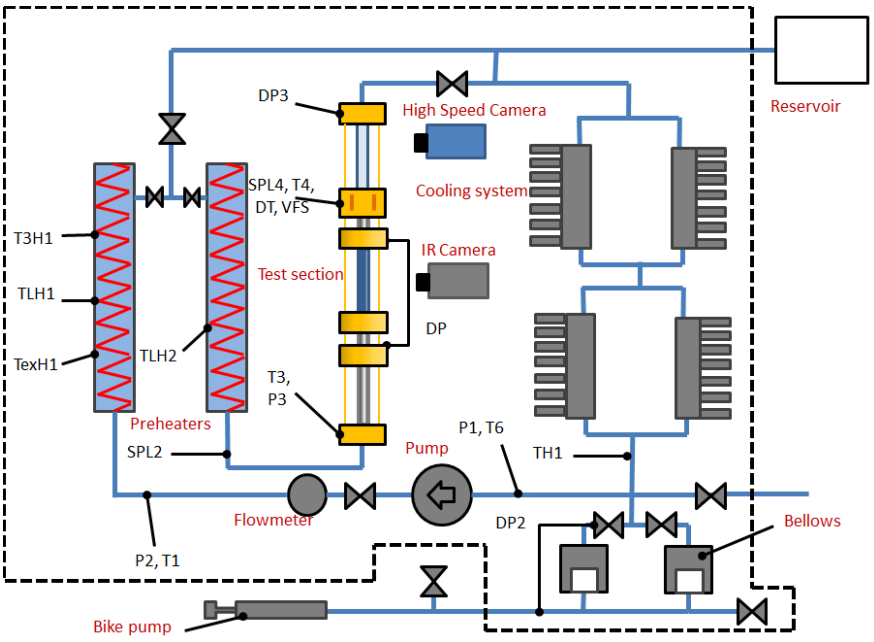

Figure 2.3: Hydraulic loop and sensors placed in the experiment for the Silicon tube configuration.

2.1.2 Working Fluids

The working fluid, circulating in the hydraulic system for the sapphire tube configuration, is a refrigerant called HFE-7000 (1-methyoxylheptafluoropropane $C_3F_7OCH_3$). In this case, this fluid was chosen for its low latent heat of vaporization and the low saturation temperature at atmospheric pressure (34°C).

For the silicon tube, HFE-7000 was not chosen since the difference between the ambient temperature and the saturation temperature is too low for accurate measurements by infrared thermography. This small temperature difference will result in low accuracy in temperature measurements and thus in large errors in the heat transfer coefficient. For the case of the silicon tube, HFE-7100 was used since the saturation temperature is higher (61°C at atmospheric pressure) and the IR technique used improves in accuracy.

	HFE-7000	**HFE-7100**
Molecular Weight (g/mol)	200	250
Boiling Point @ 1 atm (°C)	34	61
Freeze Point (°C)	-122.5	-135
Liquid Density (kgm^{-3})	1376	1421
Vapor Density (kgm^{-3})	7.98	9.40
Kinematic Viscosity (m^2s^{-1})	2.71×10^{-7}	3.06×10^{-7}
Liquid Specific Heat ($kJKg^{-1}K^{-1}$)	1328	1250.8
Latent Heat of Vaporization (Jkg^{-1})	132.2	112.1
Surface Tension (nNm^{-1})	11.23	10.06

Table 2.1: Main properties of 3M^{TM} Novec^{TM} HFE-7000 and HFE-7100 Engineered Fluids at saturation temperature and at atmospheric pressure [69].

These segregated hydrofluoroethers (HFE) products offer some very important properties for the application in BRASIL: low toxicity, non-flammability and good materials compatibility, which complies with all the restrictions established for parabolic flight experiments. Moreover it is an excellent dielectric; a potential leakage will not damage the electronic equipment of the test set-up. Table 2.1 summarizes the main properties of both fluids and their differences.

2.1.3 Test section with Sapphire Tube

BRASIL's experimental core is the test section. The first configuration used consisted of three parts, two adiabatic sections, one at the inlet and one at the outlet, and one sapphire tube between these two adiabatic sections. Two Void Fraction Sensors (VFS) are also placed, one at the exit of the first adiabatic section and the second one at the exit of the sapphire tube as shown in Fig. 2.4. This test section was already used by Narcy [64], but the sapphire tube with the ITO deposit and the void fraction sensors were changed to improve the measurement accuracy.

The sapphire tube is 200 mm long with a heated length of 170 mm and has a 50 nm thick ITO (Indium Tin Oxide) coating, which is an electrical conductive coating that allows heating on the external wall of the tube by Joule effect. A power supply EA-PS 3150-04B is used. It delivers a voltage up to 120 V with an accuracy of ± 30 mV and a current up to

1 A with an accuracy of ± 10 mA. This coating does not greatly affect the transparency of the sapphire tube; thus, the flow can be filmed during tests with a high-speed video camera for the purpose of flow visualization which enables the flow pattern identification.

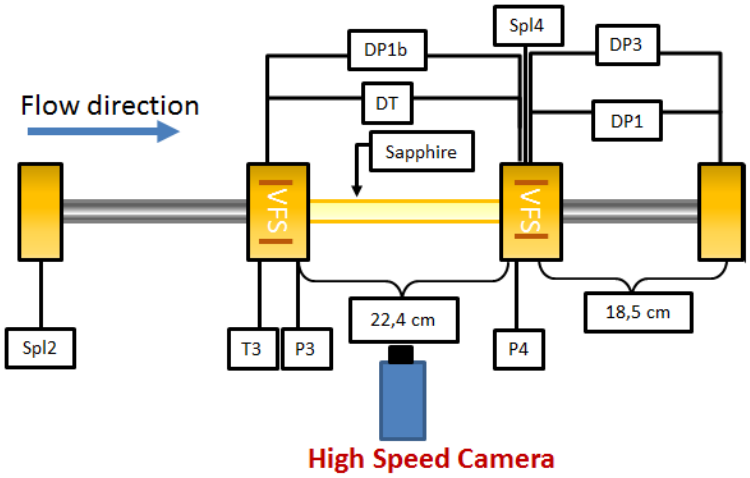

Figure 2.4: Detailed test section for the Sapphire tube configuration.

The two adiabatic parts are made of a stainless steel tube with an inner diameter of 6 mm and an outer diameter of 8 mm, it's lengths are 22 and 15 cm, respectively. To achieve the adiabatic conditions, the tubes are covered with thermal insulation. The length of the first tube is adapted so that the flow can be fully developed. The second adiabatic section is long enough to measure the pressure drop along it.

Pressure sensors and temperature sensors were also placed upstream and downstream of the test section to perform heat balance.

2.1.4 Test section with Silicon Tube

The second configuration has as main parts also two adiabatic sections and one heated section. The heated section is a 10 cm long silicon tube placed between the two adiabatic parts. One to allow a fully developed flow to establish, reducing the entrance effects, and the other one to measure the pressure drop. In this case the second tube is a glass tube, since the silicon tube is opaque the glass tube will allow the flow visualization and the recognition of flow patterns.

Since the Silicon tube had to be adapted to BRASIL, there are two small isolated stainless steel tubes that connect the adiabatic parts with the main silicon tube as shown in the schematics of Fig. 2.5.

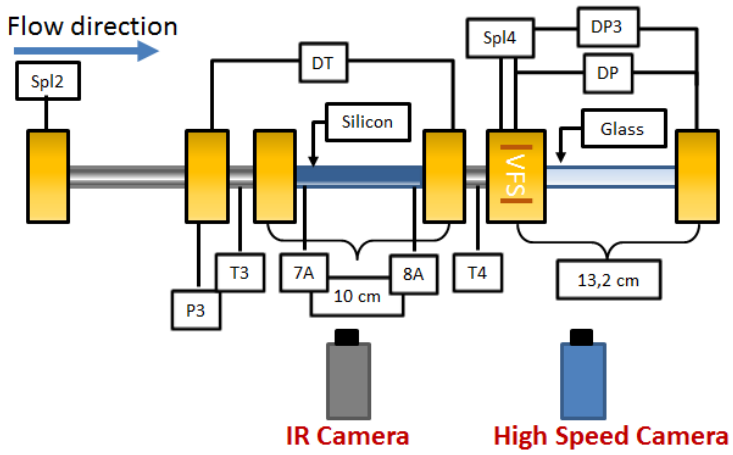

Figure 2.5: Detailed test section for the Silicon tube configuration.

2.2 Pressure and Temperature measurements

In this section the characteristics of the pressure and temperature sensors and their accuracy will be detailed.

2.2.1 Pressure sensors

Pressure transducers (Keller PAA21) measure the absolute pressure at different locations of the circuit, P_1, P_2, P_3, P_4 in Fig. 2.2 and Fig. 2.3. These pressure transducers have a full scale of 0-5 bar with an accuracy of $\pm 0.25\ mbar$. Sensors monitor the pressure in order to calculate the different saturation temperatures before the pump, at the preheaters and especially inlet and outlet of the test section.

Differential pressure transducers have also been used in the PhD of Narcy [64] to measure the pressure drop along the tube and the wall shear stress.

2.2.2 Temperature sensors

Temperature sensors used on the experiment are basically of 3 types: K-type thermocouples, T-types thermocouples and Pt100 probes.

Fluid temperature measurements for probes T_1, T_2, T_3, T_4, T_5, T_6, shown in Fig. 2.2 and in Fig. 2.3, are thermocouples type K. These are used to measure the temperature of the liquid in different points of the hydraulic loop. Thermocouple T_3 is used to measure the fluid temperature at the inlet of the test section after the first adiabatic part. These

thermocouples use a cold junction compensation of the NI DAQ. The accuracy given by the manufacturer is of ±0.25°C.

In subcooled boiling the temperature difference along the test section is low. To improve the accuracy of this temperature difference two thermocouples type T are used (DT, in Fig. 2.4 and Fig. 2.5) which measures a difference of temperature between the inlet and the outlet of the test section. These thermocouples are connected using one thermocouple as a hot junction and the other one as a cold junction, giving a precise difference in voltage even if the difference is really small. Precision of measurements is ±0.1°C.

Fluid temperature is also measured with Pt100 probes ($Spl2$, $Spl4$) with a precision of ±0.1°C, for absolute values of temperature. The outer wall temperature of the sapphire tube is measured in several locations by Pt100 probes (Fig. 2.14a). A previous calibration is done before introducing the thermocouples and the Pt100 probes in the test section.

The calibration requires the use of a thermal bath, where the thermocouples are placed and the temperature is varied between ambient temperature and 60°C. To have the precise measurement of the bath temperature a standard high-precision resistance device is used (Isotech). This type of instruments are calibrated professionally with a precision of ±0.05 °C.

Temperature measurement accuracy is important to measure the liquid enthalpy in subcooled boiling or the quality, x, in saturated boiling regimes.

2.3 Vapor quality

Vapor quality at the inlet of the test section, in saturated boiling regimes, is deduced from the enthalpy balance in the preheaters and the adiabatic part upstream the sapphire tube:

$$P_{pre} = \dot{m}\left[x_{in}h_v + (1 - x_{in})\, C_{pl}T_3 - C_{pl}T_1\right] \tag{2.3}$$

$$= \dot{m}\left[x_{in}\left[h_{lv} + C_{pl}\left(T_{sat} - T_3\right)\right] + C_{pl}\left(T_3 - T_1\right)\right] \tag{2.4}$$

where T_1 is the temperature at the entrance of the preheaters, T_3 the temperature at the inlet of the test section and P_{pre} is the power of the preheaters. The temperature of the liquid is equal to the saturation temperature, $T_3 = T_{sat}$, in saturated boiling, and the phase change starts in the preheaters.

$$x_{in} = \frac{\frac{P_{pre}}{\dot{m}} - C_{pl}(T_{sat} - T_1)}{h_{lv} + C_{pl}\left(T_{sat} - T_1\right)} - \tag{2.5}$$

Since the fluid is heated from an electrical resistance inside the preheaters protected with a high quality thermal insulation, heat losses along the preheater are neglected.

The uncertainty on x_{in}, neglecting errors on fluid physical properties, can be written as:

$$\Delta x_{in} = \sqrt{\left(\frac{\Delta P_{pre}}{\dot{m}[h_{lv}+C_p(T_{sat}-T_1)]}\right)^2 + \left(\frac{P_{pre}\Delta\dot{m}}{\dot{m}^2[h_{lv}+C_p(T_{sat}-T_1)]}\right)^2 + \left(\frac{C_p\Delta T_1}{[h_{lv}+C_p(T_{sat}-T_1)]}\right)^2} \quad (2.6)$$

The uncertainty, Δx_{in} is plotted in Fig. 2.6

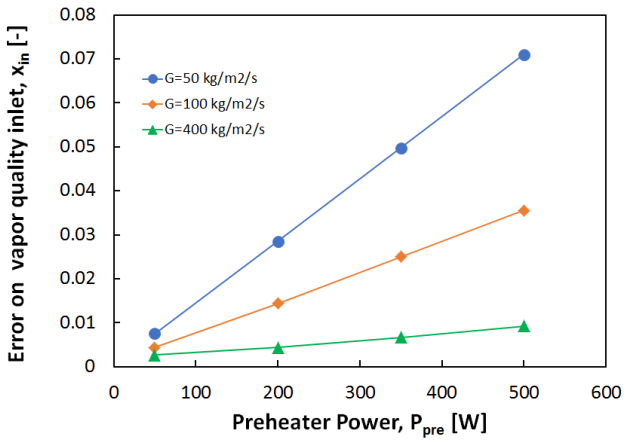

Figure 2.6: Error on x_{in} for different mass fluxes.

For low mass flux, $G = 50\ kg/m^2/s$, significant absolute error on the vapor quality is observed.

In saturated boiling, vapor quality $x(z)$, in the test section at any given axial position, z, in the tube is calculated with:

$$x(z) = x_{in} + \frac{4q}{GDh_{lv}}z \quad = \quad x_{in} + \frac{q\pi Dz}{\dot{m}h_{lv}}z \quad (2.7)$$

where q is the heat flux at the wall of the test section.

Since the heated test section, sapphire or silicon tube, is not insulated and it is connected to the peek or metallic parts, the heat loss estimation is required (Fig 2.7).

The heat losses around the test section are due to thermal convection and radiation and also due to conduction towards the peek or metallic supports at the inlet and outlet of the test section.

In order to estimate the total heat loss, the heating power P_{ITO} for the sapphire tube is compared in single-phase flow to the enthalpy variation of the liquid along the test section: $= G\pi\frac{D^2}{4}C_p\left(T_l\left(L\right) - T_l\left(0\right)\right)$ where $T_l\left(0\right)$ and $T_l\left(L\right)$ are the liquid temperature at the inlet

and outlet of the test section, respectively. $T_L(0)$ is measured by the thermocouple T_3 or the Pt100 probe $Spl2$, and $T_L(L)$ is measured by the Pt100 probe $Spl4$. The differential DT thermocouple is also used to measured $T_l(L) - T_l(0)$.

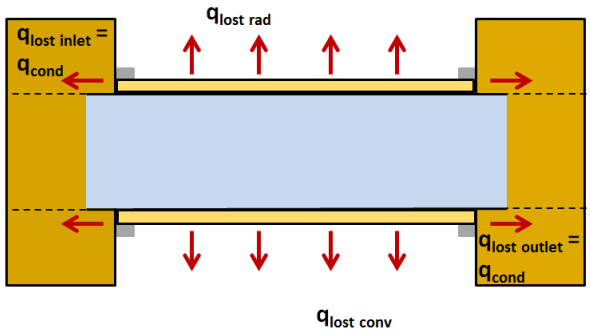

Figure 2.7: Thermal losses due to radiation, conduction and natural convection.

Fig. 2.8 presents a comparison of the heating power P_{ITO} and the enthalpy increase of the liquid. This comparison points out that the heat losses are close to 20% for the sapphire tube. As a consequence the heat flux transmitted to the liquid q is equal to:

$$q = \frac{P_{ITO}}{\pi DL}\eta \quad \text{with} \quad \eta \simeq 0.8 \tag{2.8}$$

where η is estimated from the plot in Fig. 2.8 with an uncertaintly of $\Delta\eta \simeq 0.2$.

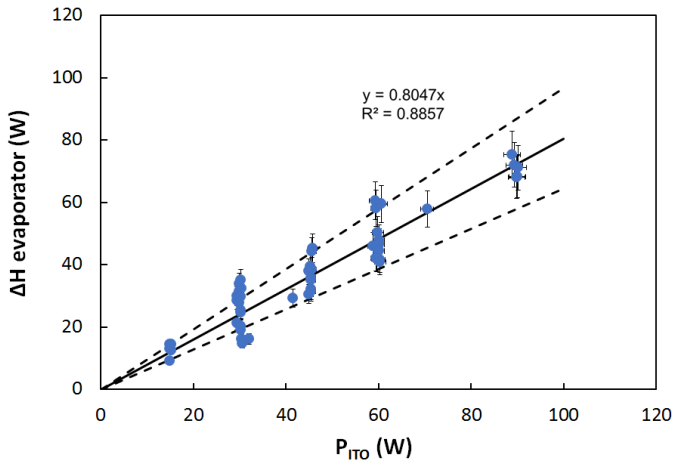

Figure 2.8: Thermal losses for the sapphire tube.

For the silicon tube, the comparison of the heating power and the liquid enthalpy increase is displayed in Fig. 2.9 . The heat losses are negligible in this configuration.

The uncertainty on the heat flux q is estimated with:

$$\frac{\Delta q}{q} = \sqrt{\left(\frac{\Delta P_{ITO}}{P_{ITO}}\right)^2 + \left(\frac{\Delta D}{D}\right)^2 + \left(\frac{\Delta L}{L}\right)^2 \left(\frac{\Delta \eta}{\eta}\right)^2} \simeq 12.5\% \tag{2.9}$$

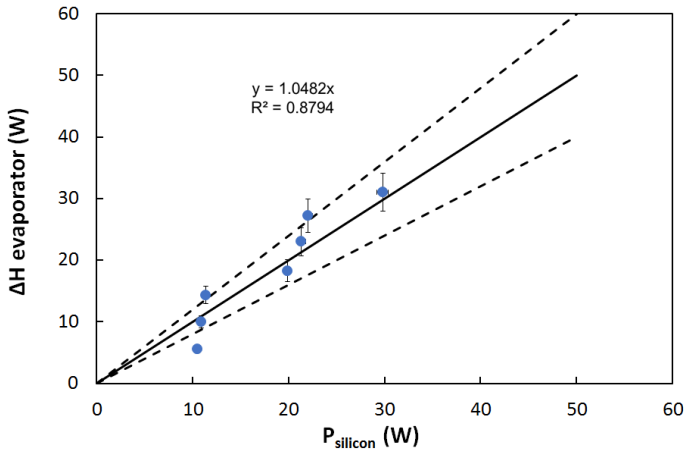

Figure 2.9: Thermal losses for the silicon tube

In soobcooled boiling, the quality $x(z)$ is equal to:

$$x_{sub}(z) = \frac{\frac{4qz}{GD} - C_p\left(T_{i\infty}(z) - T_3\right)}{h_{lv} + C_p\left(T_{sat} - T_{i\infty}(z)\right)} \tag{2.10}$$

where T_3 is the liquid temperature measured by the thermocouple T_3 at the entrance of the test section and $T_{i\infty}(z)$ is calculated by a linear interpolation between temperatures measured at the inlet and the outlet of the test section.

Measurements of quality give access to the superficial velocities of gas and liquid, j_v and j_l.

$$j_v = \frac{Gx}{\rho_v} \tag{2.11}$$

$$j_l = \frac{G\left(1-x\right)}{\rho_l} \tag{2.12}$$

To access the mean liquid and vapor velocities, U_v and U_l, the measurement of the cross-sectional averaged void fraction α is required:

$$U_v = \frac{j_v}{\alpha} \tag{2.13}$$

$$U_l = \frac{j_l}{(1-\alpha)} \tag{2.14}$$

2.4 Void fraction measurements

Cross sectional averaged void fraction can be measured locally using different methods like conductance probes [10], [23], capacitance probes [61], [32] or flow visualization. Since the liquids being used in this experiment are dielectric, conductance probes cannot be used. For this experiment capacitance probes were built and implemented in BRASIL. In addition, the capacitance measurements are low cost, non-intrusive and relatively simple in construction. They can be used not only for void fraction measurement but also for flow pattern recognition.

Void fraction measurements allow quantifying the relative volume of vapor and liquid flowing in the cross section. Void fraction sensors were developed especially for this experimental set-up. Capacitance probes measure the capacitance of the liquid-vapor mixture. These sensors use the difference in electrical permittivity between the vapor and the liquid phase. Volumetric average void fraction can be measured from the capacitance, C, after calibration.

The measurement principle of these probes is based on the measurement of electrical impedance Z that is defined as:

$$\frac{1}{Z} = \frac{1}{R} + 2\pi j f C \tag{2.15}$$

Where R is the resistance between the measuring electrode and C is the capacitance and f is the supply frequency. For a parallel-plate capacitor, A is the surface of the electrodes, d the distance between them and f the frequency used to excite the plates. The effective capacitance C is defined as:

$$C = \frac{\varepsilon_0 \varepsilon_r A}{d} \tag{2.16}$$

and the electrical resistance R is defined as:

$$R = \frac{d}{A\sigma_e} \tag{2.17}$$

where ε_0 is the permittivity of void, ε_r the relative permittivity of the medium and σ_e the electrical conductivity.

If we apply a high frequency, f, in the case of a dielectric medium with low conductivity, the resistive term is small enough and the impedance is mainly dominated by permittivity

effects. In our case, this means that the volume of vapor and liquid going through the parallel electrodes of the capacitor will depend on the permittivity of each phase.

Fig. 2.10 is a detailed drawing of the void fraction sensors. The electrodes in the void fraction probe are copper sheets of 10 mm $\times$ 10 mm and 1 mm thick and are located on both sides of the tube. The measuring electrode is placed between two guard electrodes that avoid the fringe effect in our measurements. As seen in Fig. 2.3 there are two void fractions sensors installed in the test section.

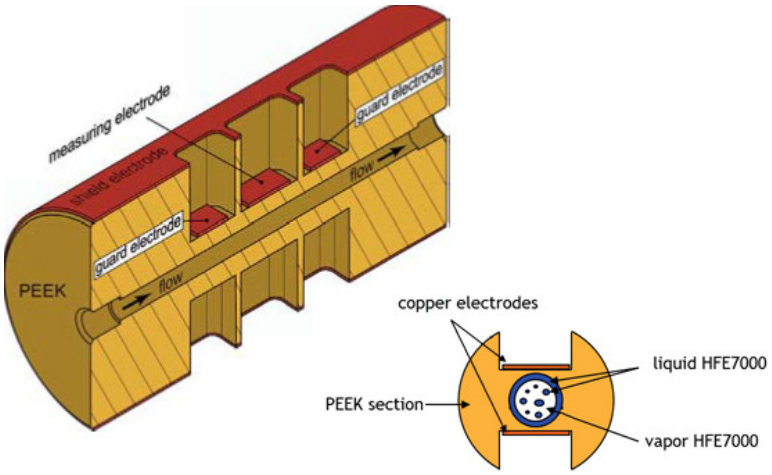

Figure 2.10: Detailed sketch of the void fraction sensor.

A review done previously helped determine the optimum configuration of the capacitance probes and a face-to-face configuration was chosen. The distance between the two opposite electrodes seen on the cross-sectional schematic is 10 mm. The distance between the electrodes was reduced to increase the accuracy of the capacitance measurements and to reduce its sensitivity to the two-phase distribution. An excitation frequency of 31.6 kHz was used during all the experiments.

Experimental calibration

For the determination of the void fraction from the capacitance measurements, a calibration curve is required. An easy way to calibrate a liquid-vapor flow is to simulate each phase with a material of a similar relative permittivity since it is the predominant effect.

The relative permittivity values are:

- Air : 1

- HFE 7000 vapor : 1.4
- Teflon : 2.1
- HFE 7000 liquid : 7.4

Several flow patterns are observed: bubbly flow, slug flow, and annular flow. The Teflon rods are used to mimic the vapor core in an annular flow. Since the permittivity of the Teflon is not exactly the same as HFE7000 vapor, the reduced capacitance is introduced:

$$C^* = \frac{C - C_v}{C_l - C_v} \tag{2.18}$$

Where C is the value of the measured capacitance, C_l the capacitance of the liquid and C_v for the calibration method are the teflon rods but for the experiments is the value measured with pure vapor in the tube.

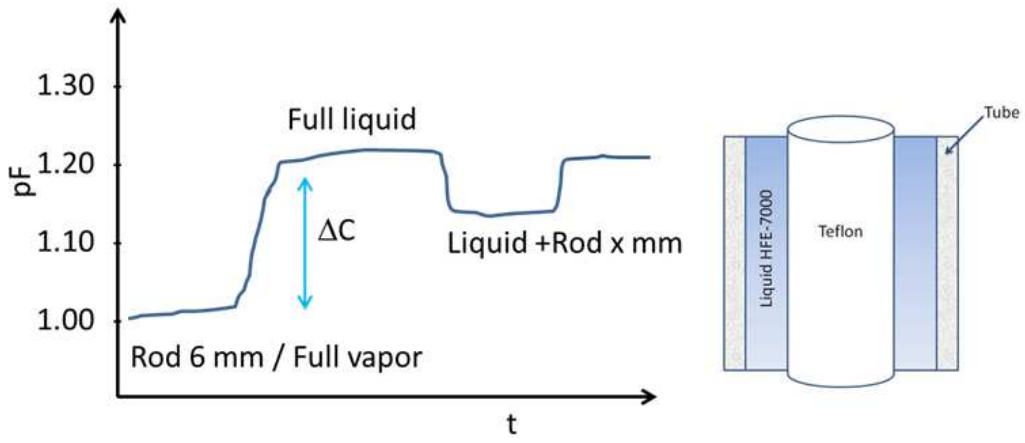

Figure 2.11: Calibration procedure

As stated before, Teflon rods are used as the vapor phase, so we used different diameter to vary the volume that represented the vapor. The liquid phase is liquid HFE 7000. Teflon rod diameters used for calibration were:

- 3.4 mm $-\triangleright$ 56.67% vapor
- 4.3 mm $-\triangleright$ 71.67% vapor
- 5.3 mm $-\triangleright$ 88.33% vapor
- 5.6 mm $-\triangleright$ 93.33% vapor

- 6.0 mm $-\triangleright$ 100% vapor

A protocol was carried out several times to assured repeatability. First, a measurement with air was performed as a zero value or starting point. The temperature of the electronics is also measured since it affects the capacitance measurement and it needs to be corrected at the end when the values are analyzed. After obtaining a zero point, runs will look like in Fig. 2.11. To start, during the same run a value of a teflon rod with a diameter equal to the inner tube diameter and then a full-of-liquid value will be recorded, like in Fig. 2.11 . After making sure the void fraction probe is properly dried a new run starts with air, then all-liquid, then the insertion of a new rod. Each rod diameter was immersed inside the void fraction sensor filled with HFE, and the capacitance values are recorded and processed.

To complete this experimental calibration, we simulated that same environment with COMSOL Multiphysics to compare both the experimental calibration and the simulation.

COMSOL Multiphysics calibration

COMSOL Multiphysics is a simulation tool we used to calculate the electrical field between the electrodes.

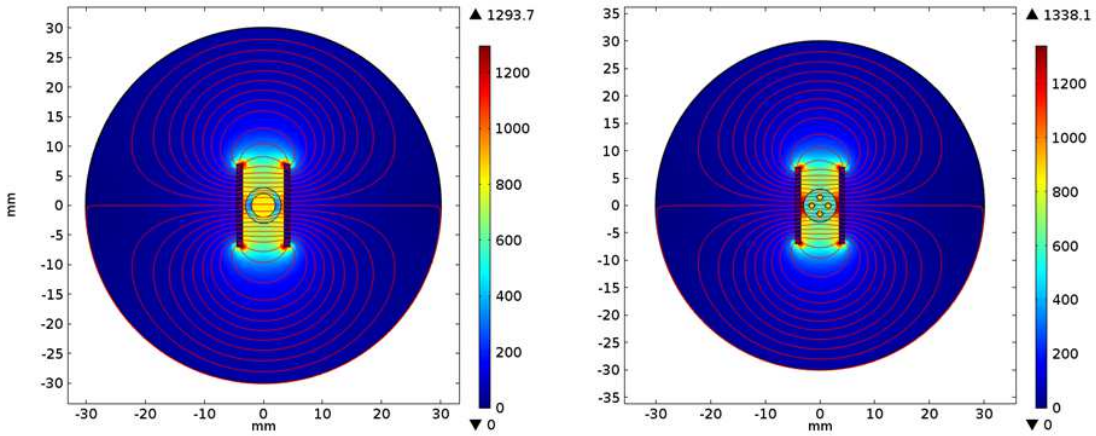

Figure 2.12: Electric field in the void fraction probe 2D.

First, a $2D$ numerical simulation of the electrical field between the 2 electrodes and around was performed for annular flows and bubbly flows (Fig. 2.12) with the permittivities of HFE 7000 liquid and vapor. To complete the analysis, a $3D$ design of the void fraction sensor was made and the simulation of the calibration was ran to the results with the experimental values.

As a boundary condition on the electrodes we applied the Voltage V_{ref}, at a constant value of 5 V. For the 2D design it was necessary to specify the thickness of the domain (1 mesh

size is 1 mm). The Capacitance calculated for the simple plane capacitor, on pen and paper, and with COMSOL had a difference of 0.73% so based on that we proceed with the simulation.

For the equations solved by the software, COMSOL claims that the boundary conditions for the exterior (2.19a) and the interior (2.19b) boundaries are assigned by the following equations:

$$\mathbf{-n} \cdot \mathbf{D} = \varepsilon_0 \varepsilon_r \frac{V_{ref} - V}{d_s} \tag{2.19a}$$

$$\mathbf{n} \cdot (\mathbf{D}_1 - \mathbf{D}_2) = \varepsilon_0 \varepsilon_r \frac{V_{ref} - V}{d_s} \tag{2.19b}$$

where ε_r is the relative permittivity and d_s the electrode thickness connected to the reference potential V_{ref} and $\mathbf{D}$ is the distributed capacitance.

New void fraction sensors were built to improve the accuracy the measurements of the capacitance and therefore of the void fraction in the experiments. The distance between the electrodes was reduced from 15 mm to 10 mm. The calibration curve shown on Fig. 2.13 shows first of all, a good repeatability between the two probes despite the fact that, experiments are run at two different temperature conditions.

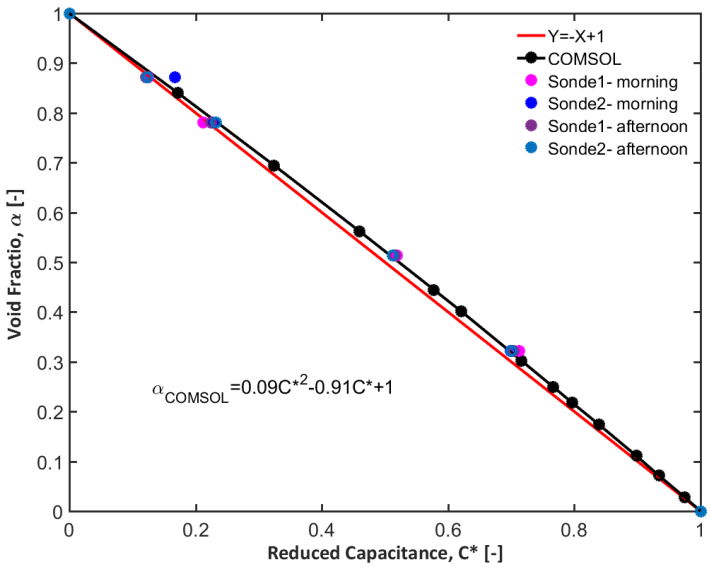

Figure 2.13: Calibration curve compared to COMSOL simulations [76]

We always plot the reduced capacitance, C^* since Teflon does not have the exact same permittivity as HFE's vapor. Comparison is then possible only by normalizing the capacitance.

The capacitance probes are not sensitive to the flow configuration. Same calibration curve is obtained for annular, slug and bubbly flow:

$$\alpha = -0.09C^{*2} - 0.91C^{*} + 1 \tag{2.20}$$

The capacitance measurements will be used to determine the void fraction and the liquid film thickness in annular flow. The signal sensibility (corresponding to the capacitance difference between liquid state and vapor state $C_{liq} - C_{vap}$) is around 0.2 pF. The accuracy on the measurement is $\Delta C = 0.001pF$. The error on the capacitance measurements is mainly due to the drift of the capacitance with the temperature of the electronics. The value is close to $\Delta C_l \simeq 0.005\ pF$. The relative uncertainty on the reduced capacitance C^* is equal to:

$$\Delta C^* = \sqrt{2\left(\frac{\Delta C}{C_l - C_v}\right)^2 + 2\left(\frac{2\Delta C\,(C_l - C_v)}{(C_l - C)^2}\right)^2} \simeq 4\% \tag{2.21}$$

The uncertainty on the void fraction itself depends on the precision of the calibration and it is estimated at $\Delta\alpha = 0.04$ for $\alpha > 0.2$: $\frac{\Delta\alpha}{\alpha} \simeq 0.05$. COMSOL simulations were used to calibrate the void fraction probes, but also to help to optimize their shape for a better measurement accuracy.

2.5 Heat Transfer Coefficient measurements: Sapphire tube

To accurately calculate the heat transfer coefficient different assumptions and calculations were made. To explain it better, in Fig. 2.14b is shown the schematic of the cross-section of the heated tube, where T_{ow} is the outer wall temperature measured at different heights (indicated in Fig. 2.14a), T_{iw} is the inner wall temperature and $T_{i\infty}$ is the liquid bulk temperature. This bulk temperature is measured by thermocouple T_3 at the inlet of the test section and Pt100 probe $Spl4$ at the outlet of the test section. The heat flux at the inner wall q is estimated by taking into account the heat losses (section 2.3).

The heat transfer coefficient is calculated versus the heat flux, and the difference $T_{iw} - T_{i\infty}$:

$$h_i = \frac{q}{T_{iw} - T_{i\infty}} = \frac{q}{T_{ow} - \frac{R_i}{k} ln\left(\frac{R_o}{R_i}\right) q - T_{i\infty}} \tag{2.22}$$

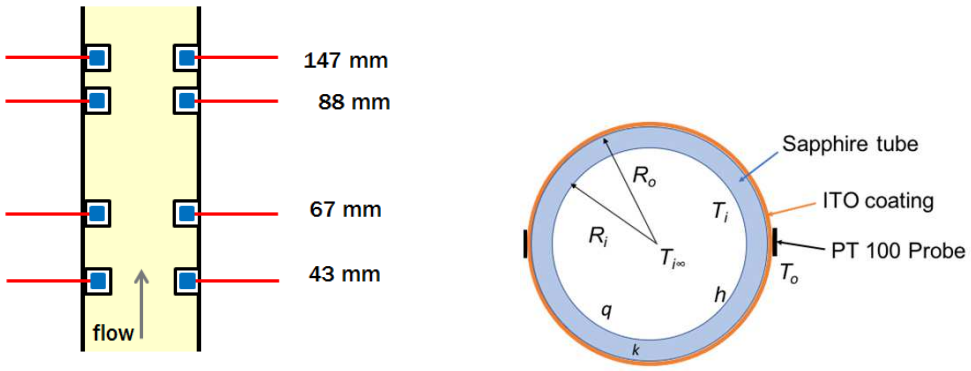

(a) Pt100 probes on the wall (b) Cross-section of the tube

Figure 2.14: Temperature sensors on the wall used to calculate the heat transfer coefficient.

where R_i and R_o are the inner and outer tube radii. The inner wall temperature is calculated considering the conduction through the sapphire wall. k is the thermal conductivity of the sapphire about equal to 31 $W/m/K$. The wall temperature T_{ow} is measured on both sides of the tube.

The good agreement of the measured values on both sides show the homogeneity of the ITO coating around the tube, Fig. 2.15.

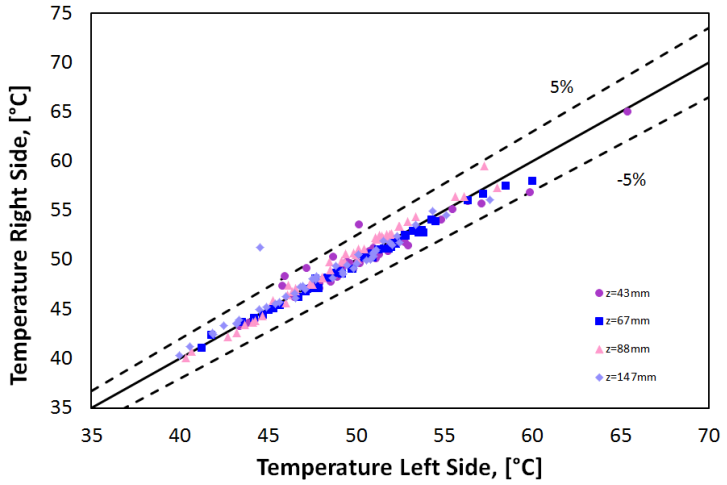

Figure 2.15: Measurements on both sides of the tube.

To be able to calculate, $T_{i\infty}$ the bulk temperature, the evolution between the inlet and the outlet of the test section, as mentioned before, is consider as a linear evolution along the tube [61].

The uncertainty on the heat transfer coefficient is equal to:

$$\frac{\Delta h_i}{hi} = \sqrt{\left(\frac{\Delta q}{q}\right)^2 + \left(\frac{\Delta T_{iw}}{T_{iw} - T_{i\infty}}\right)^2 + \left(\frac{\Delta T_{i\infty}}{T_{iw} - T_{i\infty}}\right)^2} \simeq 15\% \tag{2.23}$$

with

$$T_{iw} = T_{ow} - \frac{R_i}{k} ln\left(\frac{R_o}{R_i}\right) q \tag{2.24}$$

$$\Delta T_{iw} = \sqrt{(\Delta T_{ow})^2 + \left(\frac{Ri}{k} ln \frac{R_o}{R_i}\right)^2 + (\Delta q)^2 \left(\frac{Ri}{k^2} ln\left(\frac{R_o}{R_i}\right) q\right)^2 (\Delta k)^2} \tag{2.25}$$

For the validation of the heat transfer coefficient measurements, experiments in single-phase flow were performed. In Fig. 2.16 the Nusselt number, Nu, calculated for each position of the temperature sensor and corrected with Al-Arabi's [2] correlation, is compared to the Gnielinski correlation [35] for turbulent flows, $Re > 2000$. In forced convection Nu depends on the Reynolds number Re and the Prandtl Number Pr. Gnielinski's correlation takes into account the contribution of the the wall roughness and transitional flow conditions. Gnielinski's correlation only applies to fully developed heat transfer conditions.

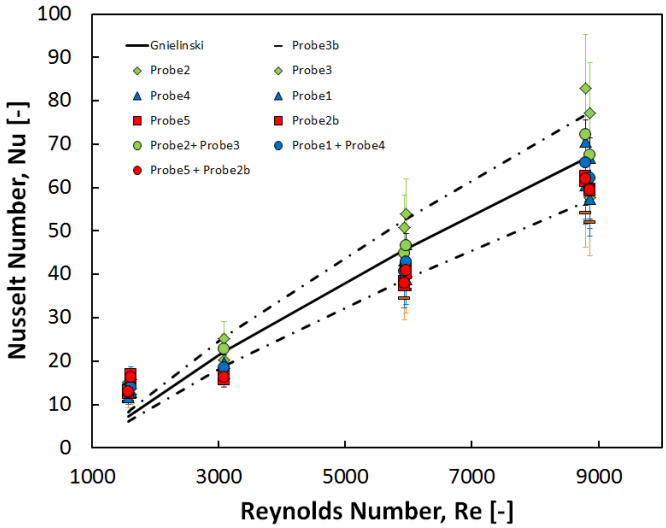

Figure 2.16: Single-phase flow experiments for heat transfer technique validation with Al-Arabi's correction.

A good agreement between the experimental measurements and the correlation of Gnielinski

validates the measurement techniques.

$$Nu = \frac{(f/2)Re^{4/5}Pr^{0.4}}{1 + 12.7(Pr^{2/3} - 1)\sqrt{f/2}} \tag{2.26}$$

where the friction factor is best calculated with an approximation of the Colebrook correlation in this case for a smooth tube:

$$f = 4(0.790lnRe - 1.64)^{-2} \tag{2.27}$$

Al-Arabi's correction is necessary since the previous correlation applies to locations far from the entrance of the tube, in our case $L/D \gg 10$ is not complied and the Nusselt number changes. Al-Arabi proposed a correlation to correct the entrance effects:

$$\frac{Nu_a}{Nu_\infty} = 1 + \frac{\frac{(z/D)^{0.1}}{Pr^{1/6}}\left(0.68 + \frac{3000}{Re^{0.81}}\right)}{z/D} \tag{2.28}$$

where Nu_a is the actual Nusselt number, which is larger than the values of the Nusselt number in the fully thermally developed flow, Nu_∞, because of the development of the thermal boundary layer [2]. In Fig. 2.16, the value of Nu_a is plotted for comparison with Gnielinski's correlation.

2.6 Heat Transfer Coefficient measurements: Silicon tube with infrared thermography

The technique used to measure the heat transfer coefficient using a silicon tube was based on infrared thermography developed by Kim et al.[49] and used by Scammell [74] for the analysis of heat transfer around a rising Taylor Bubble.

With this technique outer and inner wall temperatures can be measured at the same time. It gives access to a local heat transfer coefficient and its evolution along the tube with high spacial and temporal resolutions. Silicon is transparent to the IR radiation in the wavelength range of the camera ($3 - 7\mu m$). The IR camera used was provided by the European Space Agency. It is a high speed infrared camera with a chosen field of view of 320x2560 pixels. Since silicon is highly conductive, the inner surface of the tube is covered with a polyimide tape in order to create a radial temperature gradient in the tube and to be able to measure the local heat flux at the inner wall, Fig. 2.17.

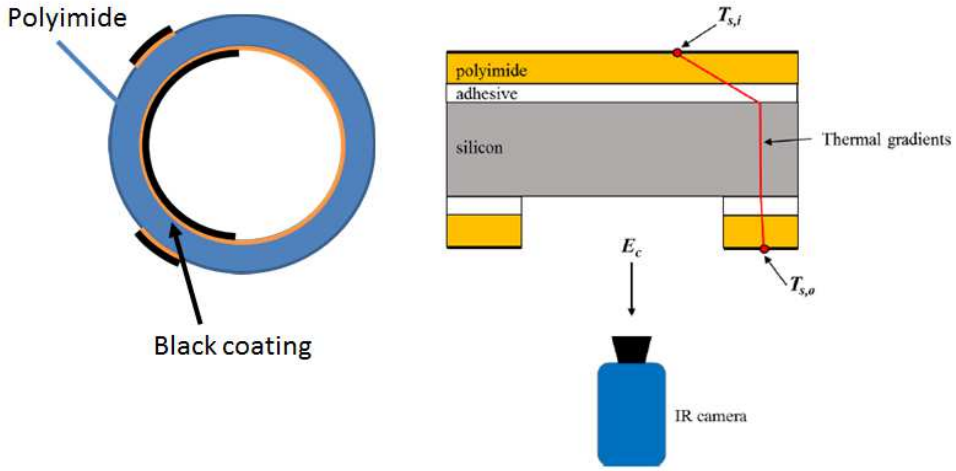

Figure 2.17: Layers of the tube

Around the silicon tube, an array of 6 mirrors (Fig. 2.17a) allows a simultaneous view of half of the tube with the black coating, where the temperature measurements are performed. The other half of the tube is used for flow visualization since HFE 7100 is semitransparent to the IR camera, Fig. 2.18a shows a typical image observed through the IR camera.

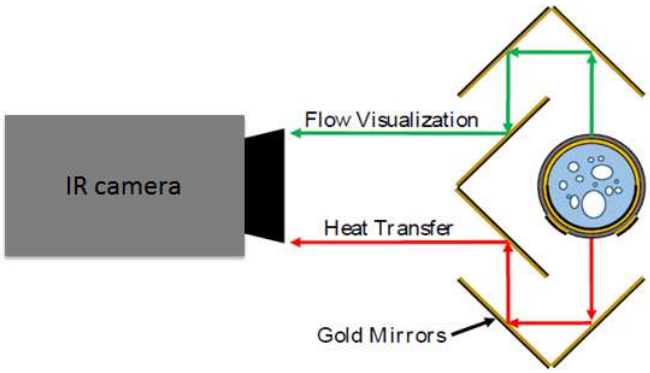

(a) Schematics of the thermometry principle [74]

Figure 2.17: IR camera thermometry technique

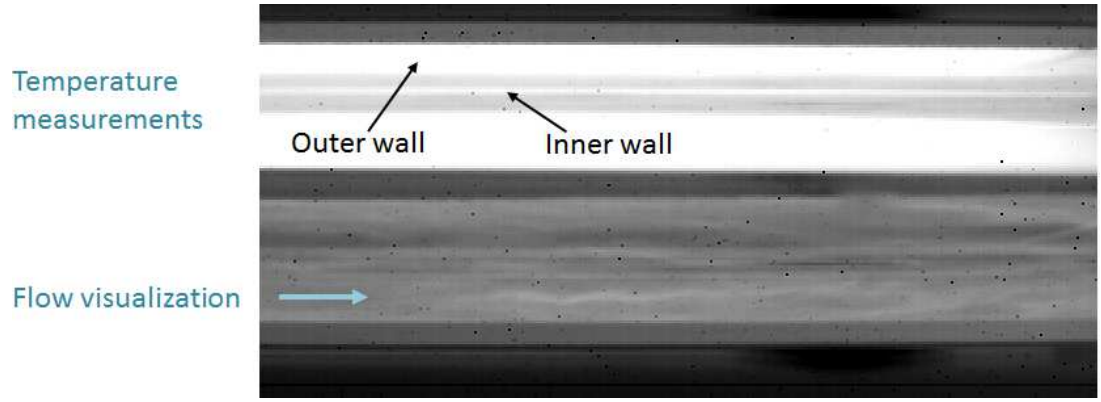

(a) Typical image obtained from the IR camera with the upper image measuring temperature and the lower image allowing flow visualization

The thin film of polyimide tape was black painted to allow the measurement of the inner wall temperature. Temperature distributions were calculated from the multilayer, Fig. 2.17, using a 1-D conduction equations for silicon Eq. 2.29a, adhesive Eq. 2.29b, and polyimide Eq. 2.29c:

$$\rho_{Si} C_{p,Si} \frac{\partial T}{\partial t} = k_{Si} \frac{\partial^2 T}{\partial^2 x} + q_{Si} \tag{2.29a}$$

$$\rho_{A} C_{p,A} \frac{\partial T}{\partial t} = k_{A} \frac{\partial^2 T}{\partial^2 x} \tag{2.29b}$$

$$\rho_{P} C_{p,P} \frac{\partial T}{\partial t} = k_{P} \frac{\partial^2 T}{\partial^2 x} \tag{2.29c}$$

where ρ, C_p, k are the density, specific heat and thermal conductivity of the materials: Silicon, Si, Adhesive, A, and polyimide, p, q_{Si}, is the power density per unit volume, and x the coordinate in the radial direction. The boundary condition $T = T_{S,o}$ at the outer wall and $T = T_{S,i}$ at the liquid-polyiamide interface ("inner wall"), $x = 0$, are used for the resolution.

The temperatures $T_{S,o}$ and $T_{S,i}$ are not directly accessible from the infrared images. For the outer surface of the tube the energy recorded by the camera E_c is the sum of the energy $E_{s,o}$ emitted by the black surface of emissivity ε_s and the energy reflected by the surrounding E_∞.

$$E_c = (1 - \varepsilon_S) E_\infty + \varepsilon_S E_{s,o} \tag{2.30}$$

with $E_\infty = F_{\lambda_1 - \lambda_2} \sigma T_\infty^4$ and $E_{S,o} = F_{\lambda_1 - \lambda_2} \sigma T_{S,o}^4$

$F_{\lambda_1-\lambda_2}$ is the portion of the energy emitted in the wavelength interval $(\lambda_1 - \lambda_2)$ of the IR camera $(3-7\mu m)$. This function can be calculated by integrating the Plank's distribution or from tables. Planck's law defines the distribution of spectral density of electromagnetic radiation emitted by a black body in thermal equilibrium at a given temperature.

For the outer wall, first we start from a guess value of the temperature T_g for a first iteration. Second, we calculate the temperature of the surface $T_{s,o}$ updating for T_g, from Eq. 2.30. Third, changing $T_g = T_g + \frac{T_{s,o}-T_g}{2}$ and finally repeating second and third for a new T_g until the difference between $T_{s,o}$ and T_g is smaller than 10^{-6}. The effect of the assumed initial temperature profile within the multilayer will disappear and the real temperature of the profile will be known.

For the inner wall, this energy is the sum of the energies emitted by each layer withing the spectral bandwidth of the IR camera:

$$E_c = \rho_{\infty-c}E_\infty + \varepsilon_{Si-c}E_{Si} + \varepsilon_{T-c}E_T + \tau_{s-c}E_{s,i} \tag{2.31}$$

Coefficients $\rho_{\infty-c}$, ε_{Si-c}, ε_{T-c} and τ_{s-c} take into account effective reflectivity of the multilayer, the effective emissivity of the silicon, the effective emissivity of the combined layer of polyimide and adhesive and the effective transmissivity of the multilayer, respectively and are given by [Kim et al. 2012 [49]]:

$$\rho_{\infty-C} = \rho_{\infty-Si} + \frac{(1-\rho_{\infty-Si})^2\rho_{app,Si-T}\tau_{Si}^2}{1-\rho_{\infty-Si}\rho_{app,Si-T}\tau_{Si}^2} \tag{2.32a}$$

$$\varepsilon_{Si-c} = \frac{(1-\rho_{\infty-Si})^2\rho_{app,Si-T}\tau_{Si}^2}{1-\rho_{\infty-Si}\rho_{app,Si-T}\tau_{Si}^2} \tag{2.32b}$$

$$\varepsilon_{T-c} = \frac{(1-\rho_{Si-\infty})(1-\rho_{Si-T})(1+\rho_{T-s})\tau_{Si}}{(1-\rho_{\infty-Si}\rho_{app,Si-T}\tau_{Si}^2)(1-\rho_{Si-T}\rho_{T-s}\tau_T^2)} \tag{2.32c}$$

$$\tau_{s-c} = \frac{(1-\rho_{Si-\infty})(1-\rho_{Si-T})(1+\rho_{T-s})\tau_{Si}\tau T}{(1-\rho_{\infty-Si}\rho_{app,Si-T}\tau_{Si}^2)(1-\rho_{Si-T}\rho_{T-s}\tau_T^2)} \tag{2.32d}$$

$$\rho_{app,Si-T} = \rho_{\infty-Si} + \frac{(1-\rho_{Si-T})^2\rho_{T-s}\tau_T^2}{1-\rho_{Si-T}\rho_{T-s}\tau_T^2} \tag{2.32e}$$

In order to obtain the temperature distribution an algorithm that coupled the conduction and radiation problems is solved [49].

α_{Si}	α_T	ρ_{Si-air}	ρ_{Si-T}	ρ_{air-T}
55 m^-1	9500 m^-1	0.313	0.14	0.07

Table 2.2: Optical properties values used for the tape and the silicon tube.

The optical properties of all different layers have been determined by Kim et al. [49], Table 2.2, and the temperature from the environment, T_∞ is measured by a thermocouple. $T_{s,i}$: First, we assume an arbitrary temperature profile within the multilayer at $t = 0$. Second,

compute E_{Si} and E_T from the temperature distribution and determine an updated $E_{s,i}$ and surface temperature $T_{s,i}$ from Eq. 2.31. Third, solve the conduction equation using the updated $T_{s,i}$ to obtain a new temperature profile at $t = \Delta t$. Then repeat steps 2 and 3 for each time step.

After convergence of the calculation, the heat flux ant the inner wall is calculated from the derivation of the local instantaneous temperature profile:

$$q = -k_p \frac{\partial T}{\partial x}\Big|_{x=0} \tag{2.33}$$

To begin with the image analysis, a calibration with a black body was made to obtain a relation between the gray level of the camera characterizing the energy and the temperature of the black body T_{BB} Fig. 2.19.

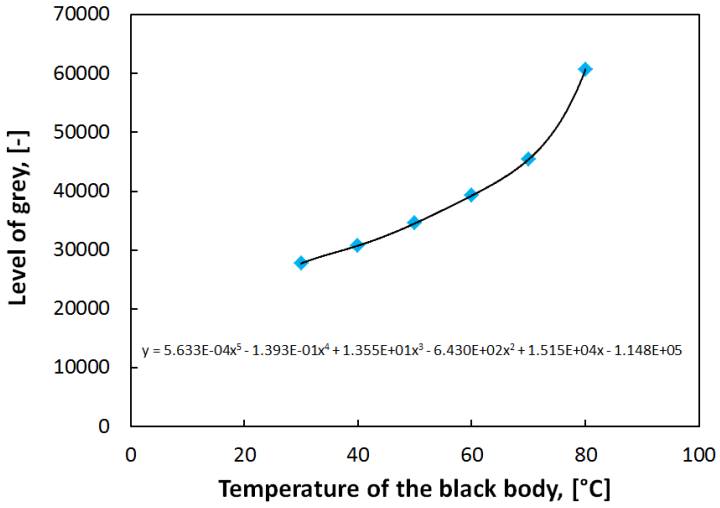

Figure 2.19: Level of gray as a function of the temperature of a black body.

Then the gray level of the camera can be related to the energy emitted by the black body $F_{\lambda_1-\lambda_2}\sigma T_{BB}$ and measured by the IR camera.

$$E_c = F_{\lambda_1-\lambda_2}\sigma T_{BB}^4 \tag{2.34}$$

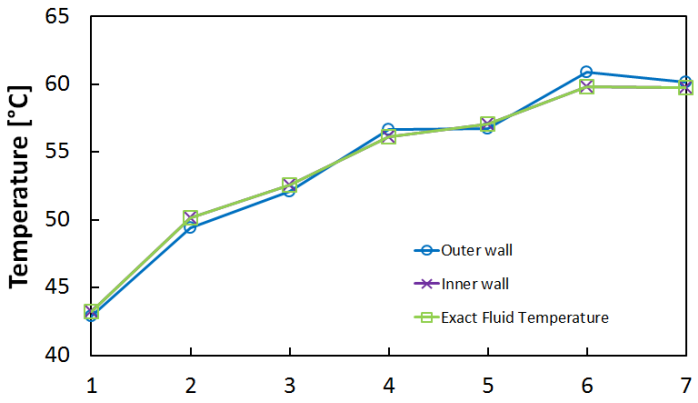

Figure 2.20: Temperature wall for single-phase validation.

Fig. 2.20 presents the measurements obtained in single-phase flow. Constant temperature runs, with an impose liquid temperature at the entrance and an unheated wall, were performed to validate the temperature measurements. Taking into account the high conductivity of the silicon tube, values of the 3 temperatures must be in a very close range. As we can see in Fig. 2.20 the temperature calculated from the initial measurements are coherent and agree with each other.

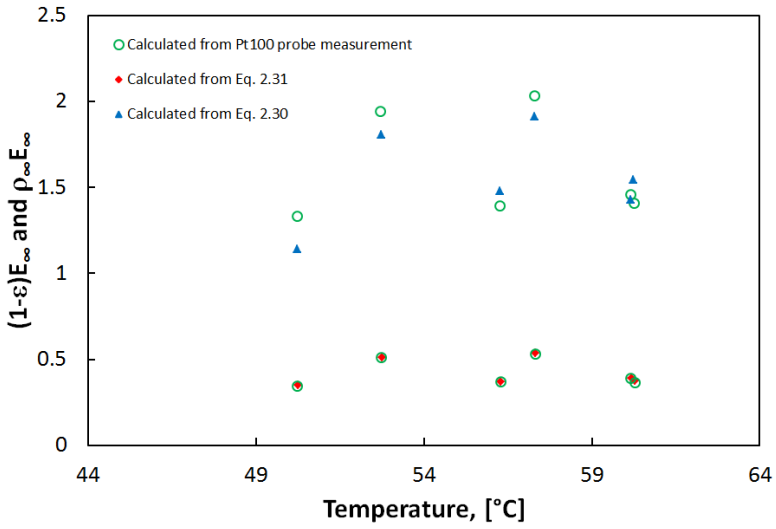

Figure 2.21: Calculation of $\rho_\infty E_\infty$.

As shown in Fig. 2.21 single-phase are also used to estimate the value of the $\rho_\infty E_\infty$ from the value measured by the Pt100 probe that measured the temperature of the environment

and the value estimated with Eq. 2.30 and Eq. 2.31. We can see the the values from Eq. 2.34 is more accurate due to less error entrained by other variables.

To validate the values of the heat transfer coefficient, results for single-phase runs are are compared to those estimated by Dittus-Boelter correlation and presented in Fig. 2.22.

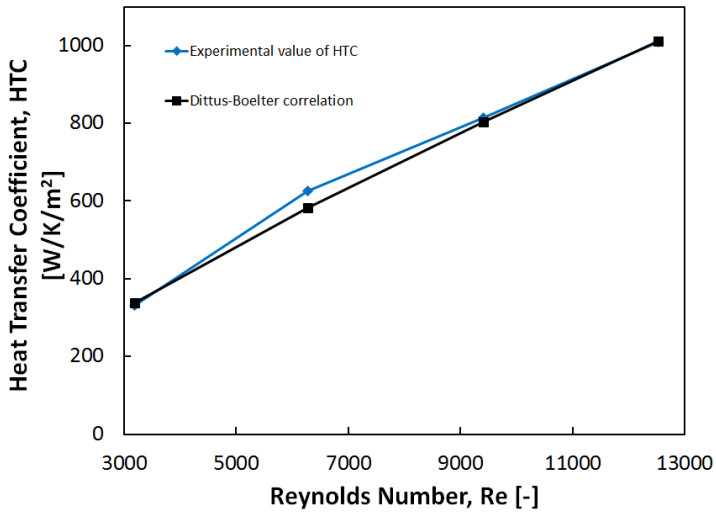

Figure 2.22: Single-phase validation of temperature wall with Dittus-Boelter correlation.

Kim et al. [49] made an uncertainty analysis in the calculated heat flux by perturbing each experimental parameter a small amount to quantify the sensitivity to the variables at varying heat flux. Physical constants are considered to introduced a negligible error. The highest error were presented by:

Constante	Value	Uncertainty
Emisivity of the black coating	0.9	0.01
Absorptivity of the polyimide tape	7110 m^{-1}	500 m^{-1}
Adhesive thickness	15 μm	2 μm
Reflectivity of silicon-air interface	0.34	0.017
Reflectivity of silicon-polyimide interface	0.14	0.007
Thermal conductivity of polyimide	0.12 W/mK	0.010 W/mK
Thermal conductivity of adhesive	0.20 W/mK	0.010 W/mK

Table 2.3: Largest effect on uncertainty analysis.

Fig. 2.23 present the acquisition of local HTC and the evolution of the temperatures measured by the IR camera. The analysis of this data was carried out by Achour [1].

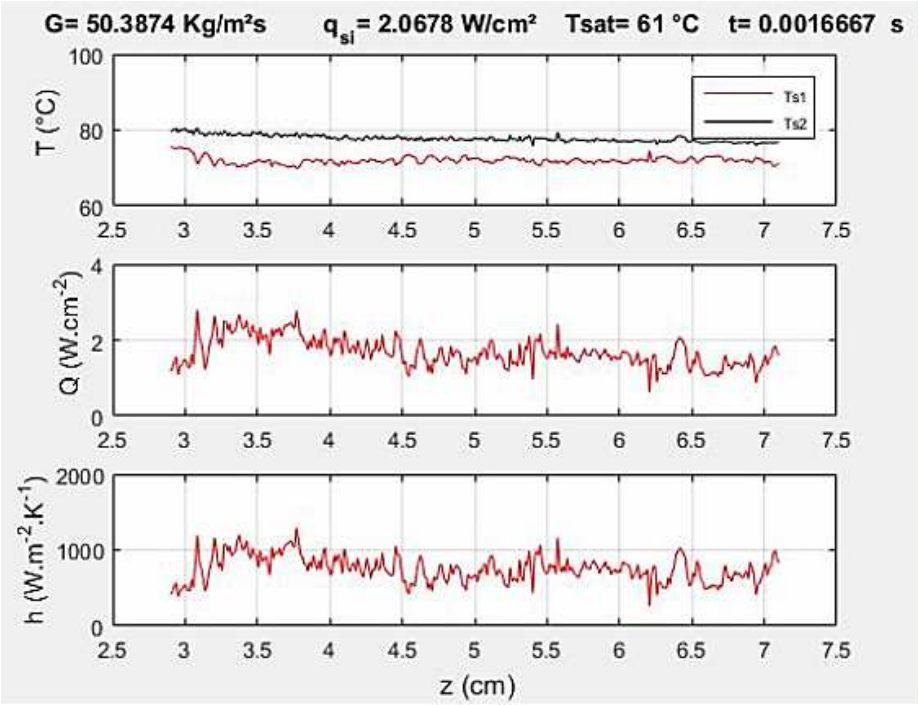

Figure 2.23: The evolution of the inner temperature and the outer temperature along the tube, the heat flux and the HTC.

2.7 Visualization

A high speed camera (PCO 1200 HS, 1200x1000 pixels) was installed for the visualization and identification of the flow patterns in both experiments. It directly films through the sapphire tube or in case of the glass tube downstream the silicon tube. During parabolic flights, the camera recorded images only during the microgravity phases with a field of view of 65x10 mm. It captured at a frequency of 1000 Hz, 1650 Hz, or 1983 Hz depending on the test running and it is synchronized with the acquisition system. The spacial resolution is 20 pix/mm. During ground experiments another high speed camera was used (PCO Dimax, 2000x2000 pixels). This camera allowed to film the whole tube so we could observe the evolution of the flow patterns along the tube. The spacial resolution of this camera is 12 pix/mm.

An example of flow visualization for bubbly and annular flow in normal and microgravity conditions is shown in Fig. 2.24

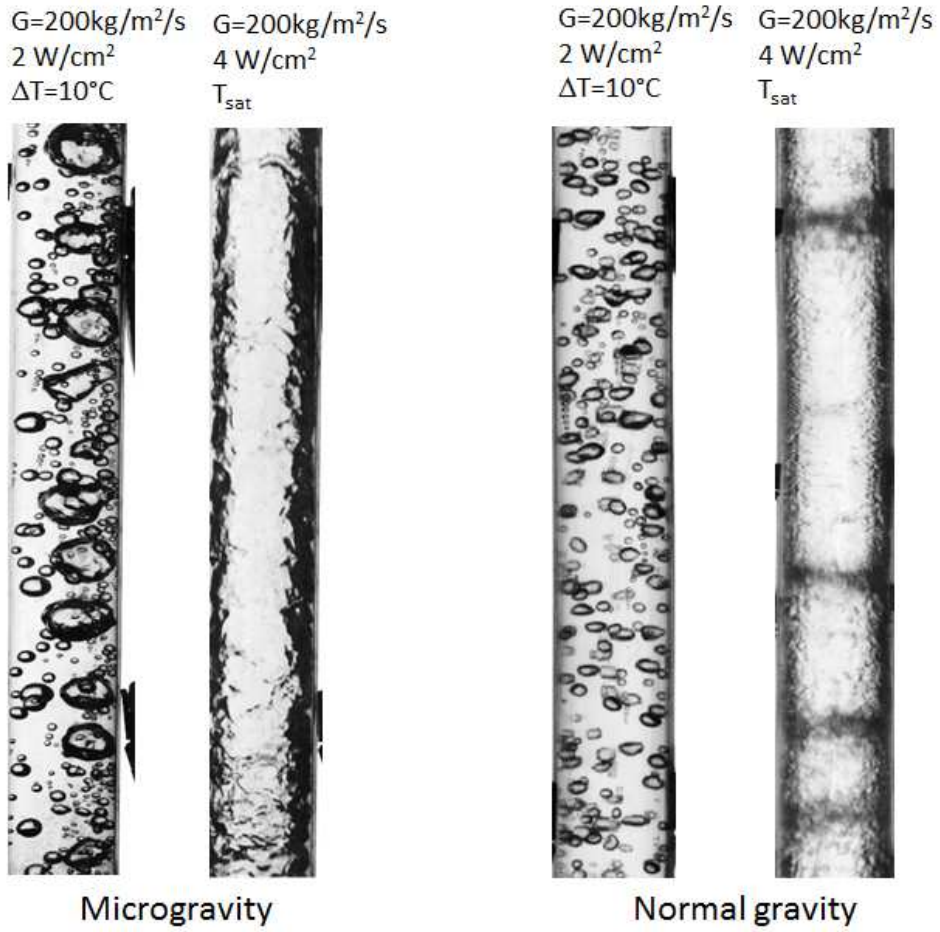

Figure 2.24: Visualization with both cameras for a mass flux during the flight campaign and ground measurements.

2.8 Parabolic flights

Parabolic flights are used to conduct short-term scientific and technological investigations in microgravity and reduced gravity, to test instrumentation prior to use in space, to validate operational and experimental procedures, and to train astronauts for a future space flight.

Such flights are conducted on specially-configured aircraft, and provide repetitively periods of up to 20 seconds of microgravity or weightlessness. On each parabola, from a steady horizontal flight, the aircraft gradually pulls up its nose and starts climbing up to an angle of approximately 47 °C.

During this phase that lasts for about 20 seconds, the aircraft experiences an acceleration of around 1.8 times the gravity level at the surface of the Earth, i.e. 1.8 g. The engine thrust is then strongly reduced to the minimum required to compensate for air-drag, and the aircraft then follows a free-fall ballistic trajectory, a parabola, lasting approximately 20 seconds, during which weightlessness is achieved, see 2.25.

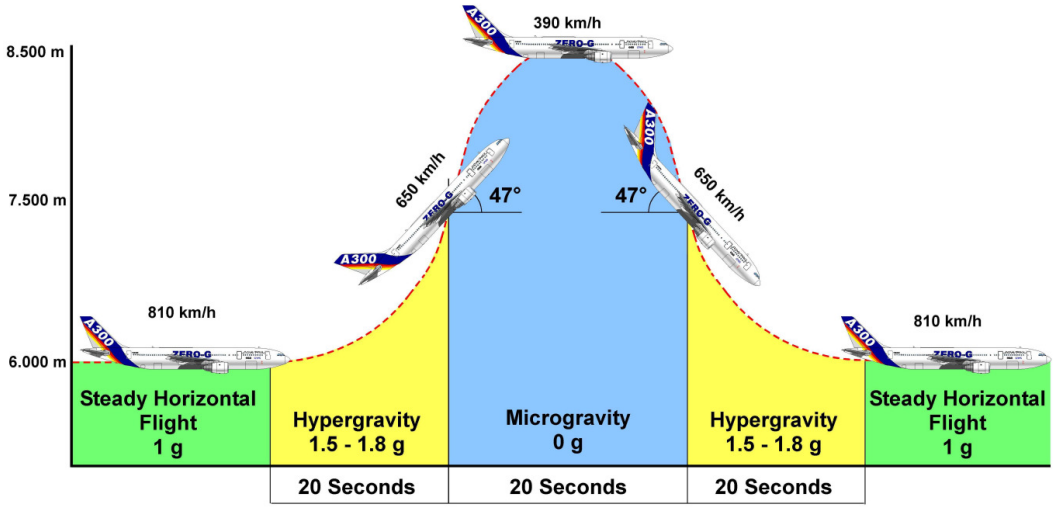

Figure 2.25: A300 Trajectory profile.

At the end of this period, the aircraft must pull out of the parabolic arc, a manoeuvre which gives rise to another 20 second period of 1.8 g on the aircraft, after which it returns to normal level flight attitude.

These maneuvers are flown repeatedly, with a period of 3 minutes between the start of two consecutive parabolas, i.e. a 1 minute parabolic phase (20 seconds at 1.8 g + 20 seconds of weightlessness + 20 seconds at 1.8 g), followed by a 2 minutes "rest" period at 1 g. After every group of five parabolas however, the rest interval is of 5 minutes.

Throughout the flight, all personnel are kept continuously informed of the flight status, i.e.

indication of how many seconds to the next parabola, number of minutes of rest period, etc.

During each parabolic flight and during each trajectory as shown in fig.2.25 the experiment was on and with the fluid circulating. For each parabola the first thing to do was to set the parameters and start the data acquisition before the $1.8g$ period. The parameters were G given by the flowmeter, q_{ITO} the power of the coating of the tube, which imposes the wall heat flux and P_{pre} the power of the preheaters which fixes the inlet quality of the flow or the liquid subcooling. During the microgravity period high speed video pictures of the flow were recorded during 10 seconds.

Figure 2.26: Zero-G Airbus A300 used to perform the parabolic flights.

After each parabola, the data of the camera and the acquisition device are saved. Then new parameters are set and start again the process. It is important to maintain communication during the flight to make sure everyone is being able to do his part of the job and to be aware of any problems on board.

Fig. 2.27 shows a sequence of signal recording during one parabola, with the evolution of acceleration, mass flow rate, wall temperatures. A PID was used to maintain a constant mass flow rate despite the rapid change of pressure gradient in the circuit. It can be seen on this figure that 5 s are sufficient to reach a steady state during the microgravity period.

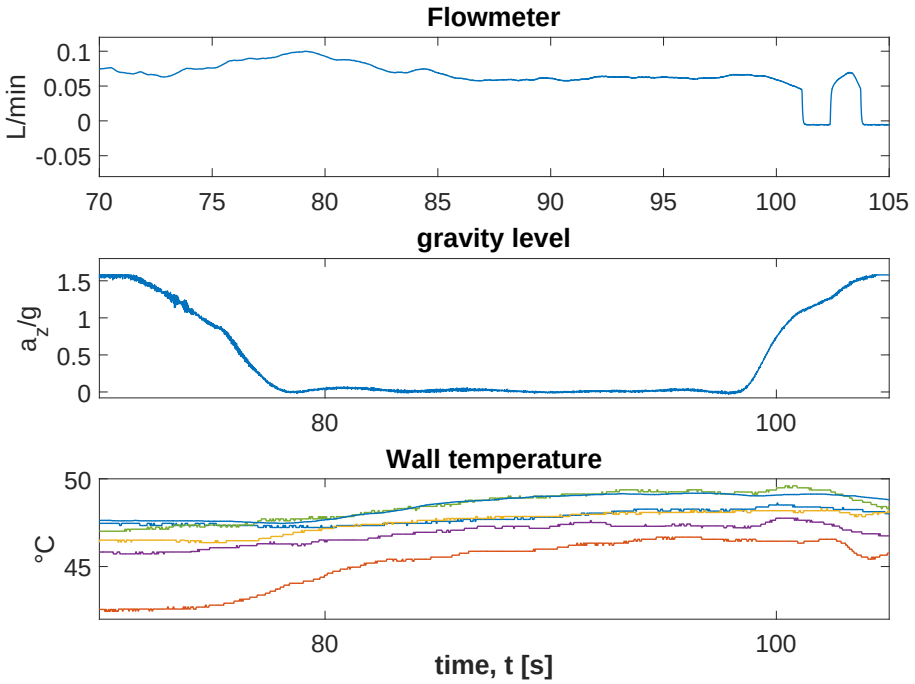

Figure 2.27: Acquisition of Flowmeter, accelerometer and Pt100 probes on the wall measuring the external temperature.

2.9 Conclusion

The experimental set-up BRASIL was built and designed at IMFT to acquire data on various parameters affecting flow boiling. Protocols and procedures are developed to test flow boiling under normal and microgravity conditions. The instrumentation will give access to the quality values along the test section, the liquid temperature, void fraction and heat transfer coefficient, as well as the flow patterns.

The measurement of the heat transfer coefficient has been validated in single-phase flow by comparison with empirical correlations of the literature. This validation is crucial to assess the accuracy of the measurement techniques and to be able to compare our results with other data sets obtained in similar conditions.

Chapter 3

Experimental Results

This chapter presents the experimental results obtained during parabolic flights and on-ground experiments. The results are compared to other correlations of the literature presented in Chapter 1. First, flow visualization for different mass fluxes, heat fluxes and inlet qualities are described. The transitions between the flow patterns are then discussed. A second part is dedicated to the void fraction measurements which are used to evaluate the mean vapor velocity in bubbly and slug flows and the film thickness in annular flow. The third section is focused on the heat transfer coefficient measured with both measurement techniques described in Chapter 2. The differences found for normal and microgravity, the comparison with correlations that predict heat transfer coefficient and contribution of nucleate and convective boiling depending on the regime are presented. The last part of this chapter is devoted to the analysis of interfacial structure of the liquid film in annular flows and the characterization of the velocity and frequency of the disturbance waves.

3.1 Visualization and flow patterns

The experimental set-up, presented in Chapter 2, allowed the visualization of the flow during the experimental runs performed with BRASIL. Fig. 3.1 and 3.2 represent snapshots of the flow patterns observed for vertical upward flow on ground for two mass fluxes $G = 50\ kg/m^2/s$ and $G = 200\ kg/m^2/s$ for different inlet conditions, from subcooled boiling $-10\ °C$ to saturated condition with quality of $x = 0.2$, and for different wall heat fluxes $q = 0.5\ W/cm^2$ to $4\ W/cm^2$.

The onset of nucleate boiling (ONB) is clearly visible in the test section in subcooled boiling ($T_{in} = T_{sat} - 10\ °C$). For $G = 200\ kg/m^2/s$ at low heat flux it occurs close the tube outlet. As the heat flux increases, it occurs closer to the tube inlet. The same trend is observed for $G = 50\ kg/m^2/s$. In saturated boiling, ONB occurs most of the time upstream the entrance of the test section. Liquid and vapor distribution strongly depends on the quality values. In subcooled boiling, after the ONB, *bubbly flow* is observed (Fig. 3.1 and 3.2 for $T_{in} = T_{sat} - 10\ °C$).

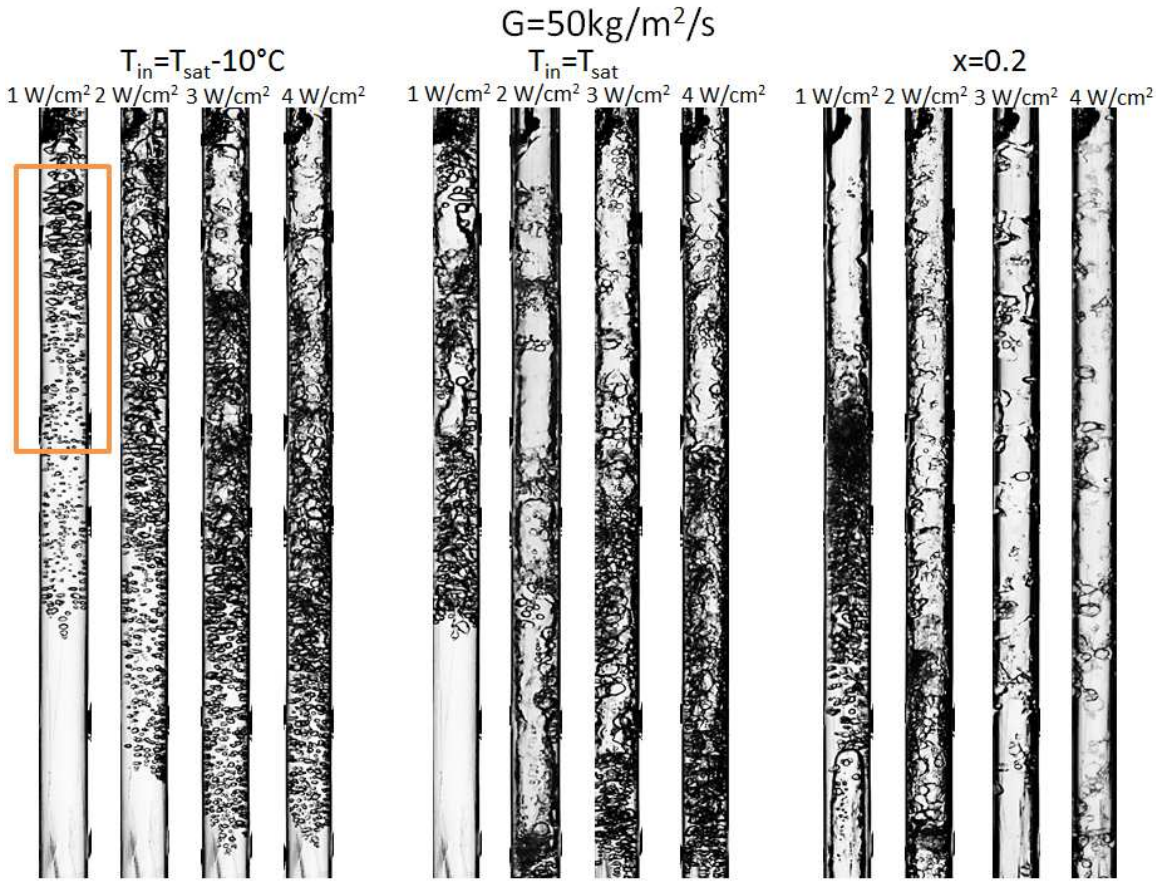

Figure 3.1: Flow regimes in normal gravity.

Very small bubbles nucleate on the wall, slide along the wall and are detached and entrained in the liquid flow. If the liquid is subcooled bubbles re-condense in the liquid core. In saturated boiling, bubbles coalesce leading to larger bubbles with a size close to the tube diameter D. In this study, bubbly flow regime is defined when bubble size is smaller to the inner diameter D.

As the void fraction or quality increases, larger bubbles are created. *Slug flow* is considered to happen when bubbles have a diameter bigger than D and are deformed creating what is usually called a Taylor bubble, followed by a slug of liquid. These long bubbles, which have a smooth interface and a spherical shaped nose, are separated by liquid slugs. These slugs contain smaller bubbles (Fig. 3.2 $T_{in} = T_{sat}$, $q = 1W/cm^2$). As the gas velocity increases, the liquid slugs decrease in length.

When the liquid slugs are short enough they collapse (Fig. 3.1 $T_{in} = T_{sat}$). The resulting pattern consisting of liquid flowing in the form of a film at the wall and gas flowing in the center is similar to annular flow. The gas core sometimes can break up and frothy slugs, containing many small bubbles, appear. This flow pattern, which is often called

frothy slug-annular flow (Zhao and Rezkallah, [86]), is a transition between slug flow and annular flow, which occurs at the highest superficial velocities of the gas. When the gas velocity is very high, the interface becomes wavy and some droplets can be entrained in the gas core. In this study, churn, or the pre-annular regime will be grouped with the slug flow regime in a regime called slug/churn. Annular flow will be considered where there is a clear continuous vapor core surrounded by a wavy liquid film. At the interface of the liquid film small ripples can be observed as well disturbance waves of large amplitude. The high shear by the gas flow at the crest of these disturbance waves is responsible for droplet entrainment. The annular flow with disturbance waves is visible in Fig 3.1 for $x = 0.2$ and in Fig. 3.2 for $x = 0.2$ and $q > 2\ W/cm^2$.

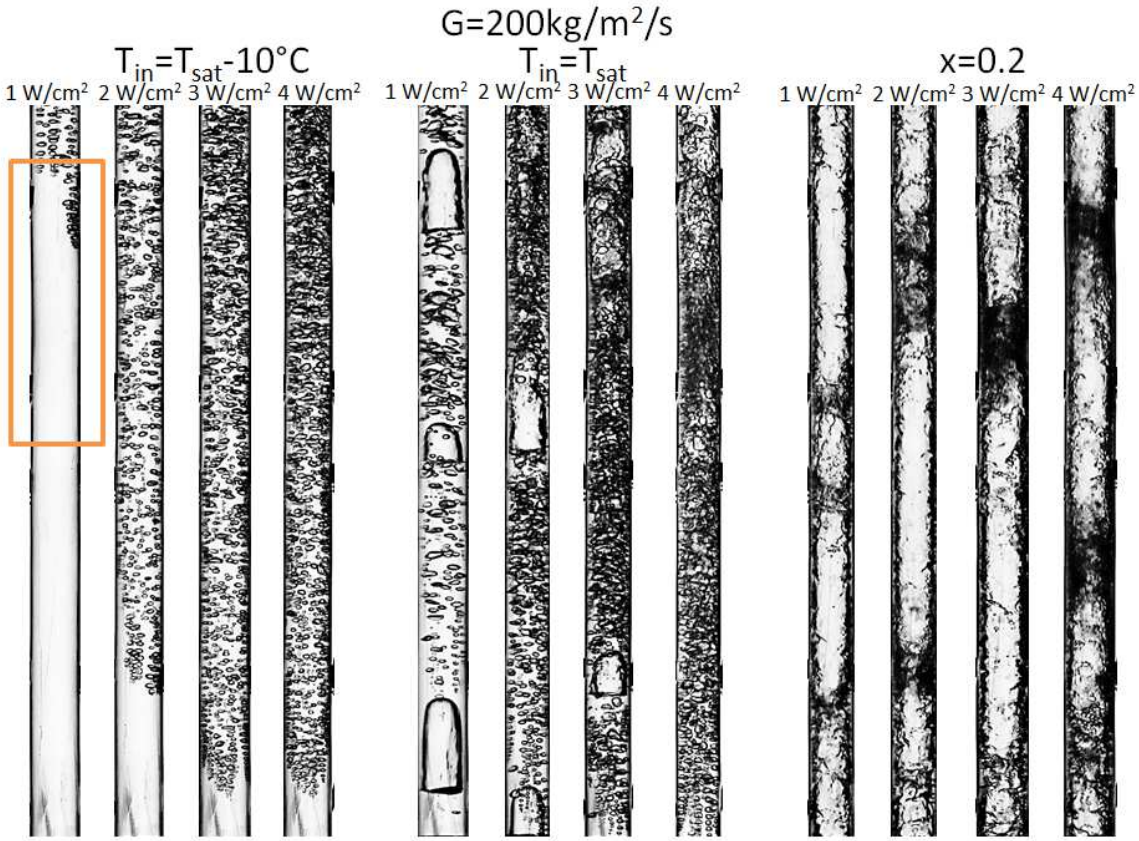

Figure 3.2: Flow regimes in normal gravity.

Flow visualizations performed in microgravity conditions are showed in Fig. 3.3 for $G = 50\ kg/m^2/s$ and $G = 200\ kg/m^2/s$. Less experimental parameters have been investigated in microgravity. A smaller length of the tube, 6.8 cm, was observed. It is located on the second half of the tube and displayed as a rectangle in Fig 3.1 and 3.2. Differences between microgravity and normal gravity conditions are clearly visible by comparing Fig. 3.1 and

3.2 (ground experiments) and Fig. 3.3 (experiments performed on board the aircraft).

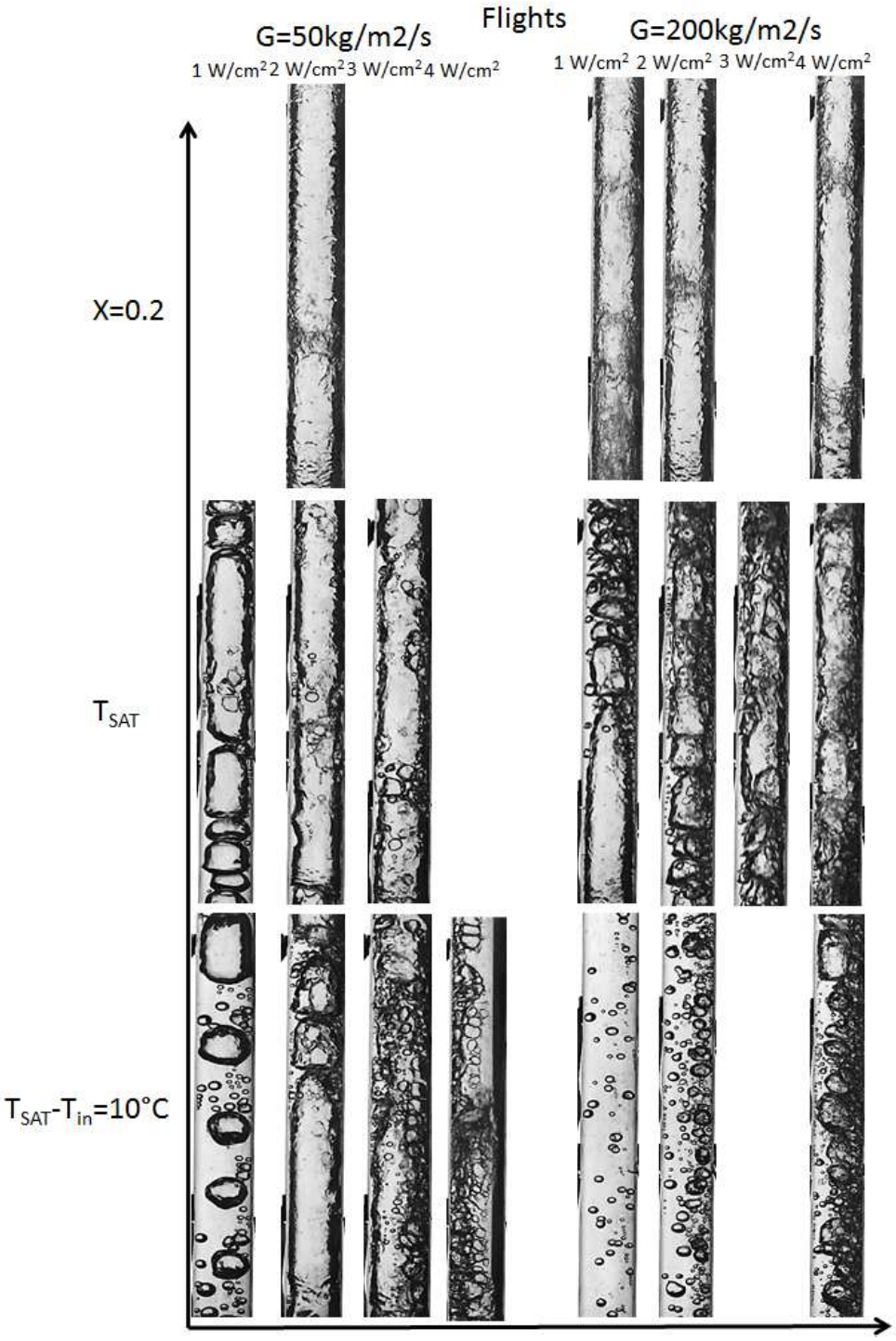

Figure 3.3: Flow regimes in microgravity.

In the case of bubbly flows, we can see the difference of bubble size between normal and microgravity. For low mass fluxes under microgravity conditions we can observe that the bubbles are larger than in normal gravity. It was observed by Ohta [66] that in normal gravity small bubbles generated from the wall and moved along the tube wall in the flow direction and grow, after a while they detach due to the buoyancy. In microgravity bubbles are moving at a reduced velocity and the size of the bubble is increased.

The larger bubble size in microgravity has been explained before as the result of a higher rate of coalescence due to the small relative motion of the bubbles and the larger diameter at detachment, since only the liquid drag is responsible for the detachment in microgravity [61].

At higher mass velocities the difference in the bubble size is less noted. Experiments were performed at mass fluxes up to $G = 200\ kg/m2/s$. For higher mass fluxes ($G = 400\ kg/m^2/s$) no significant difference was observed between normal and microgravity conditions [63]. The other flow patterns slug flow, transition slug/churn flow and annular flow are also observed in microgravity conditions. In the following we will consider 3 different flow regimes: bubbly flow with typical bubble sizes smaller than the tube diameter, annular flow with a continuous vapor core and liquid film at the wall and in between a slug flow regime including slug flow, churn flow and frothy slug-annular flow.

3.2 Flow pattern regime transitions

A flow pattern map, in function of the superficial gas and liquid velocities, is plotted in Fig. 3.4. The iso-lines of constant value of G and constant value of x are also plotted in this figure. The experiments were performed at constant mass flux, for three values $G = 50\ kg/m^2/s$, $G = 100\ kg/m^2/s$ and $G = 200\ kg/m^2/s$. The flow patterns are plotted for ground experiments and for microgravity experiments. No significant effect of gravity is visible on this map.

Let us now consider the prediction of the transition between the different flow patterns. Various models have been proposed to predict the transition from bubbly to slug flow in normal and microgravity conditions. In vertical upward flow Mishima and Ishii [60] propose that the transition between bubbly and slug flows occurs at a void fraction value equal to 0.3.

In microgravity conditions, transition criteria are defined using either a critical value of the void fraction (Dukler et al. [31], Colin et al. [23]), or a critical value of the Weber Number, We (Zhao and Rezkallah [86]). Transition from bubbly to slug flow is progressive and with the increase of coalescence, the size of the bubble increases along the tube. Coalescence is the basic mechanism responsible for the transition and it has been characterized by the Ohnesorge number, (Colin et al. [24]), $Oh = \nu_L\sqrt{\rho_L}/\sigma D$ based on liquid properties and the tube diameter D.

Two different regimes were identified, inhibiting coalescence regime ($Oh > 8.2 \times 10^{-4}$) and promoting coalescence ($Oh < 7.6 \times 10^{-4}$) regime. For cases of gas-liquid flows, a critical void fraction value of 0.45 was determined as the transition value due to coalescence where

the regime was inhibiting. For a promoting coalescence regime the transition occurred around $\alpha \approx 0.2$. In our experiments the Ohnesorge number is equal to 1.14×10^{-3}, which is characteristic of an inhibited coalescence regime in adiabatic flow.

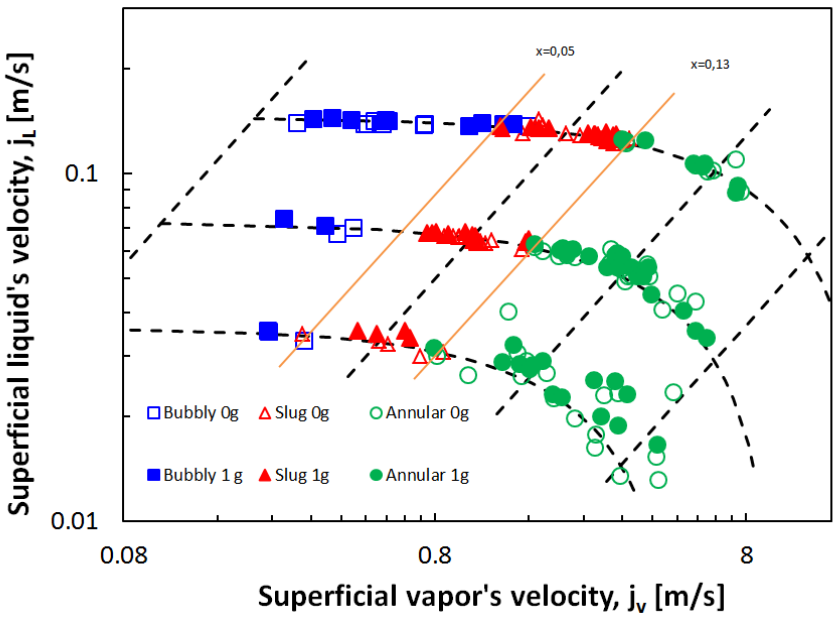

Figure 3.4: Flow pattern map for BRASIL's experimental data.

In our experiments, the transition from bubbly to slug flow appears for a quality value around 0.05. Considering that the gas velocity is well predicted by a drift-flux model in bubbly and slug flows (see section 3.3) :

$$U_G = j_v/\alpha = C_0(j_l + j_v) + U_\infty \tag{3.1}$$

It is possible to evaluate the void fraction at the transition. C_0 is taken equal to 1.2 and $U_\infty = 0$ in microgravity and $0.35\sqrt{gD}$ for slug flow in normal gravity. Thus the value of the void fraction at transition is close to 0.7, which is much higher than the value obtained in adiabatic air-water flow by Colin et al [24] or Mishima and Ishii [60]. This value is however in agreement with the value of $\alpha = 0.74$ found by Celata and Zummo [12] for the transition from bubbly to what they called intermittent flow. The origin of this particular value comes from sphere-packing theory according to Celata and Zummo [12]. When the void fraction of a bubbly flow exceeds the limit value, coalescence takes place for small bubbles and Taylor bubbles appear on the flow.

The transition from slug flow to annular flow is also observed in our experiments for a critical value of the quality close to 0.13 for both ground and microgravity conditions.

According to Dukler et al. [31] for microgravity flows the transition from slug to annular flow can be calculated by equaling the void fraction values in slug flow (3.1) and the void fraction calculated in annular flow:

$$\frac{\alpha^{5/2}}{(1-\alpha)^2} = \frac{f_i}{f_w}\frac{\rho_g}{\rho_l}\left(\frac{j_g}{j_L}\right)^2 \tag{3.2}$$

For $x = 0.13$ a void fraction value close to 0.8 is found. this value is similar to those found for adiabatic air-water flow by Dukler et al. [31].

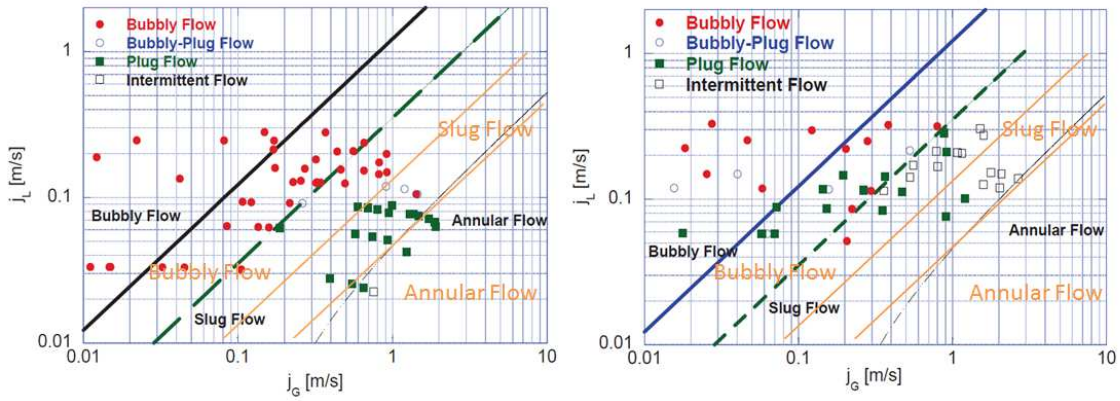

Figure 3.5: Flow pattern transitions compared with Celata and Zummo's map, to the left normal gravity conditions for a 4 mm tube and to the right microgravity conditions [12] for a 6 mm tube. The transition lines come from Dukler et al. [31].

We compared our experiment data to those of Celata and Zummo in Fig. 3.5. The orange lines in the figure are the transition lines corresponding to our experiments. In this flow pattern map, the transition lines of Dukler et al. [31] for air-water flows are also plotted in black and green. The transition from slug to annular flow is similar for flow boiling and adiabatic flow and occurs at $\alpha = 0.8$. In the experiments of Celata and Zummo, the transition from bubbly to plug flow in a 6 mm diameter tube occurs for $\alpha = 0.45$ (dashed green line) where as it occurs at $\alpha = 0.7$ in a 4mm diameter tube.

From this figure it can be seen that the transitions bubbly/slug and slug/annular do not occur for a constant value of a Weber number as proposed by Rezkallah.

A flow pattern map is also plotted in a (G, x) diagram given in Fig. 3.6. Transitions have also been characterized as a function of the vapor quality.

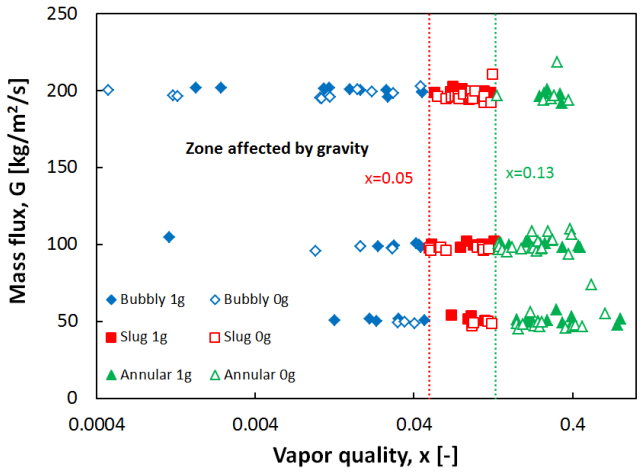

Figure 3.6: Flow patterns map Sapphire Tube.

3.3 Void fraction and film thickness

3.3.1 Void Fraction

Void fraction was measured with capacitance probes for the sapphire test section at the inlet and at the outlet. The inlet measurements were mostly used to monitor single-phase flow conditions for subcooled and saturated cases. The outlet measurements are presented in this section.

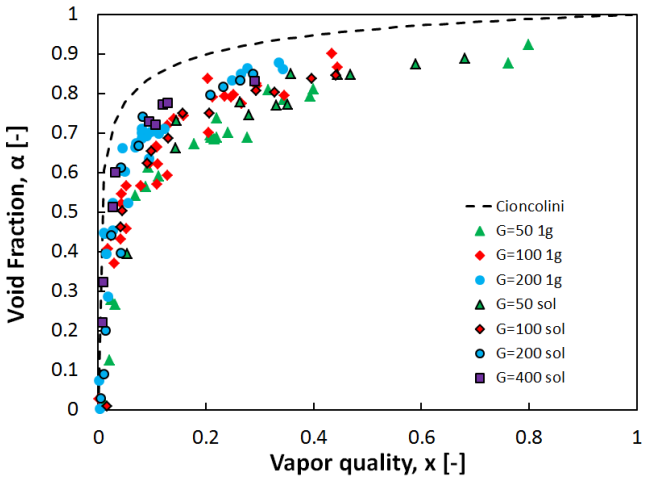

Figure 3.7: Influence of G (Normal gravity data from flight campaigns and ground measurements).

As explained in Chapter 2, modifications were made to the old design used for the capacitance probes so coherence in normal gravity measurements was expected. In Fig 3.7, void fraction in normal gravity periods during the parabolic flights are compared to the data obtained for ground measurements. As we can see the data agree for each mass flow rate and will be therefore analyzed and grouped as the normal gravity data since the same evolution as a function of the mass flux was observed.

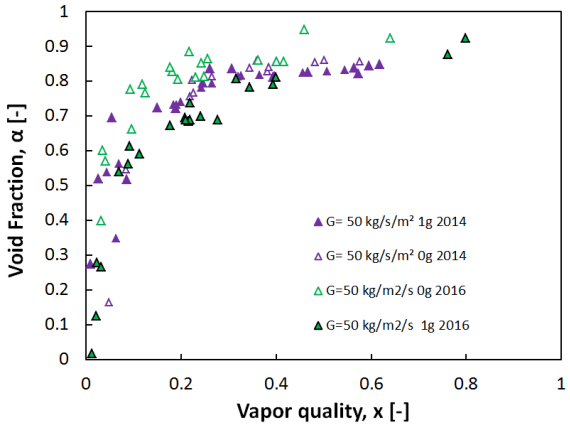

Figure 3.8: Comparison of 2014 and 2016 data (Normal and microgravity).

In Fig 3.8, void fraction data from Narcy [64], which were obtained with the same experimental set-up, are presented and compared to the data obtained during parabolic flights and on ground during this work (2016). A comparison was made to identify improvements or differences. Here, values of void fraction are more sensitive to gravity changes. What we could observe was that for low mass fluxes we could see the difference in void fraction measurements contrary to the old probes that were not sensible enough.

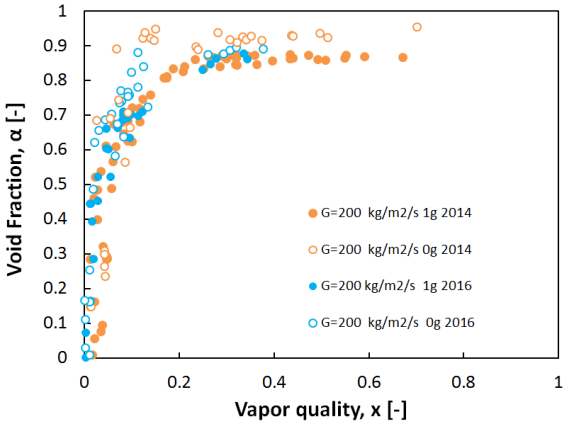

Figure 3.9: Comparison of 2014 and 2016 data (normal and microgravity).

In Fig. 3.9, the two sets of data obtained in 2014 and 2016 are in good agreement. More dispersion in the measurements of 2014 is observed.

Correlations based on the drift-flux model exist to compare experimental results of churn and annular flows. The results obtained for the void fraction were plotted and compared to previous correlations and two other models Ishii [43] and Zuber et al. [90] model. In this models the contributions parameters, C_0 and U_∞ are given by the following expressions:

- For Ishii's model for churn flow:

$$C_0 = 1.2 - 0.2\sqrt{\frac{\rho_v}{\rho_l}}, \quad U_\infty = \sqrt{2}\left(\frac{\sigma g\left(\rho_l - \rho_v\right)}{\rho_l^2}\right)^{0.25} \tag{3.3}$$

- For Zuber et al. model for annular flow

$$C_0 = 1.0, \quad U_\infty = 23\sqrt{\frac{\mu_l j_l}{\rho_v D}}\left(\frac{\rho_l - \rho_v}{\rho_l}\right) \tag{3.4}$$

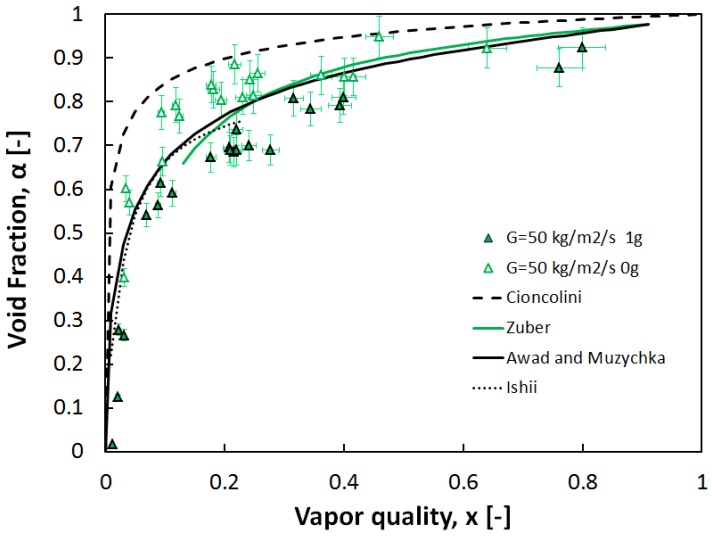

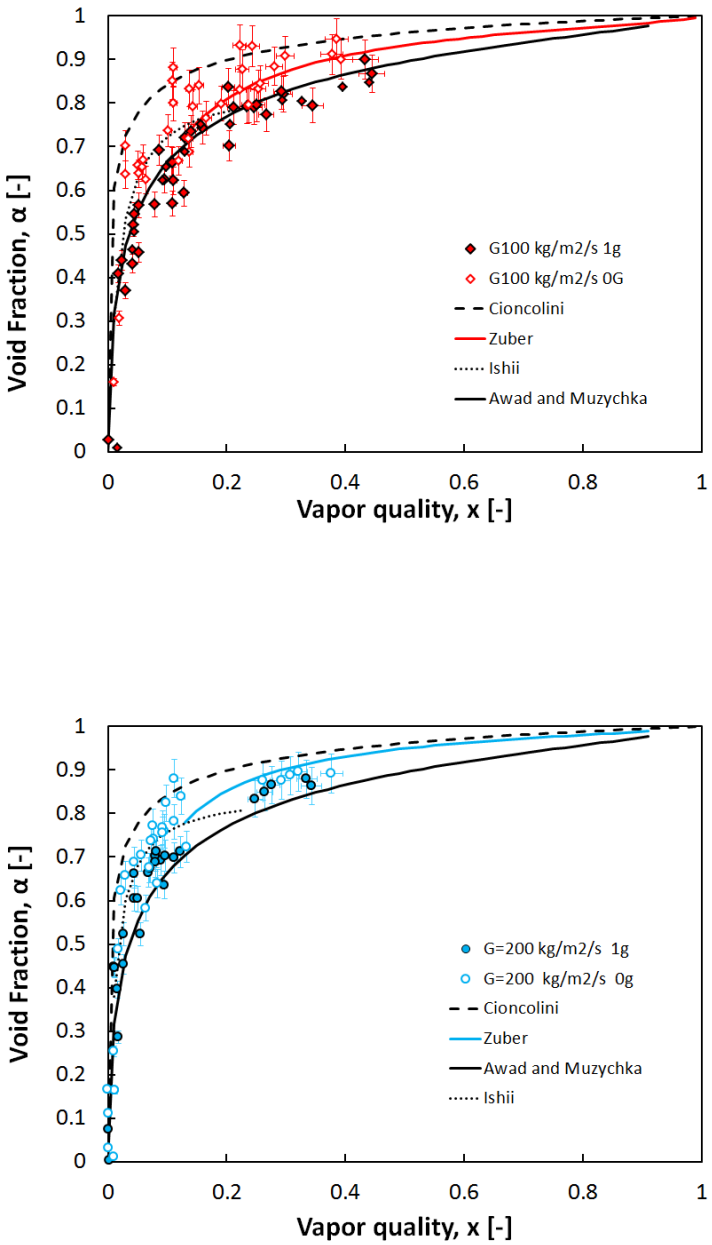

Figure 3.10: Comparison of each data set from $G = 50\ kg/m^2/s$, $G = 100\ kg/m^2/s$ and $G = 200\ kg/m^2/s$ with different correlations that predict void fraction.

In Fig. 3.10 the void is plotted versus the vapor quality, in normal and microgravity, and is compared to correlations that predict void fraction for two-phase flows. Cioncolini and Thome's correlation (Eq. 1.38) is independent of mass flux or gravity level and tends to overestimate the value of void fraction for normal gravity experiments but for microgravity data it seems to have a better agreement specially for saturated data. Zuber's correlation appears to be in a better agreement as shown in both Fig. 3.10 and in Fig. 3.11c,

this correlation can only be applied to annular flows. Ishii's correlation that can only be compared to bubbly and slug flow, can predict closely void fraction for normal gravity but for lower mass fluxes, where the influence of gravity is higher, shows less accuracy. The measurements are also compared to the correlations of Awad and Muzychka (Eq. 1.37).

A quantitative comparison of the experimental data and the prediction of the different models and correlations is displayed in Fig. 3.11 and table 3.1. Also in Fig. 3.11e is plotted the prediction of the drift-flux model (Eq. 1.25).

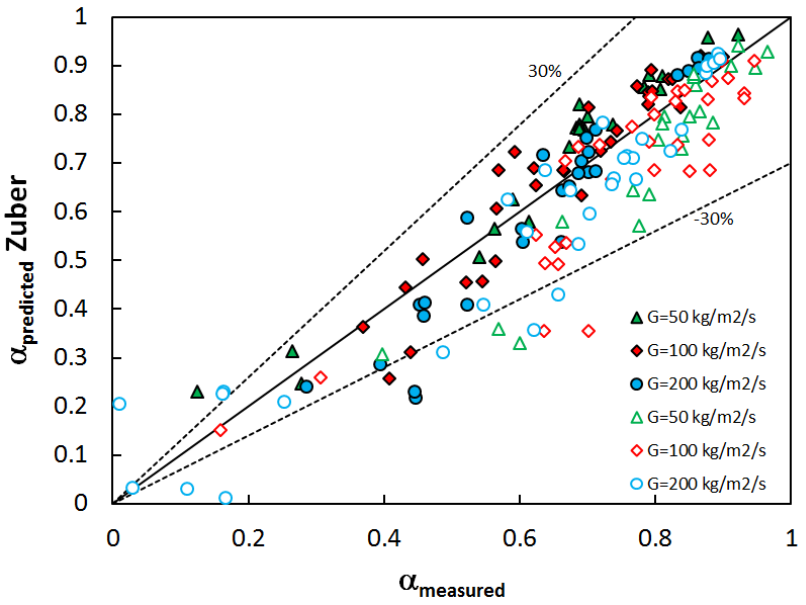

(a) α predicted by Zuber's correlation.

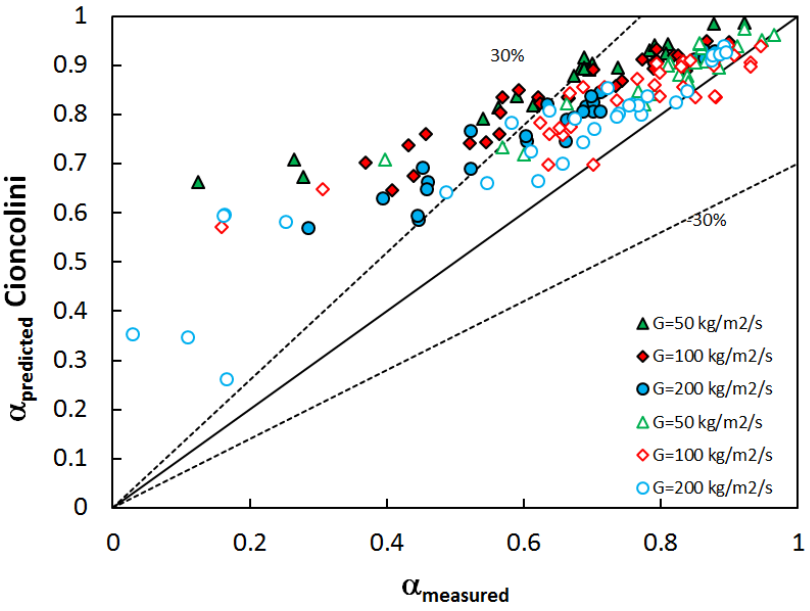

(b) α predicted by Cioncolini and Thome's correlation.

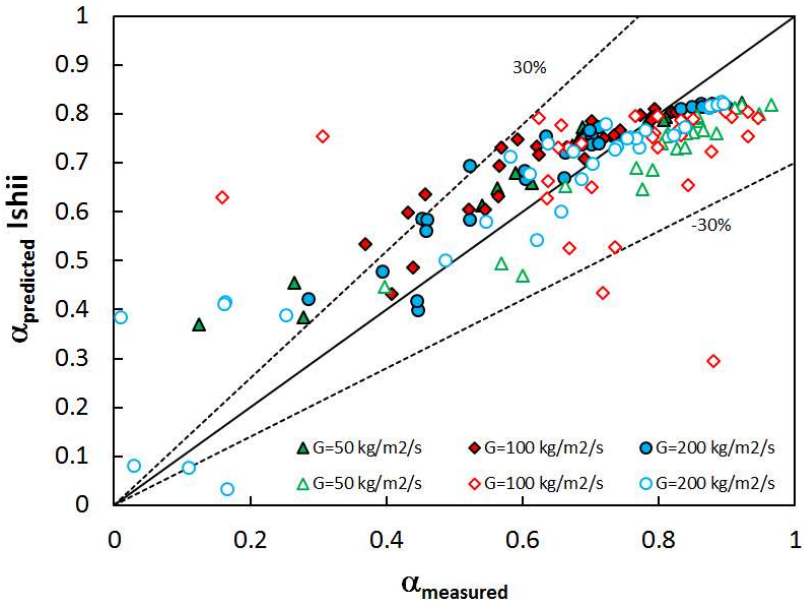

(c) α predicted by Ishii's correlation.

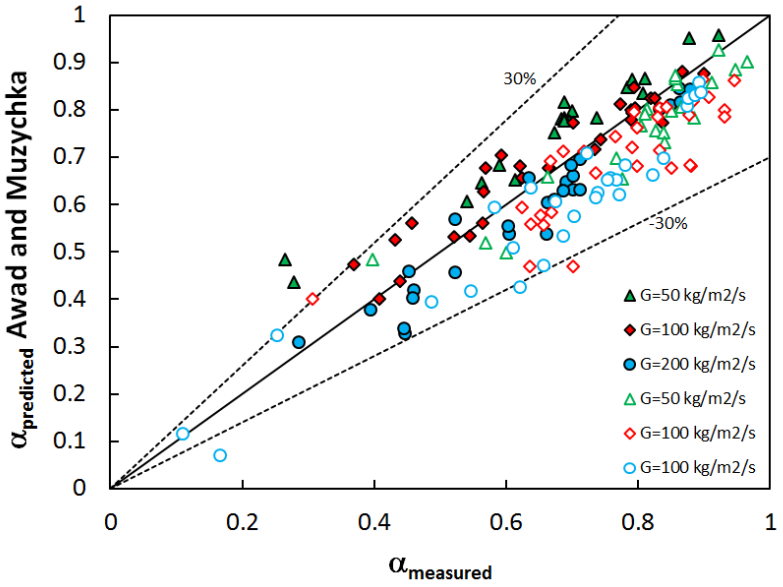

(d) α predicted by Awad and Muzychka's correlation.

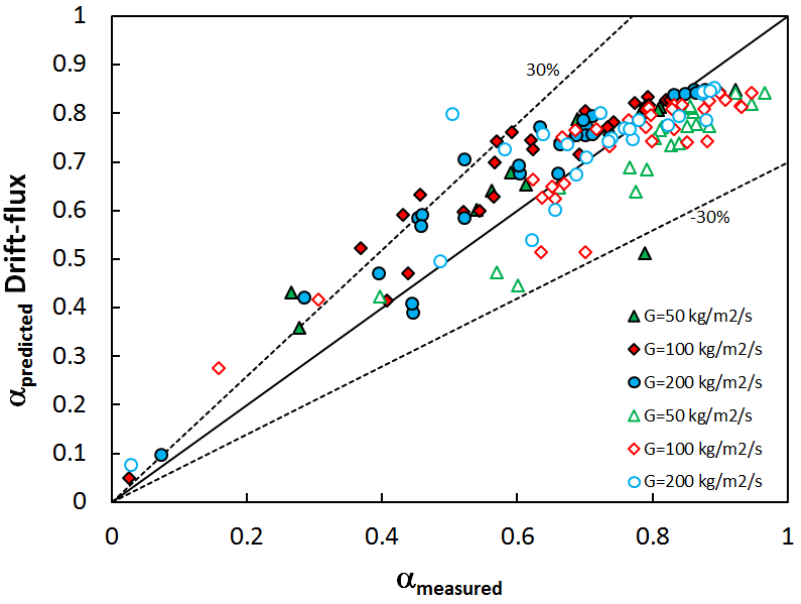

(e) α predicted by the Drift-flux model.

Figure 3.11: α predicted by Zuber, Cioncolini, Ishii, Awad and Muzychka and the Drift-flux model.

In addition for a quantitative comparison of the data with the correlations, the mean relative error and the mean absolute error were calculated as followed:

$$\text{MRE} = \frac{1}{n}\sum_{i=n}^{n}\frac{\alpha_{predicted} - \alpha_{measured}}{\alpha_{measured}} \tag{3.5}$$

and

$$\text{MAE} = \frac{1}{n}\sum_{i=n}^{n}\frac{|\alpha_{predicted} - \alpha_{measured}|}{\alpha_{measured}} \tag{3.6}$$

	1g		0g	
	MRE %	MAE %	MRE %	MAE %
Awad and Muzychka [7]	6.1	23.28	-9.2	11.8
Cioncolini and Thome [21]	35.5	35.5	37.3	37.6
Ishii [43]	11.7	14.1	1.9	17.4
Zuber [89]	1.4	11.1	-10.0	13.7
Drift-flux model	11.11	13.32	-0.58	10.9

Table 3.1: Mean relative and mean absolute error for microgravity and normal gravity data.

From this table we can observe that Zuber's model has a better capability of predicting void fraction values for this experiment. Even at low mass fluxes the accuracy of predicting the values obtained is good. The drift-flux model and Awad and Muzychka model also give a reasonable prediction of the void fraction.

3.3.2 Mean gas velocity in bubbly and slug flows

In bubbly and slug flow, the void fraction can be used to calculate the mean gas velocity and compare it to the drift-flux model (Zuber and Findlay [89]) in both normal and microgravity conditions (Eq. 1.22 and 1.24).

In Fig. 3.12 the actual gas velocity is plotted versus the mixture velocity and it is compared to the drift-model for normal and microgravity, which shows a good agreement between the measurements and the prediction of this model.

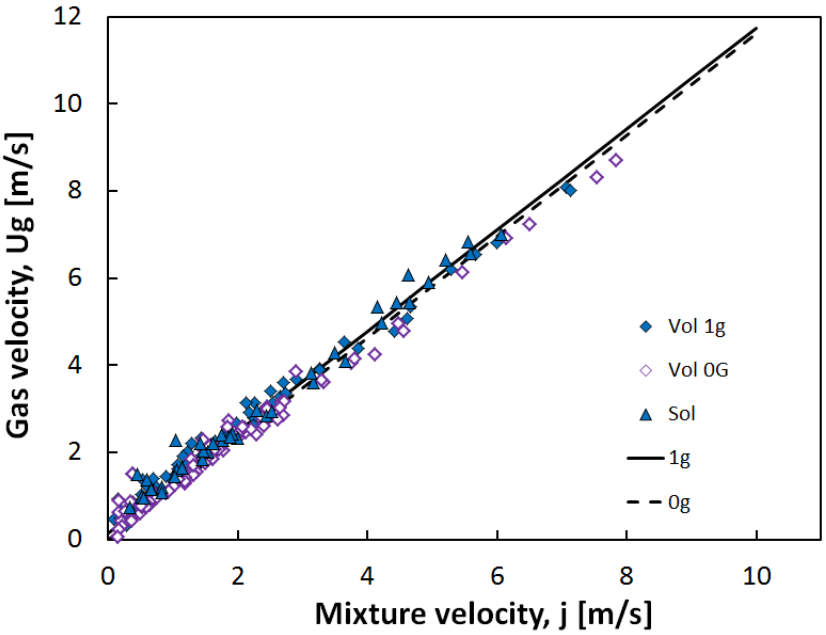

Figure 3.12: Gas velocity versus mixture velocity.

3.3.3 Film thickness

Film thickness was calculated, for every run in annular flow, from the expression:

$$\delta = \frac{D}{2}\left(1 - \sqrt{\alpha\left(1 + \frac{\rho_v}{\rho_l}\frac{1-x}{x}\ e\right)}\right) \tag{3.7}$$

where δ is the film thickness deduced from geometrical considerations and where e represents the entrainment of droplets in the vapor core in annular case that has been calculated by Eq. 1.43 and 1.45.

The model developed by Cioncolini and Thome, discussed in Chapter 1, to calculate the entrainment estimates that the value of e increases since it is based on a Weber number that uses the superficial vapor velocity and at higher mass fluxes and higher vapor qualities, the value is higher. In this study the highest mass flux was $G = 200\ kg/m^2/s$ at a $x < 0.4$ where the factor e of the Eq. 1.43 is not higher than 5%.

Comparing the latest data base with Cioncolini and Thome's correlation [21], we can point out that at low mass fluxes the values obtained experimentally are above the correlation's prediction, especially for normal gravity. On the other hand, for higher mass fluxes, the agreement with Cioncolini's correlation is reasonable for microgravity conditions.

The evolution of the film thickness for annular flows is presented in Fig. 3.13 for the

different values of G, $G = 50\ kg/m^2/s$, $G = 100\ kg/m^2/s$ and $G = 200\ kg/m^2/s$. Film thickness decreases with the vapor quality due to a higher value of the void fraction. In $1g$, the film thickness is larger than in $0g$ conditions.

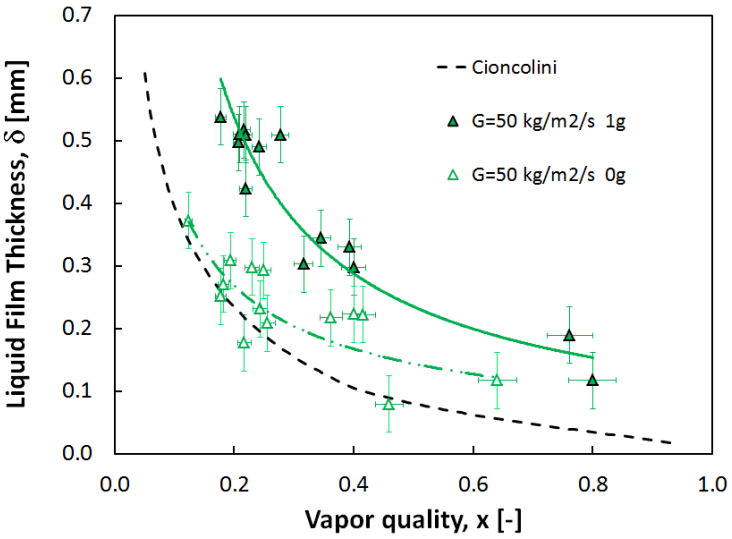

(a) Film thickness for experiments at $G = 50\ kg/m^2/s$.

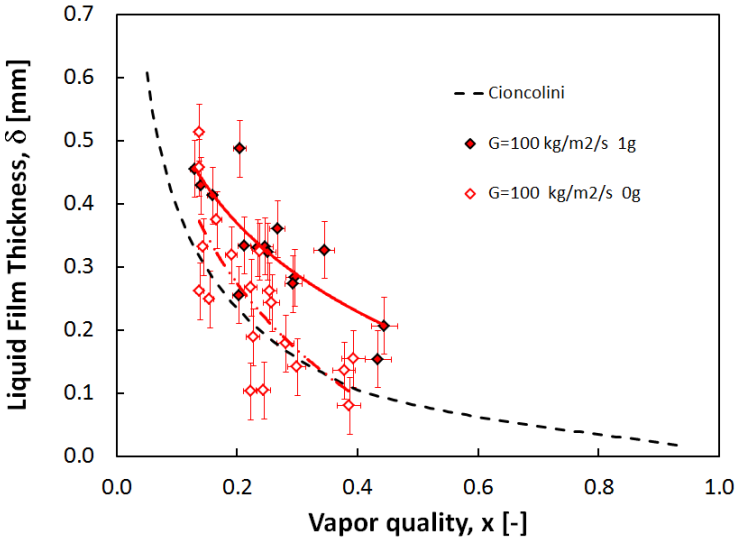

(b) Film thickness for experiments at $G = 100\ kg/m^2/s$.

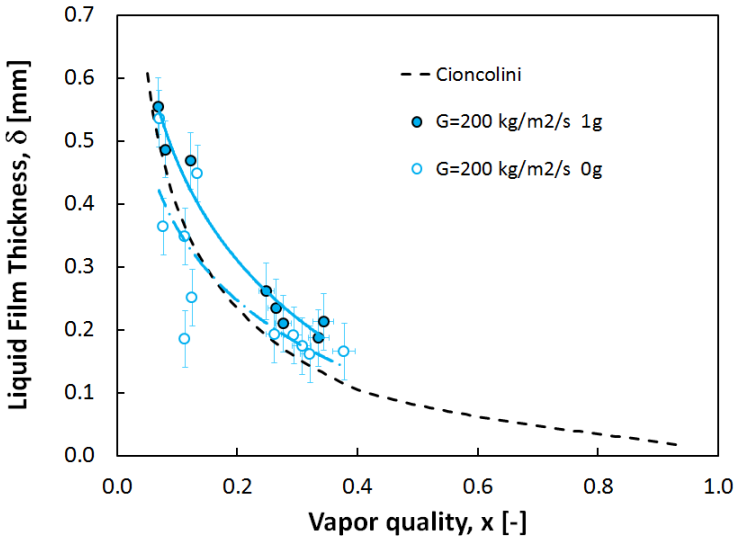

(c) Film thickness for experiments at $G = 200\ kg/m^2/s$.

Figure 3.13: Film thickness for annular cases.

It also decreases as the mass flux increases. This is due to an increase of the interfacial shear stress with the mass flow rate, [61]. The difference in the film thickness between 1g and 0g decreases with the mass flux, due to the dominant effect of inertia, compared to buoyancy.

3.4 Heat Transfer Coefficient

This section will present the experimental results obtained with the two test sections described in Chapter 2. On both test sections local measurements of the outer wall temperature were made.

Experiments were performed with the 2 sections on ground and in 2 parabolic flight campaign. The 2 sets of results for each test section will be first presented to point out the effect of the mass flux, quality, gravity and if any the effect of the wall heat flux on the heat transfer coefficient. The measurements obtained with the 2 test sections are compared with each other to show the agreement between the measurement techniques. The *HTC* are also compared to classical correlations of the literature. Finally the effect of buoyancy on the *HTC* is discussed.

3.4.1 Sapphire tube's HTC

For the sapphire tube, local measurements were made in 4 different positions, as explained in Chapter 2, along the tube on both sides of the tube. As previously mentioned, all values

are calculated at the distance of each of the 4 different probes. Heat transfer coefficients are plotted versus the vapor quality for different mass fluxes and wall heat fluxes.

Results are presented in different groups, difference were found for subcooled or saturated conditions at the entrance of the tube. Since different boiling mechanisms affect at different stages, remarks are made all along the analysis. As seen and explained for other parameters, influence of the mass flux and gravity are observed and discussed and some correlations are presented to compared them with the data obtained.

On ground and microgravity conditions experiments are performed at $G = 50$, $G = 100$ and $G = 200\ kg/m^2/s$, corresponding to mass flux ranges where gravity is expected to have an influence. Wall heat fluxes varied from 0.5 to 4 W/m^2. The inlet conditions of the test section were either subcooled liquid or saturated conditions with qualities up to $x = 0.2$.

Influence of mass flux

Data corresponding to inlet subcooled or saturated conditions are presented in this first data set. The data is plotted separately, 3.14a and 3.14b and in one same figure in Fig 3.14c. In both cases we find the influence of the mass flux G with the evolution of the vapor quality x.

The big dispersion observed for data at higher mass fluxes is due to measurement techniques. Since at $G = 200\ kg/m^2/s$ the difference between the wall temperature and the liquid temperature is so small the error made on the measurements increases drastically resulting in low accuracy for the calculation of HTC.

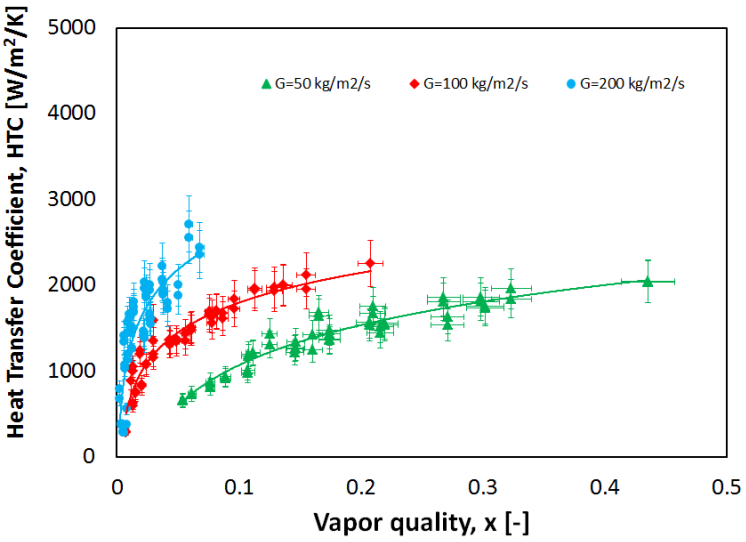

(a) HTC for Subcooled data

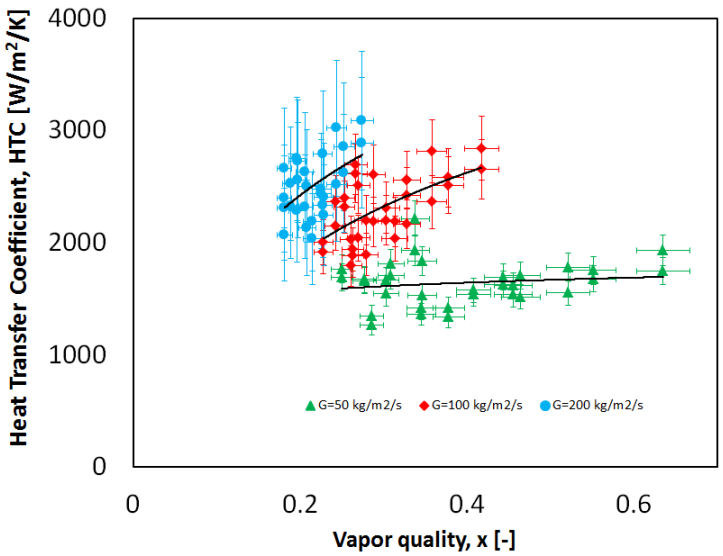

(b) HTC for saturated data

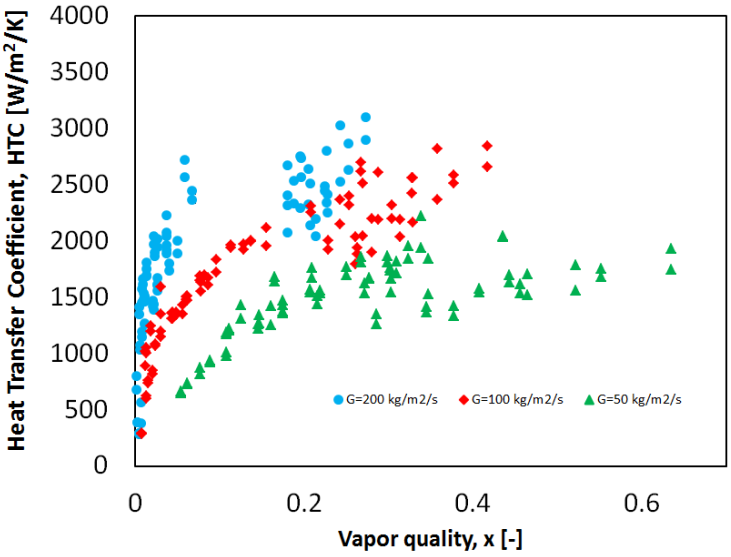

(c) HTC for all data

Figure 3.14: HTC for Sapphire tube $G = 50\ kg/m^2/s$, $G = 100\ kg/m^2/s$ and $G = 200\ kg/m^2/s$

Mass flux was noticed to be the factor that affected HTC the most. Fig. 3.14 shows the trends found for normal gravity data for different values of mass flow rates. The same evolution was found for microgravity data.

Influence of wall heat flux

To analyze the influence of wall heat flux, precision on the measurements of wall temperature was taken into account. For increasing values of heat flux we can see increasing values of heat transfer coefficient both in microgravity and normal gravity and also in subcooled and saturated conditions.

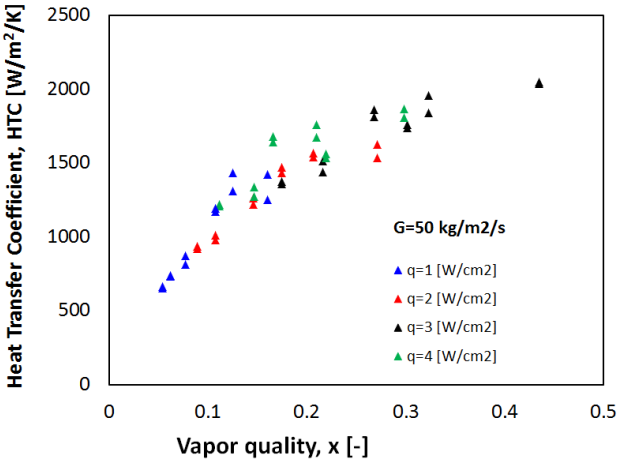

(a) $G = 50\ kg/m^2/s$ for all heat fluxes.

At low mass fluxes, $G = 50\ kg/m^2/s$ and $G = 100\ kg/m^2/s$, the effect of the heat flux is mainly visible on the increase of the quality. At constant quality value, HTC is not sensitive to the heat flux. The effect of the heat flux on the HTC is visible at $G = 200\ kg/m^2/s$ at low qualities corresponding to the subcooled nucleate boiling regime.

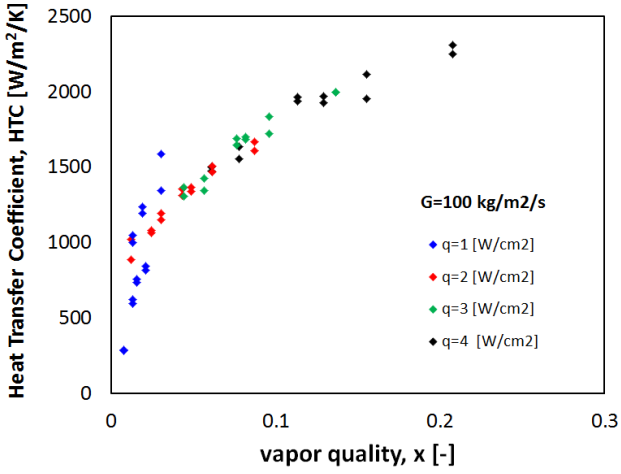

(b) $G = 100\ kg/m^2/s$ for all heat fluxes.

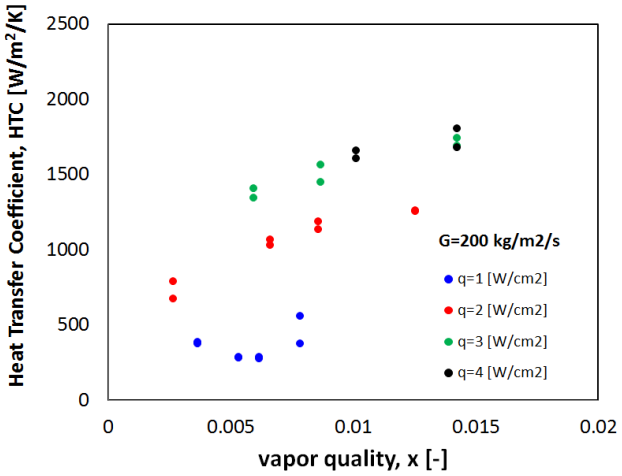

(c) $G = 200\ kg/m^2/s$ for all heat fluxes.

Figure 3.15: HTC for Sapphire tube subcooled data and the evolution depending on the heat flux.

In Fig. 3.2 for $T_{in} = T_{sat} - 10°C$, we can see that the density of the bubbles nucleating on the wall increases with the heat flux leading to an enhancement of the heat transfer coefficient. This is also coherent with the results of Narcy et al. [61] and Ohta and Baba [67].

Influence of gravity

Another parameter observed to affect the HTC was gravity. However, it is difficult to reproduce exactly the same experimental conditions (pressure, saturation temperature, etc...) on ground in parabolic flights. This is the reason why, we will compared the data obtained during the parabolic flights in 1g and 0g phases.

It was observed, as seen on Fig. 3.16, a deterioration on the heat transfer coefficient during the measurements in microgravity. This set of data was obtained during the parabolic flight campaign performed in March 2016.

In the Fig. 3.16, the filled symbols represent the normal gravity periods, during horizontal flight, and the empty symbols the microgravity measurements. The effect of gravity is significantly higher for low mass fluxes, at $G = 50\ kg/m^2/s$, and we can see a smaller difference at higher mass fluxes, $G = 200\ kg/m^2/s$. The same trends were already observed by Narcy et al. [63]

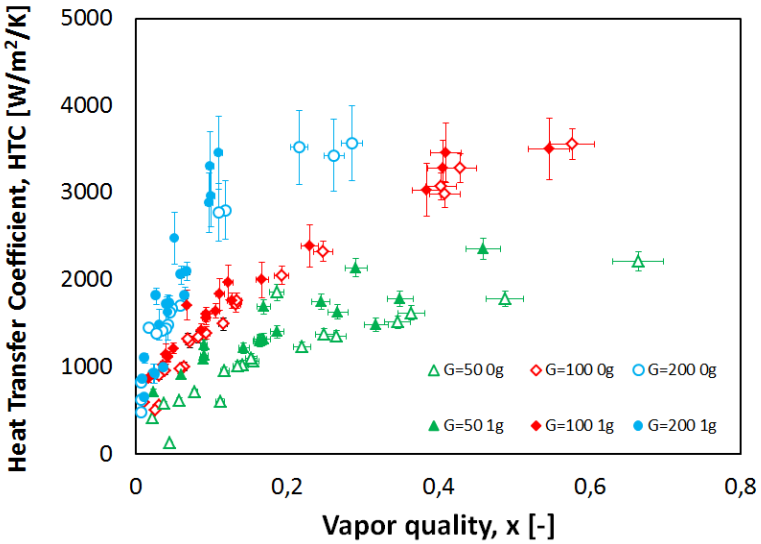

Figure 3.16: HTC for Sapphire tube $G = 50\ kg/m^2/s$, $G = 100\ kg/m^2/s$ and $G = 200\ kg/m^2/s$ in 1g (closed symbols) and 0g (open symbols) periods during parabolic flights.

Comparison to the literature

Correlations presented in Chapter 1 have been compared to the data set obtained for the sapphire tube in Fig. 3.17.

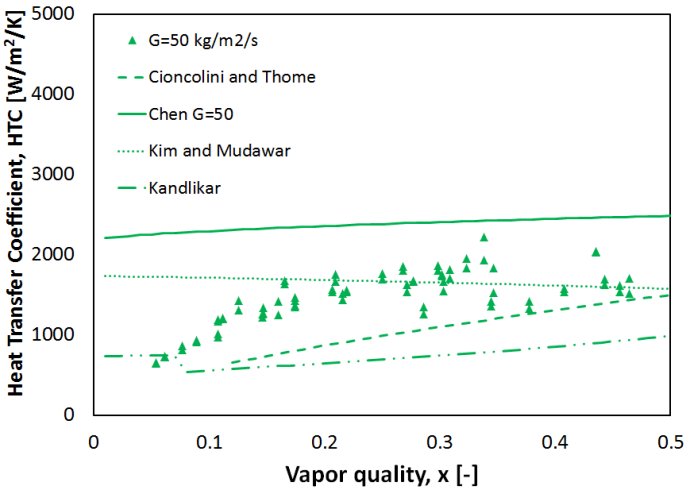

(a) HTC for Sapphire tube compared to experimental correlations at $G = 50\ kg/m^2/s$.

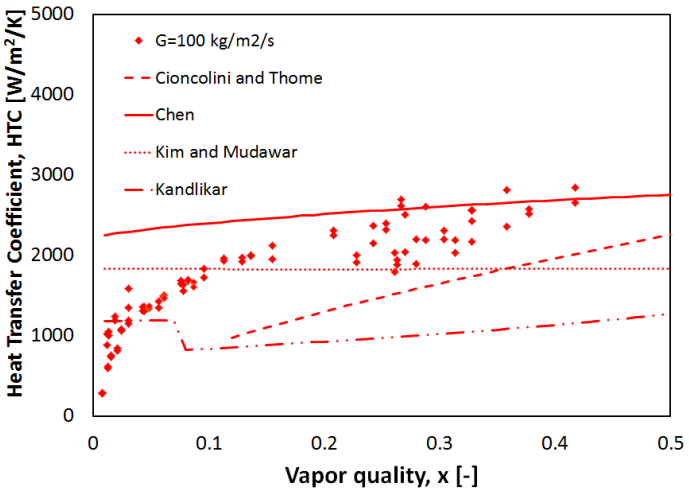

(b) HTC for Sapphire tube compared to experimental correlations at $G = 100\ kg/m^2/s$.

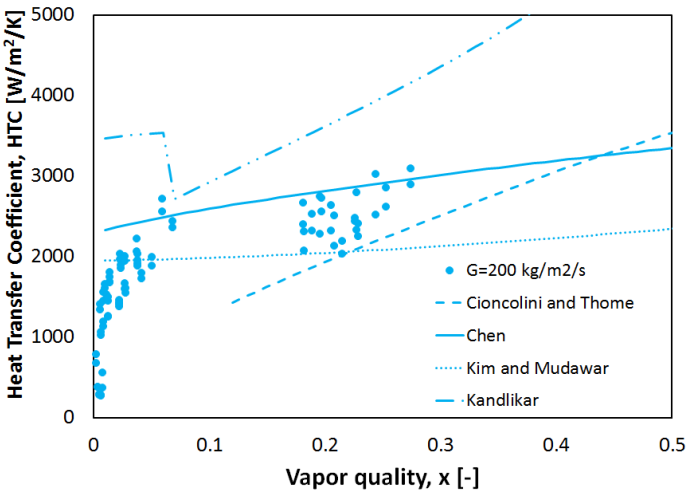

(c) HTC for Sapphire tube compared to experimental correlations at $G = 200\ kg/m^2/s$.

Figure 3.17: HTC for Sapphire tube compared to experimental correlations.

Cioncolini and Thome's correlation, appeared to predict the trends of the results obtained by BRASIL. Kim and Mudawar for the most cases, especially for the subcooled data set, although it under predicts some of the values, at lower heat transfer rates seems to work better. On the other hand Chen's correlation, a classical correlation that takes into account nucleate and convective boiling, over predicts for most of the cases specially the subcooled data measured by BRASIL. Unfortunately Chen's correlation depends on the difference

between the wall temperature and the liquid temperature, since this difference is so small, we do not seem to have enough precision to calculate HTC and the error made for this correlation increases rapidly.

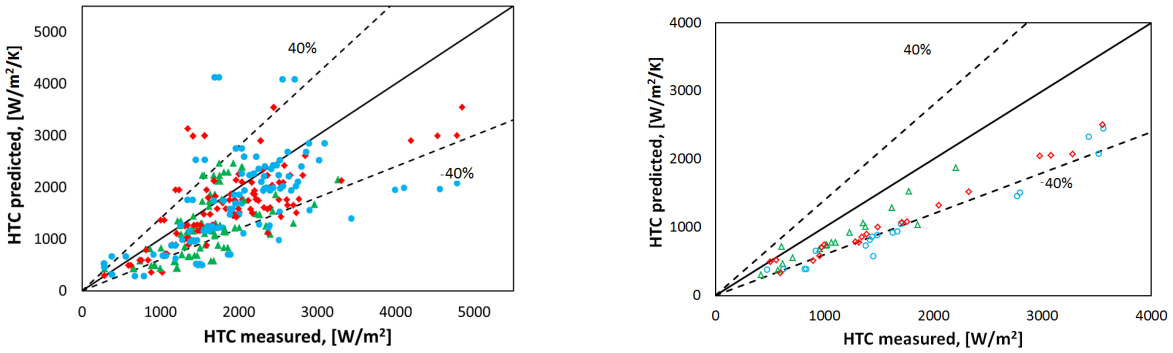

(a) Cioncolini and Thome.

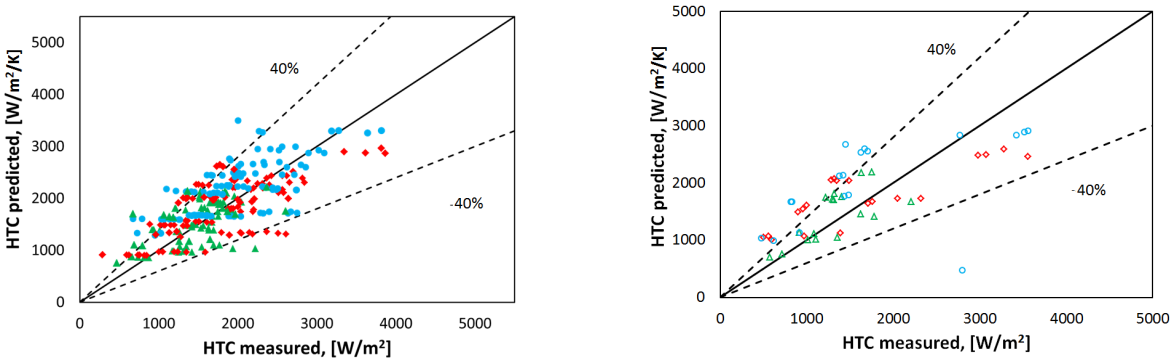

(b) Kim and Mudawar.

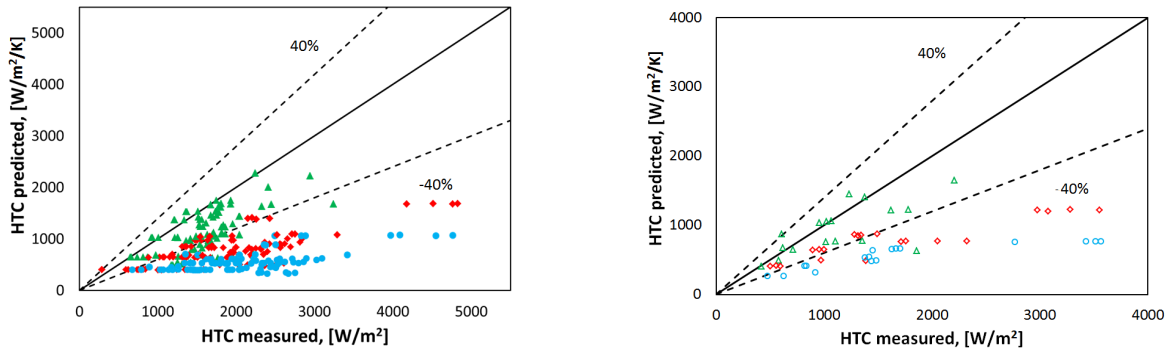

(c) Kandlikar.

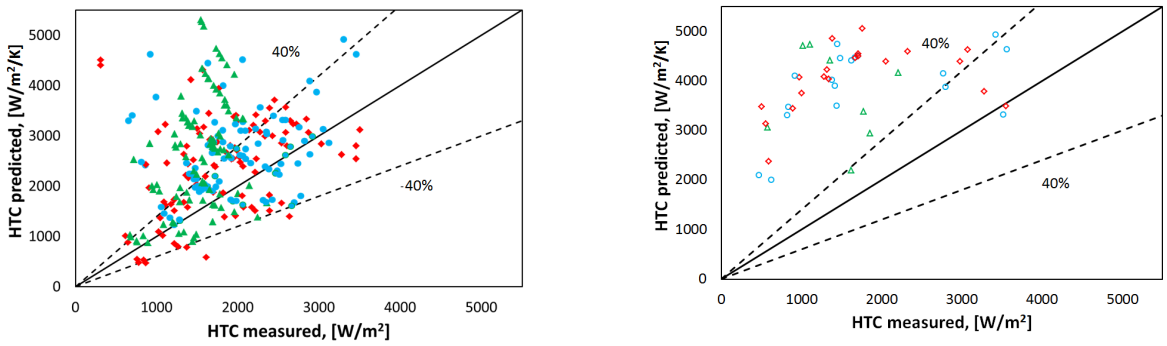

(d) Chen.

Figure 3.18: Correlations predicting HTC by different models compared to results obtained with BRASIL. On the left side is presented the results obtained from the ground measurements and normal gravity periods during parabolic flights and and on the right side the results obtained during the microgravity.

These correlations, although they are compared to all the results obtained by BRASIL, are conceived for saturated boiling. Chen, Kim and Mudawar and Kandlikar involve both convective boiling and nucleate boiling heat transfer. Cioncolini on the other hand only considers the evaporation through the turbulent liquid film in annular flows.

	1g		0g	
	MRE %	MAE %	MRE %	MAE %
Chen [15]	45.56	61.72	-1.0	19.0
Kandlikar [47]	3.43	54.99	37.3	37.6
Kim and Mudawar [50]	5.53	24.62	1.9	17.4
Cioncolini and Thome [20]	1.3	11.1	-10.0	13.7

Table 3.2: Mean relative and mean absolute error for microgravity and normal gravity data

3.4.2 Silicon tube's HTC

For the silicon tube as explain in Chapter 2 the heat transfer coefficient was obtained with the local measurement of the temperature thanks to the infrared thermography technique, all along the tube. The comparison with correlations previously discussed was made. The influence of G is also found and very noticeable at every experiment as shown in Fig. 3.19 for ground experiments.

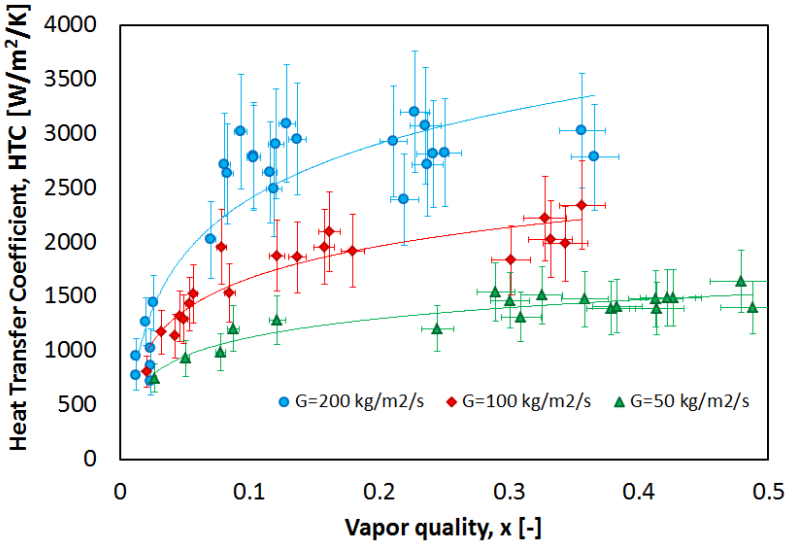

Figure 3.19: HTC calculated for the silicon tube for normal gravity conditions and trends for the three mass fluxes studied.

Fig. 3.21 shows the values of the HTC obtained for the three mass fluxes in 1g (closed symbols) and microgravity conditions (open symbols). Experiments were performed with wall heat fluxes from $q = 0.5\ W/cm^2$ to $3\ W/cm^2$.

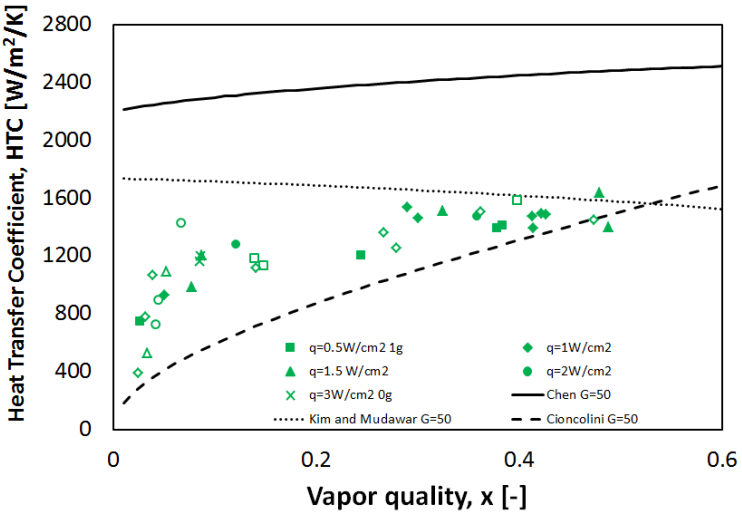

(a) HTC for the Silicon tube $G = 50\ kg/m^2/s$.

The influence of the wall heat flux on the heat transfer coefficient is not clearly visible on these figures. The effect of the gravity is only visible for $G = 200\ kg/m^2/s$, but it is

difficult to conclude since the accuracy of the measurements for this mass flux is not very good as it can be seen on the dispersion of the results.

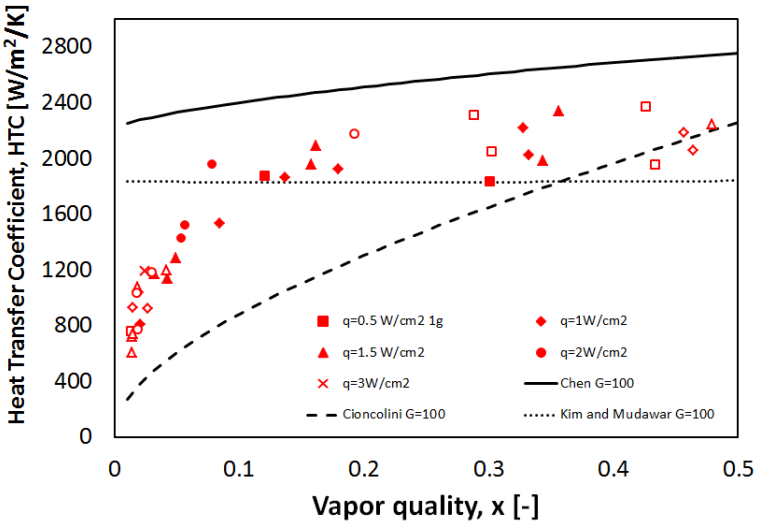

(b) HTC for the Silicon tube $G = 100\ kg/m^2/s$.

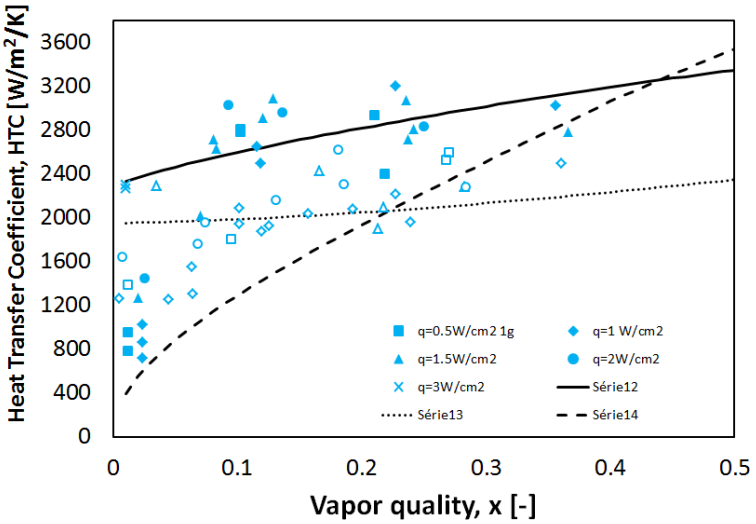

(a) HTC for the Silicon tube $G = 200\ kg/m^2/s$.

Figure 3.21: HTC for saturated and subcooled data at $G = 50\ kg/m^2/s$, $G = 100\ kg/m^2/s$ and $G = 200\ kg/m^2/s$ for normal and microgravity.

3.4.3 Sapphire tube data and Silicon tube data

The most interesting part of these experiments has been no doubly the fact that changing the tube and using different techniques to measure the same parameters of a phenomenon, the data seems to be in agreements with each other.

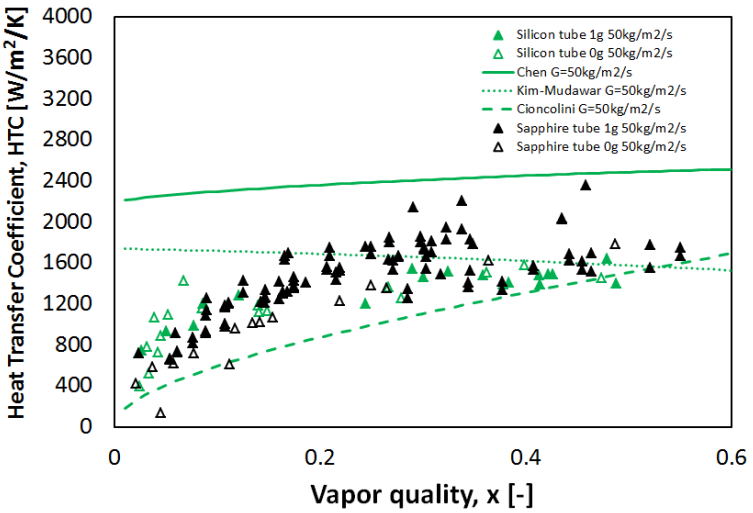

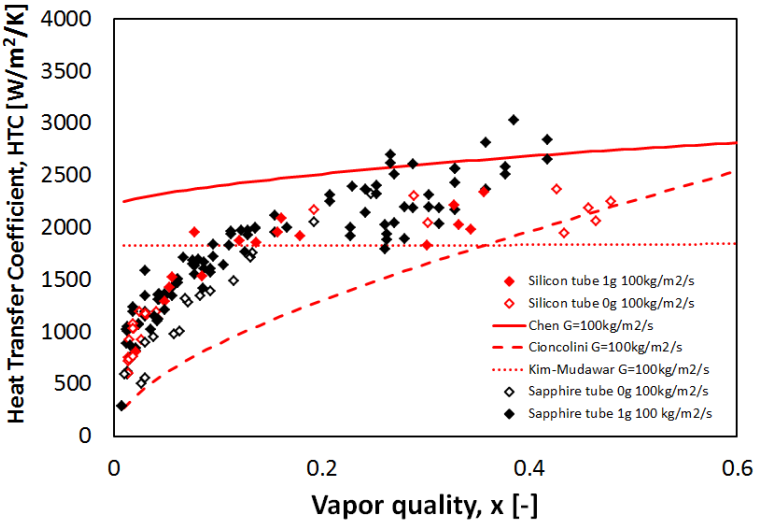

Something that we can highlight after performing these experiments is the need to continue studying flow boiling at a nucleate boiling regime, at subcooled conditions and at low vapor qualities. From the experiments with the silicon tube it is not obvious to point out the effect of gravity on the heat transfer coefficient.

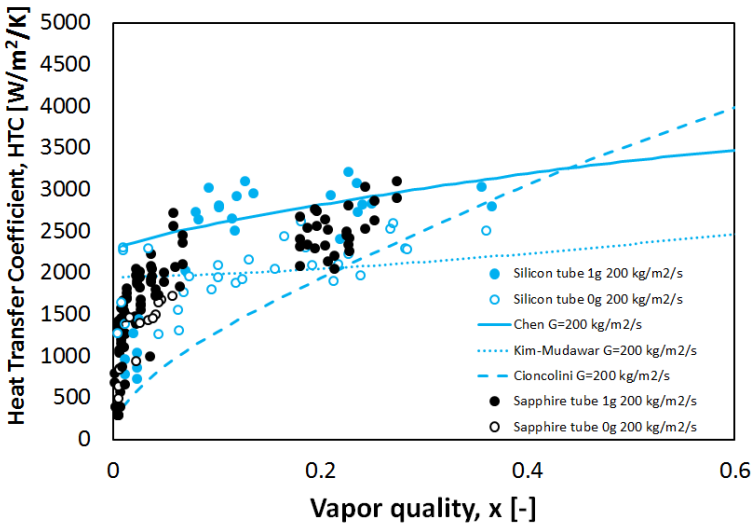

Figure 3.22: Comparison between Silicon and Sapphire tube data in normal and microgravity.

Influence of gravity on HTC: Sapphire

In order to clearly point out the effect of gravity on HTC, comparison of experiments performed with the same tube in the same conditions of temperature and pressure in 1g and 0g are compared. This is the case of the results presented in Fig. 3.23.

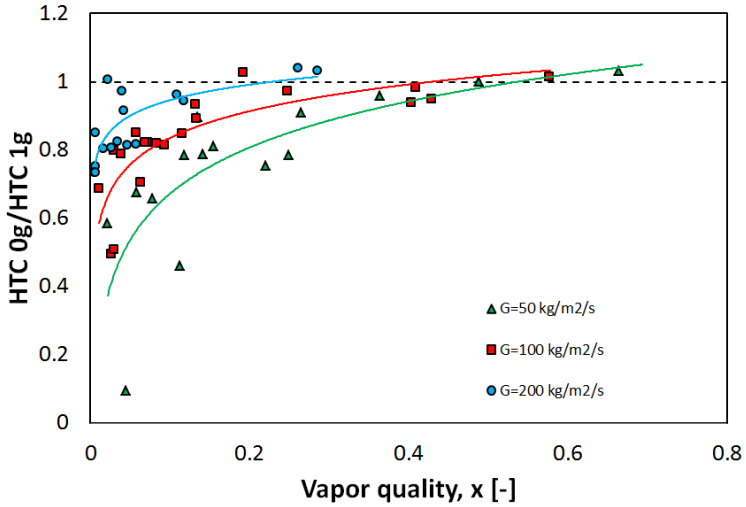

Figure 3.23: Ratio of HTC in normal and microgravity.

The ratio of the HTC in 0g and in 1g is plotted in Fig. 3.23. The lower the mass flux, the

greater the decrease of the HTC in 0g is observed. For $G = 200kg/m^2/s$, the decrease in the HTC in 0g is mainly observed in the nucleate boiling regime, for qualities smaller that 0.1. At $G = 50kg/m^2/s$, the decrease in the HTC in 0g is observed also in annular flow for quality up to 0.5.

This results is also coherent with what we observed on the film thickness in annular flow. The effect of gravity is visible at low mass flux, with a significant decrease of the film thickness in 0g compared to 1g. In Fig. 3.24, a flow pattern map is plotted with the domain of parameters (G,x) influenced by gravity. This map shows that future experiments will have to be focused on subcooled boiling regime and also mass fluxes smaller that $G = 100kg/m^2/s$.

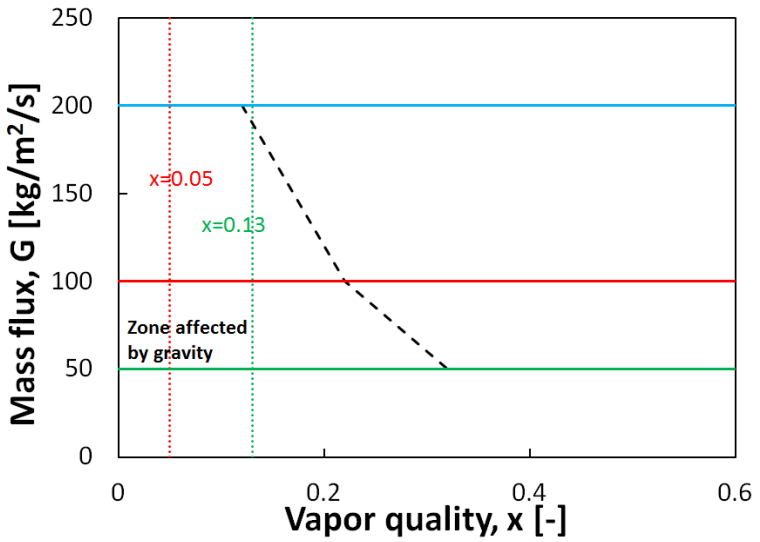

Figure 3.24: Flow patterns map of data for the sapphire tube with transition lines of gravity impact.

3.5 Liquid film structure in annular flows

3.5.1 Wall and interfacial shear stress measurements from Narcy et al.

The preceding results on the liquid film thickness in annular flow and the heat transfer coefficient pointed out that annular flows are influenced by gravity for the lowest mass flux $G = 50\ kg/m^2/s$. In the present study, the wall friction has not been measured, but we can refer to the previous study of Narcy et al. [62], where the wall friction in normal and microgravity were compared for 2 mass fluxes $G = 50\ kg/m^2/s$ and $G = 200\ kg/m^2/s$. The wall shear stress τ_w was deduced from pressure drop dP/dz and void fraction measurements

by using the momentum balance of the mixture in adiabatic flow:

$$-\frac{dP}{dz} - \frac{4\tau_w}{D} - (\rho_l (1-\alpha) + \rho_v \alpha) g = 0 \tag{3.8}$$

It was compared to the classical prediction of Lockhart and Martinelli [57], who proposed to express the frictional pressure gradient in two-phase flows versus the single-phase liquid flow frictional pressure gradient $(dP/dz)_L$, and a multiplier ϕ_l^2:

$$\frac{4\tau_w}{D} = \left(\frac{dp}{dz}\right)_l \phi_l^2 \quad \text{with} \quad \phi_l^2 = \left(1 + \frac{C}{X} + \frac{1}{X^2}\right) \quad \text{and} \quad X = \frac{\left(\frac{dp}{dz}\right)_l}{\left(\frac{dp}{dz}\right)_v} \tag{3.9}$$

$C = 20$ if the single-phase liquid and vapor flows are both turbulent (tt) and $C = 12$ if the single-phase liquid flow is laminar and single-phase vapor flows turbulent (lt). Narcy et al. [63] plotted, the experimental value Φ_L^2 versus Martinelli's parameter X for $G = 50\ kg/m^2/s$ and $G = 200\ kg/m^2/s$. For $G = 200\ kg/m^2/s$, the wall shear stress is the same in normal and microgravity conditions and close to Lockhart and Martinelli correlation for turbulent liquid and vapor flows. The wall shear stress is much higher in 1g than in 0g for G values smaller than $100\ kg/m^2/s$.

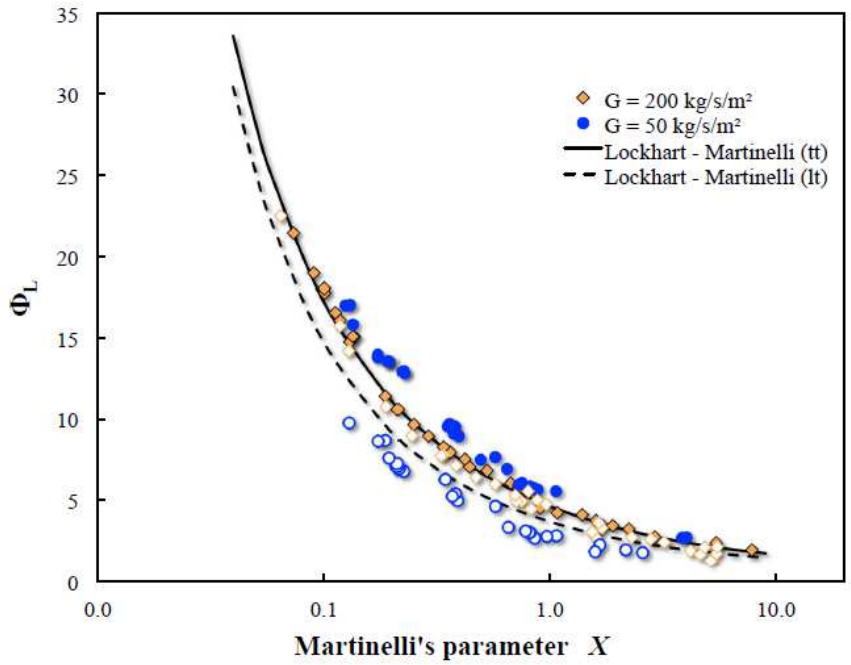

Figure 3.25: Experimental two-phase multiplier according to Martinelli's parameter from 1g (closed symbols) and 0g (open symbols) conditions comparisons with two correlations proposed by Lockhart and Martinelli [57].

Narcy et al. [63] also calculated the interfacial shear stress from the measurements of the void fraction and pressure drop by using the momentum balance equation for the vapor phase:

$$-\alpha\frac{dP}{dz} - \frac{4\tau_i\sqrt{\alpha}}{D} - \rho_v\alpha g = 0 \tag{3.10}$$

Narcy et al. [63] plotted the interfacial friction factor $f_i \approx 2\tau_i/\rho_v U_v^2$ scaled by the friction factor of the vapor core $f_v = 0.079(Re_v)^{-1/4}$ versus the Reynolds number of the vapor $Re_v = j_v D/V$ in Fig. 3.25.

In Fig. 3.26 , it can be seen that for $G = 200\ kg/m^2/s$, the interfacial friction in 1g and 0g are close as the wall friction and void fraction are. However at $G = 100\ kg/m^2/s$, the interfacial shear stress is much lower in microgravity than it is in normal gravity. The void fraction probes did not have the sufficient spatial and temporal resolutions, then it was not possible to perform an analysis of the liquid film structure from these measurements. Wang et al. [82] performed such an analysis using conductance probes to measure the film thickness in an air-water annular flow in a small inner diameter tube ($9.525mm$ i.d.).

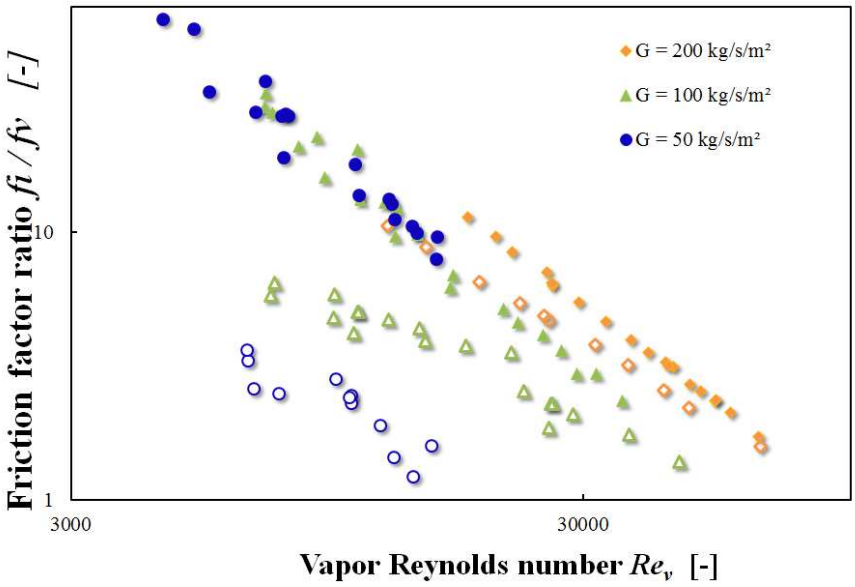

Figure 3.26: Dimensionless interfacial friction factor versus vapor Reynolds number in 1g (closed symbols) and in 0g (open symbols).

They found that gravity level alter the friction factor and film roughness. It was found that wave height, hence the relative interfacial roughness decreased with increasing the gas Reynolds number. The roughness in microgravity is less than half of that in normal gravity, while the friction factor was about 10% smaller in microgravity than that in normal gravity.

3.5.2 Visualization and image processing of liquid film structure

Authors have characterized the film structure in annular flows from image processing of high speed video images. This is the approach we have adopted. The behavior of waves at the surface of the liquid film has been studied for pre-annular and annular flows [36], [37], [83], [40], [39], [3], [29].

In Fig. 3.27, a visualization of an annular flow shows the presence of disturbance waves and small ripples or capillary waves. Disturbance waves, are large amplitude waves. They have been identified as the major source of droplet entrainment, [27], [44], [73]. Advanced models for the prediction of droplet entrainment are based on the characteristics of the disturbance waves such as wavelength and speed.

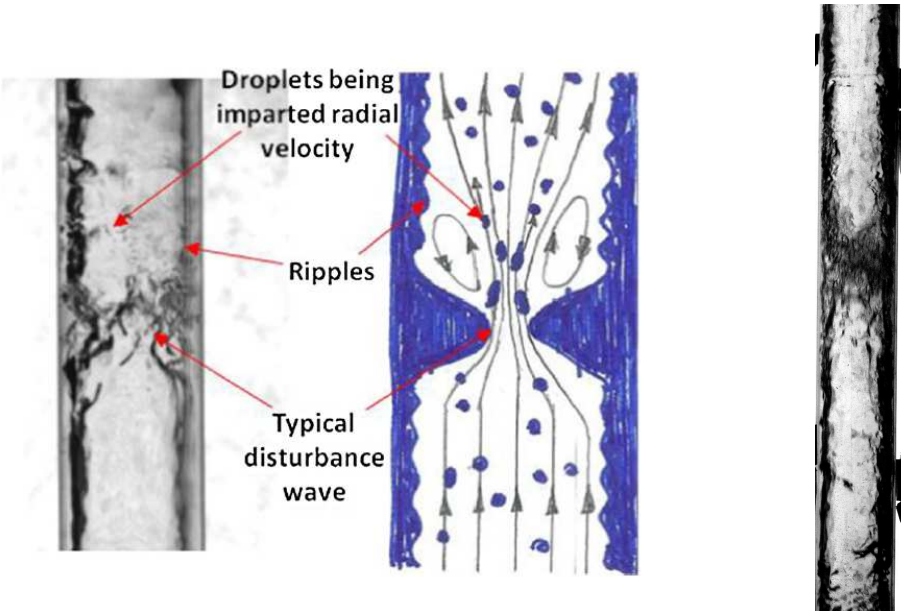

Figure 3.27: Typical disturbance waves and their schematic illustration according to Dasgupta et al. [29] to the left and to the right an annular flow seen with BRASIL.

In Fig.3.28 shows an annular flow for $G = 100kg/m^2/s$ and two qualities in 1g upward flow and in microgravity conditions. In these images, we can see both the presence of capillary waves with a small wave length and disturbance waves. As quality increases, the frequency of the disturbance waves increases.

From these images, a (x-t), space-time plot, was obtained for each run. The distance (tube length) and time are the axis of the plot. To obtain this plot, the centerline of the tube image, where the optical distortion is close to zero, is extracted. From the next image the same line is taken, extracted, and placed next to the first image and so on. This sequence of vertical lines give a plot of the height of the tube and the period registered by the camera. This image processing technique to determine the wave velocity was also performed by Hall-Taylor [39] and most recently Dasgupta et al. [29].

Figure 3.28: Observation of disturbance waves in microgravity and normal gravity for $G = 100\ kg/m^2/s$ at $x = 0.2$ for $q = 1\ W/s$ and $q = 2\ W/s$. The size difference of the 0g and 1g experiments is due to different type of cameras used on ground visualizations and in-flight visualization.

Analysis of these images was performed to obtain velocity of the disturbance waves and histograms of wave frequency. As we can see in Fig. 3.29a the disturbance waves are the long lines that we can see all along the tube. Ripples are also observed in the bottom part of the image and we can see that disturbance waves have a steeper slope which mean

they move faster than the ripples. In Fig. 3.29b we can observe wavy lines that we could identified as coalescence of waves, it is a characteristic of pre-annular regime, close to the transition to churn flow.

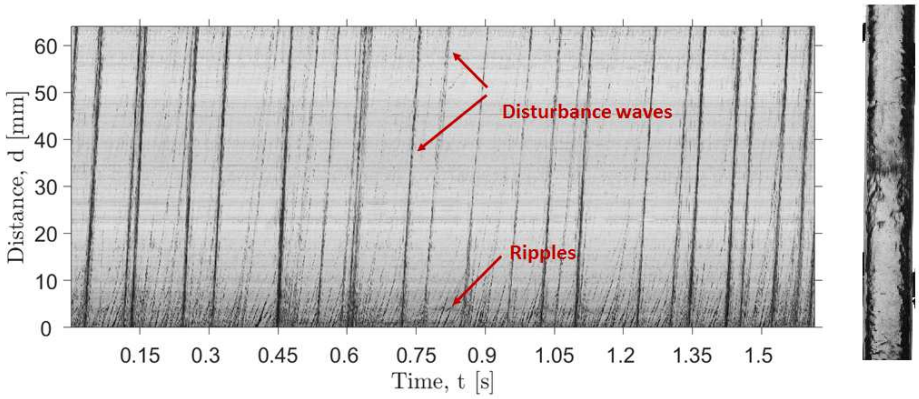

(a) Microgravity $G = 100\ kg/m^2/s$.

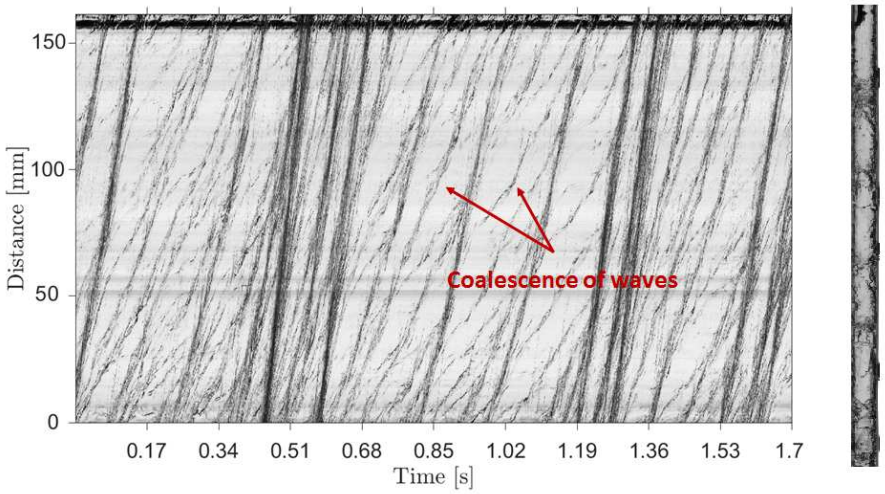

(b) Normal gravity $G = 100\ kg/m^2/s$.

Figure 3.29: Typical distance versus time plot for annular flows (top) and pre-annular flow (bottom).

Wave velocities

Mean waves velocities were calculated from the space-time plots. The slope was obtained from every wave passage and averaged into a mean value as shown in Fig. 3.30. For microgravity runs, the distance observed by the camera is smaller (64 mm) and we don't see

any variation between the beginning or the end of the image, on the other hand the velocity obtained from the ground measurements changes along the tube and it is noticeable. For this reason, the images were sectioned where the values of wall temperature measurements as references. Around this area velocities are obtained.

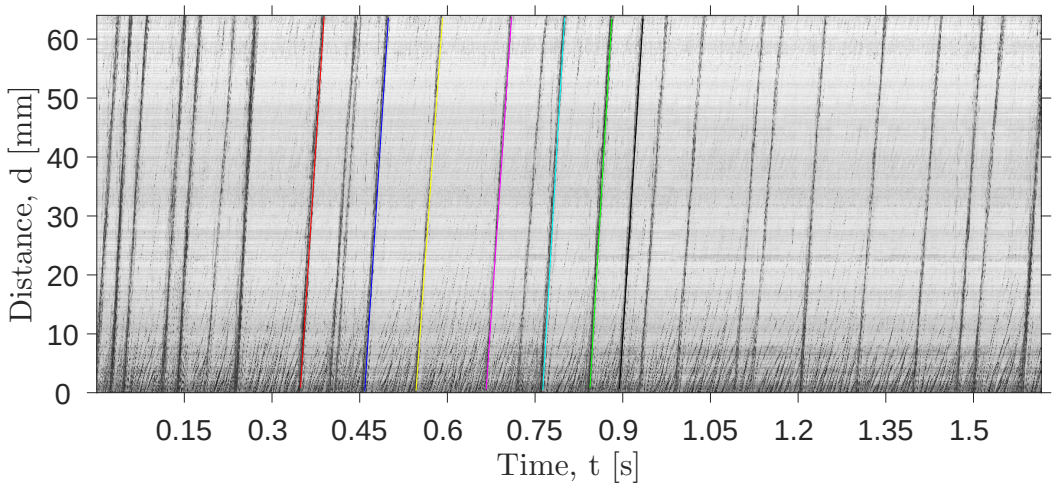

Figure 3.30: Mean disturbance wave velocity for an annular case at $G = 100kg/m^2/2$, $x = 0.2$ at 0g.

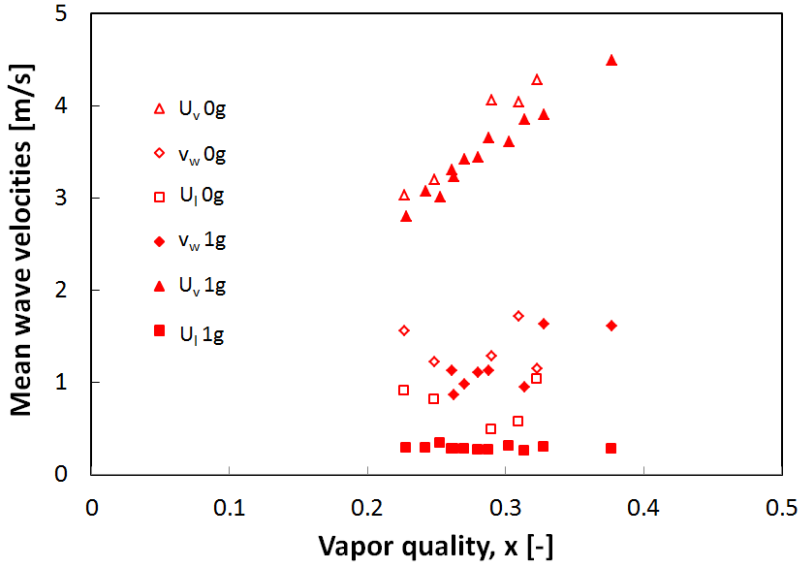

(a) Experiments at $G = 100\ kg/m^2/s$ in normal and microgravity

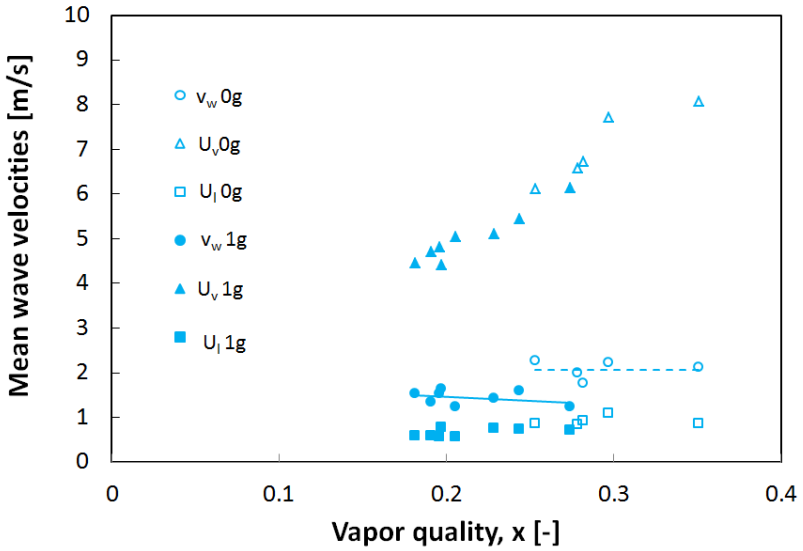

(b) Experiments at $G = 200\ kg/m^2/s$ in normal and microgravity

Figure 3.31: Waves average frequencies in normal and microgravity.

In Fig. 3.31 the mean velocity of the liquid U_l, gas U_v and waves v_w are plotted as a function of the vapor quality. We can observe how the velocity of the gas increases with the increase of x. We can also see that the wave velocity is higher in microgravity than in normal gravity, also the liquid velocity is slightly higher in microgravity that in normal gravity. Knowing that in normal gravity the liquid film thickness is thicker than in microgravity, this could explain that the liquid velocity is smaller especially for $G = 100\ kg/m^2/s$. The difference between the vapor velocity and the wave velocity is lower in microgravity conditions.

Table 3.3 assembles the mean liquid, gas and wave velocities measured and presented in Fig. 3.31. It highlights the difference between the normal gravity and the microgravity cases.

	1g				0g			
	x	U_L	U_g	v_w	x	U_L	U_g	v_w
G=100	0.28	0.26	3.65	0.74	0.24	0.81	3.19	1.13
	0.26	0.27	3.30	0.70	0.32	1.03	4.28	1.47
	0.24	0.28	3.07	0.68	0.22	0.90	3.02	1.19
	0.31	0.25	3.85	0.77	0.30	0.56	4.04	1.03
	0.28	0.26	3.43	0.72	0.29	0.48	4.06	0.97
G=200	0.21	0.56	5.04	1.21	0.25	0.84	6.11	1.57
	0.27	0.70	6.12	1.49	0.27	0.83	6.56	1.87
	0.24	0.73	5.44	1.30	0.29	1.07	7.71	2.01

Table 3.3: Mean liquid, gas and wave velocities at normal and microgravity conditions.

An histogram is presented in Fig. 3.34 with the number of waves per run and the velocities found on the space-time plots.

Correlations developed by Pearce [68] and Kumar et al. [52] allow to predict the wave velocities in annular flows. Pearce proposed to express the wave velocity v_w as:

$$v_w = \frac{K_{pr}\bar{u}_{lf} + U_g\sqrt{\frac{\rho_v}{\rho_l}}}{K_{pr} + \sqrt{\frac{\rho_v}{\rho_l}}} \tag{3.11}$$

where $\bar{u}_{lf}$ is the time averaged liquid film velocity, and K_{pr} is a parameter depending on pipe diameter. Taken equal to 0.51, the time averaged liquid film velocity is obtained from:

$$\bar{u}_{lf} = \frac{G\,(1-x)}{\rho_l\,(1-\alpha)} \tag{3.12}$$

The average film thickness, δ, for this experiment was evaluated experimentally by capacitance probes as explained in Chapter 2. The results of this comparison, shown in Fig. 3.32, appear to over predict the values obtained by our measurements of the velocity.

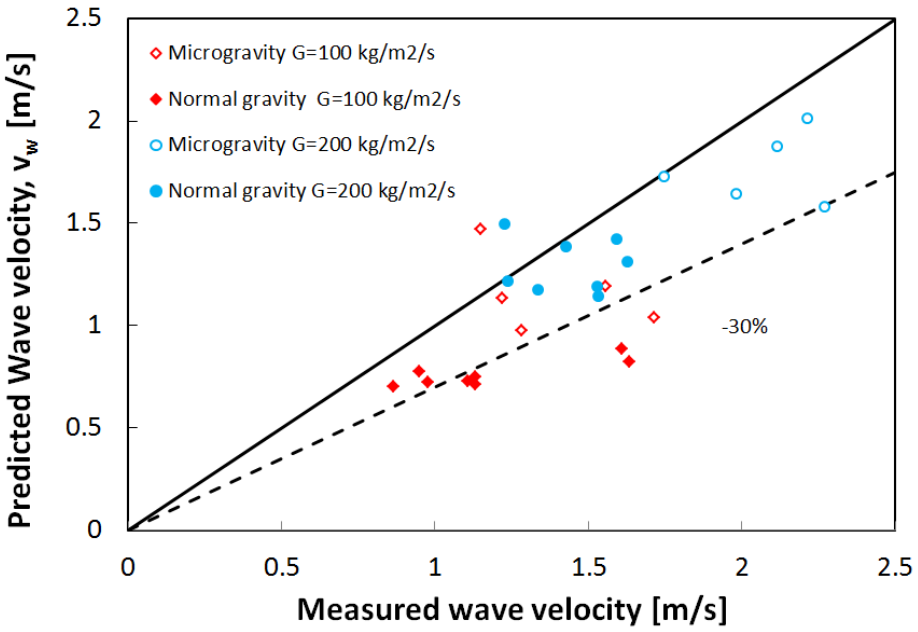

Figure 3.32: Comparison of the present measurements with Pearce's correlation.

The correlation proposed by Kumar et al [52], a much more recent one, derives from experiments on annular flows. This experiments were performed in a range of $\rho_g j_g^2 = 4700 - 8300\ kg/ms^2$ and $\rho_l j_l^2 = 7.5 - 600\ kg/ms^2$ which is outside the range of the experiments performed with BRASIL.

This correlation obtains the value of v_w as:

$$v_w = \frac{K_{Kum} j_v + j_l}{1 + K_{Kum}} \tag{3.13}$$

where K_{Kum} is a constant given by:

$$K_{Kum} = a \left(\frac{\rho_v}{\rho_l}\right)^{1/2} \left(\frac{Re_l}{Re_v}\right)^{1/4} \tag{3.14}$$

Since this correlation was proposed for rectangular channels and ours is circular, a has a value of 7.653 was used. In Fig. 3.33 we present the comparison with Kumar et al. correlation.

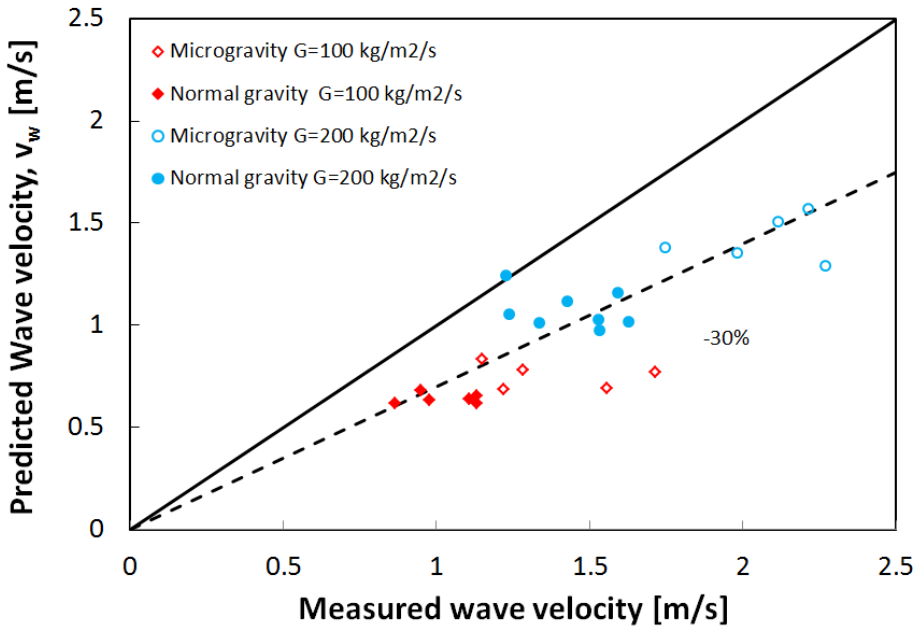

Figure 3.33: Comparison of the present measurements with Kumar's correlation.

For our experiment the correlation proposed by Kumar over predicts the values all along the data obtained. Pearce correlation seems to predict better for both values of G in this experiment.

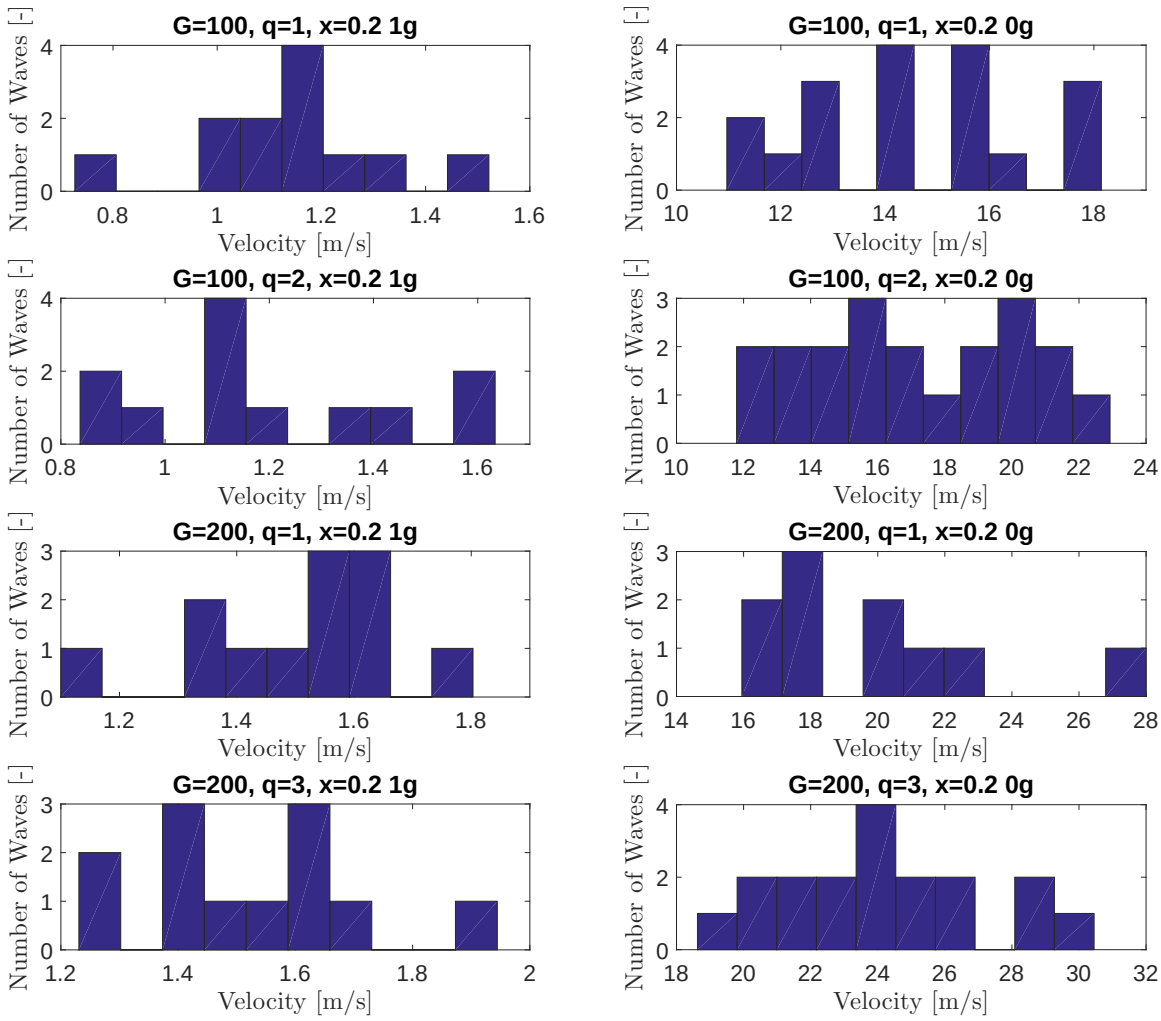

Figure 3.34: Histogram for wave velocities

Wave Frequency

The wave frequencies were obtained from the space-time plots. The period of the disturbance waves is characterized by the horizontal distance between two consecutive waves. The frequency is the inverse of the period.

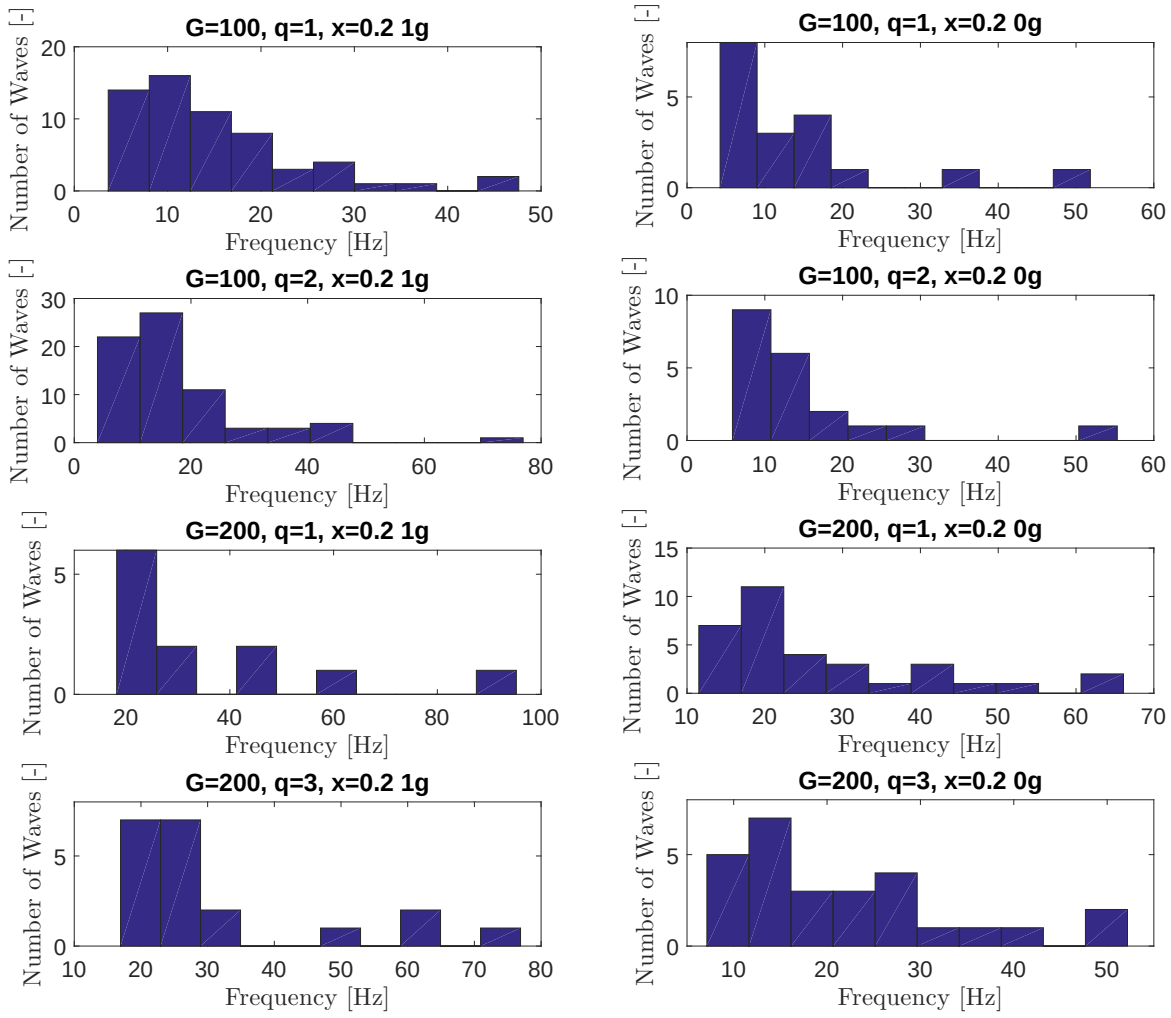

Figure 3.35: Histograms in microgravity and normal gravity.

The frequency of the waves are larger in normal gravity than in microgravity. A typical histogram of frequencies obtained from an annular cases is presented in Fig. 3.35. The histograms seem to be in the same range of values obtained by Dasgupta et al. [29], Fig. 3.36.

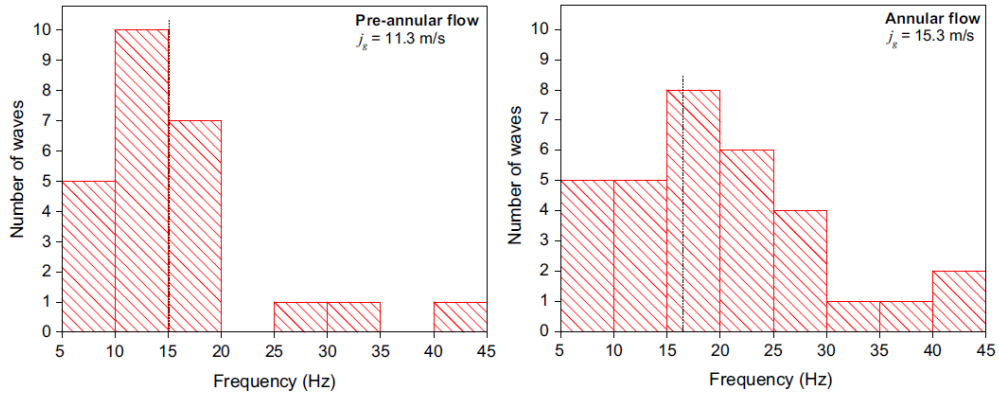

Figure 3.36: Histograms from Dasgupta et al. [29] for a Reynolds number $Re_l = 759$.

The average frequency was calculated and plotted as a function of j_v. In Fig. 3.37 we can see how the frequency seems to be higher for normal gravity that in microgravity. This could explain why we see an increase on the interfacial shear stress in normal gravity is obtained.

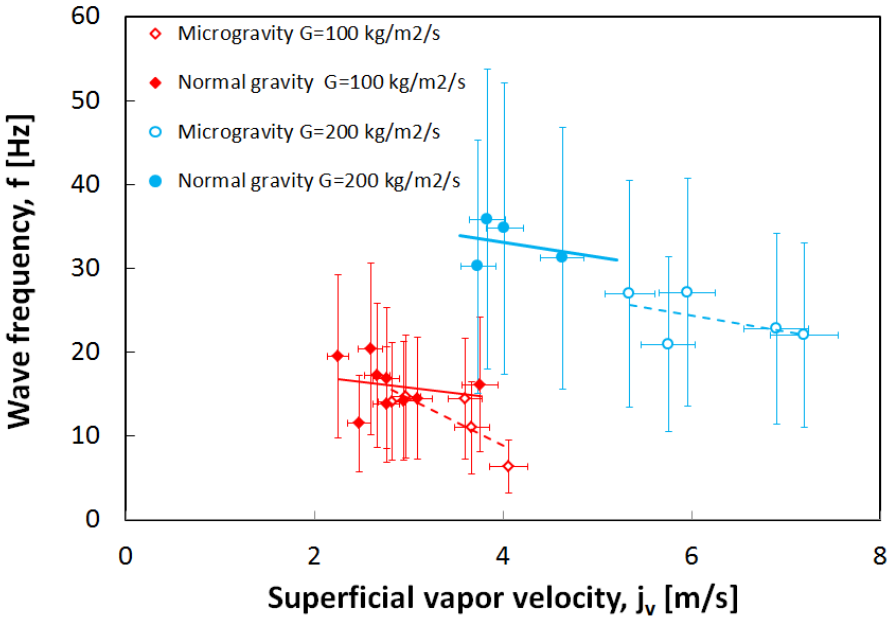

Figure 3.37: Waves average frequencies in normal and microgravity.

Further study should be made on the dependency of the frequency on j_v. Several authors

have observe a limiting j_v below which average frequency is independent [84] [28] [77].

The first results on the film structure by image processing in microgravity sim to show a decrease of the wave frequency and on the velocity difference $(U_w - v_w)$ in microgravity by comparison to normal gravity. This could explain the reduction of the interfacial shear stress and consequently the heat transfer coefficient in annular flow in microgravity for low mass fluxes. Unfortunately we were not able to analyze the results at the lowest mass flux $G = 50\ kg/m^2/s$, because dry-out frequently occurs in microgravity conditions.

3.6 Conclusion

Experimental results obtained in normal and microgravity have been analyzed and compared to experimental correlations and models of the literature. Access to flow patterns, regime transitions, void fraction, heat transfer coefficients, and wall and interfacial shear stresses can allow a future modeling of flow boiling.

Flow patterns showed that the transitions between regimes occurs at a constant value of void fraction and that Zuber model based on the drift flux model seems to predict the void fraction of this experiment with a good agreement.

Heat transfer coefficients have been measured with two different techniques and coherent data have been found. Although accuracy should be improved, subcooled runs for ground measurements and during parabolic flight campaign runs appear to be in line with each other.

The analysis of waves and film structure of annular flows seem to explain the increase in interfacial shear stress in normal gravity conditions for these regimes. Gravity's impact is identified and observed on void fraction, heat transfer coefficients, and film structures of annular flows at low mass fluxes. A cartography of the parameters (G,x) showing the impact of gravity is proposed.

Chapter 4

Conclusions and Perspectives

This chapter presents a summary of the results obtained during this PhD Thesis on flow boiling in vertical tubes in normal and microgravity conditions. The objectives were to obtain measurements on the hydrodynamics and heat transfer in flow boiling. Results on flow pattern, regime transitions, void fraction, heat transfer coefficient were obtained.

In chapter 1, the basic equations for two-phase flows with phase change were presented, as well as classical closure laws for the prediction of the void fraction, wall friction and heat transfer coefficient. Some recent results obtained in microgravity conditions are also described.

The experimental set-up described in this text, BRASIL, was built at the Institut de Mécanique des Fluides de Toulouse, specifically to study flow boiling of an upward flow with a 6 mm diameter tube. This experiment was conceived to carry out parabolic flights experiments in aircraft in order to understand the impact of gravity on flow patterns, regime transitions, void fraction, heat transfer coefficient and shear stresses. Protocols are developed to obtain data of the liquid temperature, vapor quality and visualization of the flows. The experimental set-up was upgraded in some instrumentation to improve accuracy and avoid noise in the measurements.

With the purpose of collaborating with the University of Maryland, BRASIL was adapted to include a different test section built by Prof. Jungho Kim and his team. An infrared camera provided by the European Space Agency was used to obtained the thermography measurements. Post processing the infrared images was coupled with the computation of the unsteady conduction in the silicon tube. Validation of both techniques implemented during this PhD work for the measurement of the heat transfer coefficient was essential to compare both methods and results.

Experimental results obtained in normal and microgravity were analyzed and compared to experimental correlations and models. Flow patterns were identified and characterized, regime transitions and quantitative results of the impact of microgravity on these regimes was presented. Void fraction improvements were achieved and a better precision was obtained. Correlations based on the drift-flux model were found to have a better agreement with this data. Heat transfer coefficient for both techniques seem to agree with each other.

The values observed are consistent for both methods. By all means, accuracy should be improved, especially for saturated data, but subcooled runs for ground measurements and during parabolic flight campaign runs appear to be in line with each other and with very little dispersion.

The analysis of waves and film structure of annular flows seem to explain the increase in interfacial shear stress in normal gravity conditions for these regimes. Gravity's impact is identified and observed on void fraction, heat transfer coefficients, and film structures of annular flows at low mass fluxes. A cartography of the parameters (G,x) showing the impact of gravity is proposed.

Further data processing and new experiments that complete the data base need to be performed to improve the modeling of flow boiling and especially the prediction of void fraction, wall and interfacial shear stresses and heat transfer coefficient. This work shows that measurements of the heat transfer coefficients are delicate and a special care has to be taken for calibration. Despite these precautions uncertainties often reach 20% and it is not obvious to evaluate the impact of gravity. There is a need of additional data at low mass flux where gravity has a dominant impact. In these conditions, parabolic flights experiments become critical because of the effect of the g-jitter, which cannot be anymore neglected. This is the reason why future experiments on the International Space Station are foreseen.

Bibliography

[1] N. Achour. 2017. Étude du transfert de chaleur en ébullition convective en gravité terrestre et en micro-gravité. Projet de fin d'études. Département Génie Industriel.

[2] M. Al-Arabi. 1982. Turbulent heat transfer in the entrance region of a tube. J. of Heat Transfer Engineering, 3, 76-83.

[3] B.J. Azzopardi. 1986. Disturbance wave frequencies, velocities and spacing in vertical annular two-phase flow. Nucl. Eng. Des. 92 121-133.

[4] T. Gomyo, H. Asano. 2016. Void Fraction characteristics of one-coponent gas-liquid two-phase flow in small diameter tubes. I. Ph. and Heat Transfer. Vol. 4(1). pp. 1-8.

[5] M.M. Awad, Y.S. Muzychka. 2008. Effective property models for homogeneous two-phase flows. Experimental Thermal and Fluid Science, 33(1), pp. 106-113.

[6] M.M. Awad, Y.S. Muzychka. 2010. Review and modeling of two-phase frictional pressure gradient at microgravity conditions. Fluid Enginnering Division Summer Meeting ASME, Montreal.

[7] M.M. Awad, Y.S. Muzychka. 2010. Bounds on two-phase frictional pressure gradient and void fraction in circular pipes. Advances in Mechanical Engineering.

[8] C. Baltis, G.P. Celata, M. Cumo, L. Saraceno, G. Zummo. 2012. Gravity influence on heat tranfer rate in flow boiling. Microgravity Sci. Technol. Vol. 24. pp. 203-213.

[9] S.M. Bhagwat and A.J. Ghajar. 2014. A flow pattern independent drift flux model based void fraction correlation for a wide range of gas-liquid two phase flow.

[10] W.S. Bousman, A.E. Dukler. 1993. Study of gas-liquid flow in microgravity: void fraction, pressure drop and flow pattern. Proceedings of the 1993 ASME Winter

Meeting, New Orleans, LA. 174-175.

[11] W.S. Bousman. 1994. Studies of two-phase gas-liquid flow in microgravity. PhD Diss. Univ. of Houston.

[12] G.P. Celata and G. Zummo, 2009. Flow Boiling heat transfer in microgravity: Recent progress.

[13] R. Chanay. 2014. Experimental study of flow boiling in horizontal minichannels at high saturation temperature. Institut Natational des Science Appliquées de Lyon.

[14] I.Y. Chen, R.S. Downing, E. Keshock, M. Al-Sharif. 1991. Measurements and correlation of two-phase pressure drop under microgravity conditions. Journal of Thermophysics. Vol. 5. pp. 514-523.

[15] I.Y. Chen. 1966. Correlation for boiling heat transfer to saturated fluids in convective flow. Industrial Engineering Chemistry Process Design and Development. Vol. 5(3). pp. 322-339.

[16] I.Y. Chen, R.S. Downing, R. Parish, E. Keshock. 1988. A reduced gravity flight experiment: observed flow regimes and pressure drops of vapor and liquid flow in adiabatic piping.

[17] L. Chen, Y.S. Tian, T.G. Karayiannis. 2006. The effect of tube diameter on vertical two-phase flow regimes in small tubes. Int. J. of Heat and Mass Transfer.

[18] Chrisholm. 1973. Pressure gradientsdue to friction during the flow of evaporating two-phase mixtures in smooth tubes and channels. Internat. J. of Heat and Mass Transfer. 16(2), pp. 347-358.

[19] A. Cioncolini, J.R. Thome. 2011. Algebraic turbulence modeling in adiabatic and evaporation annular two-phase flow, Int. J. of Heat and Fluid Flow, 32, 805-817.

[20] A. Cioncolini, J.R. Thome, 2012. Entrained liquid fraction prediction in adiabatic and evaporation annular two-phase flow. Nuclear Engineering and design, 32, 200-213.

[21] A. Cioncolini, J.R. Thome. 2012.Void fraction prediction in annular two-phase flow. Int. J. of Multiphase Flow. 43, pp. 72 – 84.

[22] C. Colin. 1990. Écoulements diphasiques a bulles et a poches en micropesanteur. Thesis, Institut de Mécanique de Fluides de Toulouse, France.

[23] C. Colin, J. Fabre, A. Dukler. 1991. Gas-liquid glow at microgravity conditions-i Dispersed bubble and slug flow. Int. J. of Multiphase Flow. 17, pp. 533-544.

[24] C. Colin, J. Fabre, J. McQuillen. 1996. Bubble and slug flow at microgravity conditions: state of knowledge and open questions. Chemical Engineering Communications. 141-142, pp. 155-173.

[25] J.G. Collier. 1980. Convective boiling and condensation. McGraw-Hill book company. Second Edition, pages 50-133.

[26] M. Cooper. 1984. Heat flow rates in saturated nucleate pool boiling a wide-ranging examination using reduced properties. Advances in Heat Transfer. 16, pp. 157-239.

[27] L.B. Cousins, G.F. Hewitt. 1968. Liquid Mass Transfer in Annular Two-Phase Flow: Droplet Deposition and Liquid Entrainment. AERE-R5657, Harwell, UK, 1968.

[28] K.J. Chu. 1973. Statistical characterization and modeling of wavy liquid films in vertical two-phase flow. Ph.D. Thesis. University of Houston.

[29] A. Dasgupta, D.K. Chandraker, S. Kshirasagar, B. Raghavendra Reddy, R. Rajalakshmi, A.K. Nayak, S.P. Walker, P.K. Vijayan, G.F. Hewitt. 2016. Experimental investigation on dominant waves in upward air-water two-phase flow in churn and annular regime. Experimental Thermal and Fluid Science. Vol 81. pp. 147-163.

[30] A.E. Dukler, M. Wicks, R.G. Cleveland 1964. Pressure drop and hold-up in two-phase flow Part A- a comparison of existing correlations and Part B- an approach through similarity analysis. A.I.Ch.E. Journal. 10 (1). pp.38-43.

[31] A.E. Dukler. 1988 Gas-Liquid flow at microgravity conditions: flow patterns and their transitions. Int. J. of Multiphase Flow. Vol. 14. pp. 389-400.

[32] K. Elkow, K Rezkallah. 1997. Void Fraction measurements in gas-liquid flows under 1-g and 0-g conditions using capacitance sensors. Int. J. Multiphase Flow. Vol. 23. pp. 815-829.

[33] H.K. Forster and N. Zuber. 1955 Dynamics of vapor bubbles and boiling heat transfer. A.I.Ch.E. Journal 1, 531-535.

[34] F. García, R. García, J.C. Padrino, C. Mata, J.L. Trallero, D.D. Joseph. 2003. Power law and composite power law friction factor correlations for laminar and turbulent gas-liquid flow in horizontal pipelines. Int. J. of Multiphase Flow, Vol. 29, No. 10, pp. 1605-1624.

[35] V. Gnielinski. 1976. New equations for heat and mass transfer in turbulent pipe and channel flow. International Journal of Heat and Mass Transfer. vol 16. pp. 359-368.

[36] A.H. Govan, G.F. Hewitt, S.B. Lim. 1990. Visualization studies of churn flow in a vertical pipe, in: Second Irish Research Colloquia, 9th March. Institution of Chemical Engineers, Belfast.

[37] J.R. Barbosa, A.H. Govan, G.F. Hewitt. 2001 Visualisation and modelling studies of churn flow in a vertical pipe. Int. J. Multiph. Flow 27. 2105-2127.

[38] A. Greco. 2008. Convective boiling of pure and mixed refrigerants: an experimental study of the major parameters affecting heat transfer. Int. J. Heat Mass Transfer 51. 896-909.

[39] N. Hall-Taylor, G.F. Hewitt, P.M.C. Lacey. 1963. The motion and frequency of large disturbance waves in annular two-phase flow of air-water mixtures. Chem. Eng. Sci. 18. pp. 537-552.

[40] H. Han, Z. Zhu, K. Gabriel. 2006. A study on the effect of gas flow rate on the wave characteristics in two-phase gas-liquid annular flow. Nucl. Eng. Des. Vol. 236. pp. 2580-2588.

[41] W.S. Hill, F.R. Best. 1991. Microgravity two-phase flow experiment and test results. SAE Tech. Paper Ser. 911556, Int. Conf. on Env. System, San Francisco.

[42] S. Huckerby, K. Rezkallah. 1992. Flow pattern observation in two-phase gas liquid flow in a staight tybe under normal and microgravity conditions. Prodessings of the National Heat Transfer Conference, 2.

[43] M. Ishii. 1977. One-dimensional drift-flux model and constitutive equations for relative motion between phases in various two-phase flow regimes. ANL-77-47.

[44] M. Ishii, M.A. Grolmes. 1975. Inception criteria for droplet entrainment in two-phaseconcurrent film flow. AIChE J. 21. pp 308-318.

[45] A.J.P. Janicot. 1988. Experimental and theoretical studies of gas-liquid two-phase flow at reduced gravity conditions. MS Thesis, Univ. of Houston.

[46] S. Jayawardena, V. Balakotaiah, and L. Witte. 1997. Flow pattern transition map for microgravity two phase flows. A.I.Ch.E. Journal, Vol. 43, pp. 1637-1640.

[47] S.G. Kandlikar. 1990. A general correlation for saturated two-phase flow boiling heat transfer inside horizontal and vertical tubes. Int. J. of Heat Transfer, Vol. 112. pp. 219-228.

[48] I. Kataoka and M. Ishii. 1987. Drift flux model for large diameter pipe and new correlation for pool void fraction. Int. J. of Heat and Mass Transfer. Vol. 30, No. 9. pp. 1927-1939.

[49] T.H. Kim, E. Kommer, S. Dessiaroun,J. Kim. 2012. Measurements of two-phase flow and heat transfer parameters using infrared thermometry. Int. J. Multiphase Flow, 40, 56-67.

[50] S.-M. Kim, I. Mudawar. 2013. Universal approach to predicting saturated flow boiling heat transfer in mini/micro-channels - Part II: two-phase heat transfer coefficient. Int. J. of Heat and Mass Transfer 64, pp. 1239-1256.

[51] S.-M. Kim, I. Mudawar. 2013. Universal approach to predicting saturated flow boiling heat transfer in mini/micro-channels - Part I. Dryout incipience quality. Int. J. of Heat and Mass Transfer. 64, pp. 1226-1238.

[52] R. Kumar, M. Gottmann, K.R. Sridhar. 2002. Film thickness and wave velocity measurements in a vertical duct. J. Fluids Eng. Vol. 124. pp. 634-642.

[53] S. Kutateladze. 1961. Boiling heat transfer. Int. J. of Heat and Mass Transfer. 4, pp. 31-45.

[54] M.T. Lebon, C.F. Hammer, J. Kim. 2018. Gravity effectson subcooled flow boiling heat transfer. Int. J. of Heat and Mass Transfer. 128, pp. 700-714.

[55] S. Lin, P. Kew, K. Cornwell. 2001. Two-phase heat transfer to a refrigerant in a 1 mm diameter tube. Int. J. of Refrigeration. 24 (1). pp. 51-56.

[56] Z. Liu, R.H.S. Winterton. 1991. A general correlation for saturateed and subcooled flow boiling in tubes and annuli, based on a nucleate pool boiling equation. Int. J. Heat Mass Transfer, Vol. 34, No. 11, pp. 2759-2766.

[57] R.W. Lockhart, R.C. Martinelli. 1949. Proposed correlation of data for isothermal two-Phase, two-component flow in pipes. Chemical Engineering Progress Symposium Series. 45 (1). pp. 39-48.

[58] R. Mastrullo, A.W. Mauro, A. Rosato, G.P. Vanoli. 2009. Carbon dioxide local heat transfer coefficients during flow boiling in a horizontal circular smooth tube. Int. J. Heat Mass Transfer 52. 4184-4194.

[59] W. McAdams, W. Woods, R. Bryan. 1942. Vaporization inside horizontal tubes-ii-benzene-oil mixtures. J. of Heat Transfer. 64. pp. 193-200.

[60] K. Mishima, M. Ishii. 1984. Flow regime transition criteria for upward two phase flow in vertical tubes. Int. J. Heat Mass Transfer. Vol. 27. No. 5. pp. 723-737

[61] M. Narcy, E. de Malmazet, C. Colin. 2014. Flow boiling in tube under normal gravity and microgravity conditions. Int. J. Multiphase Flow 60, 50-63.

[62] M. Narcy, A, Scammell, C. Colin, J. Kim. 2015. Flow boiling under microgravity conditions. Proceedings of the 15th International Heat Transfer conference, IHTC-15, August 10-15, 2014.

[63] M. Narcy, C. Colin. 2015. Two-phase pipe flow in microgravity with and without phase change:recent progress and future prospects. I. Ph. and Heat Transfer. 60. pp. 50-63.

[64] M. Narcy. 2014. Flow boiling in tube under normal gravity and microgravity conditions. Thesis.

[65] H.K. Oh, C.H. Son. 2011 Evaporation flow pattern and heat transfer of R-22 and R-134a in small diameter tubes. Heat Mass Transfer 47. 703-717.

[66] H. Ohta. 2003. Microgravity heat transfer in flow boiling. Advances in heat transfer. Advances in Heat Transfer. Vol. 37. pp. 1-76.

[67] H. Ohta, Baba. 2003. Microgravity heat transfer in flow boiling. Advances in heat transfer. Advances in Heat Transfer. Vol. 37. pp. 1-76.

[68] D.L. Pearce. 1979. Film waves in horizontal annular flow: space time correlatior experiments. RD/L/N/111/79. Central Electricity Research Laboratories.

[69] M.H. Rausch, L. Kretschmer, S. Will, A. Leipertz, and A. P. Froba. 2015. Density, surface tension, and kinematic viscosity of hydrofluorethers HFE-7000, HFE-7100, HFE-7200, HFE-7300, and HFE-7500. J. of Chemical & Engineering Data. Vol. 60. No. 12. pp. 3759-3765.

[70] T.R. Reinarts. 1993. Adiabatic two phase flow regime data and modeling for zero and reduced (horizontal flow) acceleration fields. PhD Diss. Texas A& M Univ., College Station.

[71] K.S. Rezkallah, L. Zhao. 1995. Pressure drop in gas-liquid flow at microgravity conditions. Int. J. of Multiphase Flow. Vol. 21. pp. 837-849.

[72] K.S. Rezkallah. 1996. Weber number based flow-pattern maps for liquid-gas flows at microgravity. Int. J. of Multiphase Flow. Vol. 22. pp. 1265-1270.

[73] P. Sawant, M. Ishii, M. Mori 2009. Prediction of amount of entrained droplets in vertical annular two-phase flow. Int. J. Heat Fluid Flow. Vol. 30. pp. 715-728.

[74] A. Scammell. 2016. A Study of Heat Transfer and Flow Characteristics of Rising Taylor Bubbles. PhD Dissertation, University of Maryland.

[75] J. Thome. 2006. State-of-the-Art Overview of boiling and Two-Phase Flows in Microchannels. Heat Transfer Engineering. Vol. 27. No. 9. pp. 4-19.

[76] J. Thome. Encyclopedia of Two-Phase Heat Transfer and Flow IV, Modeling Methodologies, Boiling of CO_2, and Micro-Two-Phase Cooling, Volume 4: Special Two-Phase Flow and Boiling Topics, Chapter 3. C. Colin, M. Narcy. 2018. World Scientific. pp. 93–137.

[77] G.R. Thwaites, N.N. Kulov, R.M. Nedderman. 1976. Liquid film properties in two-phase annular flow. Chem. Eng. Sci. Vol. 31. pp. 481-486.

[78] Y. Taitel, A.E. Dukler. 1976. A Model for predicting flow regime transitions in horizontal and near horizontal gas-liquid flow. A.I.Ch.E. Journal. Vol. 22, No.1. pp. 47-55.

[79] Y. Taitel, D. Barnea, A.E. Dukler. 1980. Modeling flow pattern transitions for steady upward gas-liquid flow in vertical tubes. A.I.Ch.E. Journal. Vol. 26. No. 3. pp. 345-354.

[80] G.B. Wallis. 1969. One Dimensional Two-Phase Flow, McGraw-Hill, New-York.

[81] C.C. Wang, C.S. Chiang, J.G. Yu. 1988. An experimental study of in tube evaporation of R-22 inside a 6.5 mm smoth tube. Int. J. Heat fluid Flow. Vol. 19. pp.259-269.

[82] Z. Wang, K.S. Gabriel, D.L. Manz. 2004. The influences of wave height on the interfacial friction in annular gas–liquid flow under normal and microgravity conditions, Int. J. of Multiphase Flow, Vol. 30. pp. 1193-1211.

[83] K. Wang, B. Bai, W. Ma. 2013. Huge wave and drop entrainment mechanism in gasliquid churn flow. Chem. Eng. Sci. Vol. 104. pp. 638-646

[84] D. Webb. 1970. Studies of Characteristics of Downward Annular Two-phase Flow, Ph. D. Thesis, University of Cambridge.

[85] R. Yun, Y. Kim, M.S. Kim. 2005. Convective boiling heat transfer characteristics of CO2 in microchannels, Int. J. Heat Mass Transfer. Vol. 48. pp. 235-242.

[86] L. Zhao, K.S. Rezkallah. 1993. Gas liquid flow patterns at microgravity conditions, Int. J. Multiphase Flow. Vol. 19. pp. 751-763.

[87] J. Zhao, J. Xie, H. Lin, W. Hu, A. Ivanov, and A. Belyaev.2001. Experimental studies on two-phase flow patterns aboard the mir space station. Int. J. of Multiphase Flow. Vol. 27. pp. 1931–1944.

[88] X. Zhao, P.K. Bansal. 2007. Flow boiling heat transfer characteristics of CO2 at low temperatures. Int. J. Refrig. Vol. 30. pp. 937-945.

[89] N. Zuber and J.A. Findlay. 1965. Average volumetric concentration in two phase flow systems. J. of Heat Transfer. pp. 453-468.

[90] N. Zuber, F.W. Staub, G. Bijwaard, P.G. Kroeger. 1967. Steady state and transient void fraction in two-phase flow systems: Final report for the program of two-phase flow investigation. GEAP-5417.